Alma Mater Studiorum – Università di Bologna

DOTTORATO DI RICERCA IN

Scienze Ambientali: tutela e gestione delle risorse naturali

Ciclo XXII
Settore scientifico-disciplinare di afferenza: GEO/12

TITOLO TESI:

''Bio-physical interactions and feedbacks in a global climate model''

Presentata da:

Lavinia Patara

Coordinatore Dottorato:	**Relatore:**	**Correlatori:**
	Prof. Nadia Pinardi	**Dr. Simona Masina**
Prof. Elena Fabbri		**Dr. Marcello Vichi**

Esame finale anno 2010

Abstract

This PhD thesis addresses the topic of large-scale interactions between climate and marine biogeochemistry. To this end, centennial simulations are performed under present and projected future climate conditions with a coupled ocean-atmosphere model containing a complex marine biogeochemistry model. The role of marine biogeochemistry in the climate system is first investigated. Phytoplankton solar radiation absorption in the upper ocean enhances sea surface temperatures and upper ocean stratification. The associated increase in ocean latent heat losses raises atmospheric temperatures and water vapor. Atmospheric circulation is modified at tropical and extratropical latitudes with impacts on precipitation, incoming solar radiation, and ocean circulation which cause upper-ocean heat content to decrease at tropical latitudes and to increase at middle latitudes. Marine biogeochemistry is tightly related to physical climate variability, which may vary in response to internal natural dynamics or to external forcing such as anthropogenic carbon emissions. Wind changes associated with the North Atlantic Oscillation (NAO), the dominant mode of climate variability in the North Atlantic, affect ocean properties by means of momentum, heat, and freshwater fluxes. Changes in upper ocean temperature and mixing impact the spatial structure and seasonality of North Atlantic phytoplankton through light and nutrient limitations. These changes affect the capability of the North Atlantic Ocean of absorbing atmospheric CO_2 and of fixing it inside sinking particulate organic matter. Low-frequency NAO phases determine a delayed response of ocean circulation, temperature and salinity, which in turn affects stratification and marine biogeochemistry. In 20th and 21st century simulations natural wind fluctuations in the North Pacific, related to the two dominant modes of atmospheric variability, affect the spatial structure and the magnitude of the phytoplankton spring bloom through changes in upper-ocean temperature and mixing. The impacts of human-induced emissions in the 21st century are generally larger than natural climate fluctuations, with the phytoplankton spring bloom starting one month earlier than in the 20th century and with ~50% lower magnitude. This PhD thesis advances the knowledge of bio-physical interactions within the global climate, highlighting the intrinsic coupling between physical climate and biosphere, and providing a framework on which future studies of Earth System change can be built on.

Table of Contents

5. Marine biogeochemical variability in the North Pacific in XX and XXI century simulations   90

Chapter 1

Introduction

The Earth's climate comprises a variety of physical and biospheric processes ultimately powered by the Sun energy (Peixoto and Oort, 1992). A vast range of physical, chemical, biological, and human processes interact simultaneously and at different spatio-temporal scales within and among the atmospheric, oceanic, and land components of the climate system. Earth system science is devoted to investigating the nature of these interactions and assessing their role on the mean state and temporal evolution of the Earth's climate.

Fig. 1-1 shows a schematic representation of Earth system components and interactions of relevance for this study. The Earth's climate exhibits strong fluctuations in time both due to natural variability and to external forcings. Natural climate fluctuations (arrow 1) span multiple time scales - interannual, interdecadal, multidecadal - and arise from the atmosphere's dynamics and from ocean-atmosphere interaction. Well known climate fluctuations are the El Niño-Southern Oscillation involving pressure and ocean temperature redistributions between the eastern and western tropical Pacific (Philander, 1990), the Northern and Southern Annular Modes involving seesaws of atmospheric mass between polar and middle latitudes (Thomson and Wallace, 2000), and the Pacific North American teleconnection associated - among others - with fluctuations of the Aleutian Low strength (Wallace and Gutzler, 1981). Atmospheric oscillations affect ocean properties through heat, momentum, and freshwater exchanges (Visbeck et al., 2003), and are hypothesized to be in turn influenced to some degree by oceanic temperature patterns (Czaja and Frankignoul, 2001).

External forcing of climate variability (arrow 2) arises from any process capable of modifying the radiative balance of the Earth System. This occurs for instance through changes in solar activity, changes in the Earth's orbital parameters (Hays, 1976), or through fossil fuel emissions by human activities (Forster et al., 2007). This latter process increases the atmospheric greenhouse gas concentrations and thus the fraction of longwave radiation re-emitted towards the Earth surface. A larger greenhouse gas concentration is thus expected to increase atmospheric temperatures which in turn

impact the ocean compartment, e.g. through changes in steric height and stratification (Bindoff et al., 2007; Meehl et al., 2007).
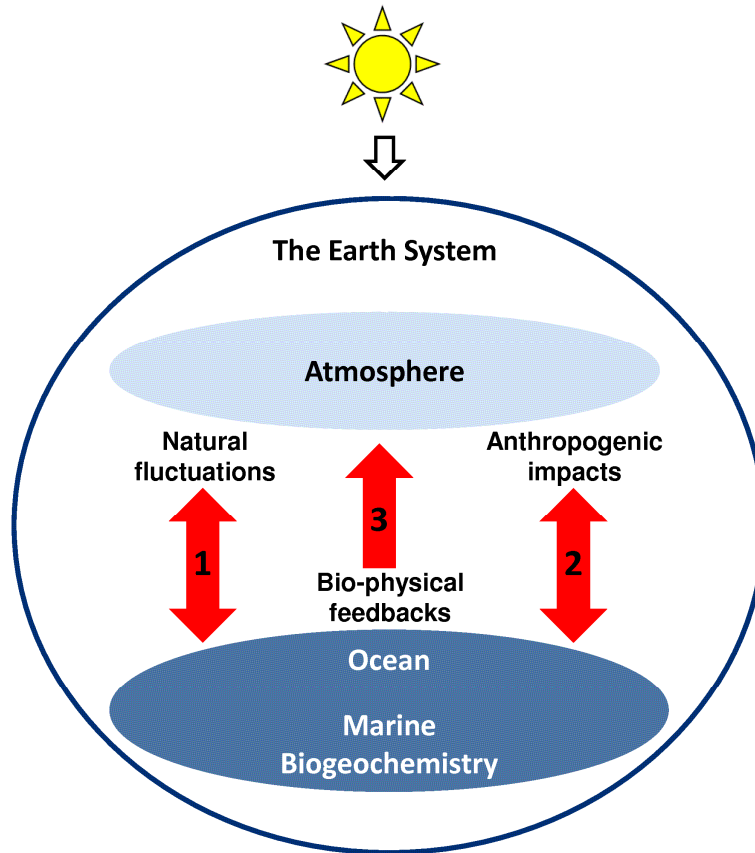
Fig. 1-1: Schematic representation of Earth system components and interactions of relevance for this study.

This PhD thesis focuses on the study of large-scale interactions between physical climate and marine biogeochemistry. Marine biogeochemistry is closely related to the physical processes occurring within the Earth System. Ocean-atmosphere dynamics and external forcing affect marine biogeochemistry through a variety of processes such as ocean mixing and circulation, sea ice coverage, and incoming solar radiation. More precisely, these processes modify environmental conditions relevant to the lower trophic levels of the marine ecosystems through changes in ocean temperature, nutrients, and solar radiation availability (Mann and Lazier, 1996; Longhurst, 2007). Natural climate fluctuations (arrow 1) and anthropogenic climate change (arrow 2) may therefore significantly impact the composition, spatial structure, and temporal evolution of the ocean biogeochemical compartment (Sarmiento and Gruber, 2006).

The interaction between physical climate and marine biogeochemistry is however bi-directional. Marine biogeochemical processes may in fact create feedbacks onto the

physical climate system (arrow 3), owing to their capability of modifying physical and chemical properties of their surrounding environment (Denman et al., 1996). For instance, phytoplankton absorbs CO_2 and contributes to the sequestration of atmospheric CO_2 (biological pump) and produces other radiatively-active chemical substances (Boyd and Doney, 2003). Another bio-physical feedback is the absorption of solar radiation by phytoplanktonic organisms which modifies the upper ocean radiative budget (Morel and Antoine, 1994).

The understanding of the two-way interactions between physical climate and marine biogeochemistry is further complicated by the fact that these interactions are simultaneous, characterized by multiple scales, and possibly co-varying to some degree. It is therefore useful to analyze these interactions within coupled climate models, which interactively simulate the dynamical evolution of the ocean, atmosphere, sea ice, and marine biogeochemistry in an interactive way. Climate models are capable of internally generating natural climate variability and of reasonably simulating the major large-scale processes occurring within the Earth System. They are therefore valuable tools, to be used in combination with observational data sets, for investigating interactions between physical climate and marine biogeochemistry under present climate and future projections of increased greenhouse gases.

In this PhD thesis I focus on three particular aspects of the vast range of bio-physical interactions occurring within the Earth System:

1. **The response of marine biogeochemistry to the North Atlantic Oscillation and to North Pacific climate variability (arrow 1).**

2. **The combined impacts of natural climate and anthropogenic forcing on marine biogeochemistry in the North Pacific (arrows 1 and 2).**

3. **The climate feedbacks of solar radiation absorption by phytoplankton (arrow 3).**

These aspects are thought to be relevant for improving the scientific understanding of Earth System functioning and its temporal evolution. The interrelated, simultaneous, and bi-directional nature of the bio-physical processes requires a comprehensive approach considering the various aspects of this interaction as part of a unitary and coupled system. In this PhD thesis I have consequently used a coupled ocean-

atmosphere model containing interactive marine biogeochemistry to investigate two-way interactions between climate and marine biogeochemistry within the Earth System.

The following topics will be addressed:

- Chapter 2 describes the coupled model employed to investigate the main PhD questions, the model development performed within the PhD, and the experiments conducted in this work; subsequently, the model climatological outputs are be analyzed in comparison with available observations.

- Chapter 3 analyzes the feedbacks exerted by ocean phytoplankton radiative heating on global climate. The investigations are carried out in the areas where the bio-optical feedbacks have a larger effect on the physical climate, in order to better identify underlying mechanisms.

- Chapter 4 investigates physical and biogeochemical ocean responses to the North Atlantic Oscillation. It focuses on analyzing the marine biogeochemical responses on interannual to decadal time scales and on identifying the driving processes.

- Chapter 5 explores and compares the impacts of natural and anthropogenic climate change on marine biogeochemistry in 20th and 21st century simulations.

- Chapter 6 summarizes the main findings and concludes on the main perspectives that this work opens.

Chapter 2

Methods

2.1 Coupled model description

The fully coupled global models used in this study are two: the first one is a carbon cycle model containing ocean, atmosphere, sea ice, marine biogeochemistry, and land surface compartments (for a technical description see Fogli et al., 2009); the other one is identical to the first one except for not containing the land surface compartment.

The atmosphere general circulation model is ECHAM5 (Roeckner et al., 2003), which numerically solves the primitive equations for the atmospheric general circulation on a sphere. The horizontal triangular truncation used is T31, corresponding to an approximate 3.75º horizontal grid spacing. In the vertical a flexible coordinate is used, enabling the ECHAM5 model to use either terrain-following sigma or hybrid coordinates, with a total of 19 vertical levels.

The ocean general circulation model OPA 8.2 (Madec et al., 1998) solves primitive equations on the global curvilinear and tripolar ORCA2 grid (Madec and Imbard, 1996). The model has a horizontal resolution of $2º \times 2º \cos\theta$ except for the tropical belt between 20ºS and 20ºN, where grid spacing is reduced to 0.5°. The model has 31 unevenly spaced vertical levels with increasing resolution up to 10 m in the upper thermocline. Vertical eddy diffusion of momentum and tracers is parameterized according to a 1.5 turbulent closure model based on a prognostic equation for the turbulent kinetic energy (Blanke and Delecluse, 1993). The mixed layer depth is then computed diagnostically as the depth at which density is 0.1 kg m^{-3} higher with respect to surface values. In case of vertical density instability, vertical diffusivity is artificially enhanced to 100 m^2 sec^{-1} in order to parameterize convective adjustment. The horizontal diffusion of momentum is parameterized with a Laplacian operator and a 2-D spatially-varying kinematic viscosity coefficient set to 40000 m^2 sec^{-1} poleward of 20°N and 20°S and in the western boundary regions, and gradually decreasing to 2000 m^2 sec^{-1} in the equatorial region. The horizontal diffusion of tracers is computed by means of a harmonic operator along isopycnal surfaces with an eddy diffusivity coefficient equal to 2000 m^2 sec^{-1}. The

model implements an eddy-induced velocity parameterization (Gent and McWilliams, 1990) with coefficient values depending on the growth rate of baroclinic instabilities and usually varying between 15 and 3000 $m^2 s^{-1}$. Ocean and atmosphere exchange of momentum, heat, and freshwater fluxes is provided once a day by means of the OASIS3 coupler (Valcke et al., 2004). Heat and freshwater conservation are ensured by the OASIS3 coupler without the addition of flux corrections. However, since river runoff is climatologically prescribed, excess freshwater or salt is equally redistributed on the global ocean on a daily basis.

The ocean model includes the thermodynamic-dynamic sea ice model LIM (Timmermann et al., 2005). Sensible heat storage and vertical heat conduction within snow and ice are determined by a three-layer model (one layer for snow and two layers for ice). Vertical and lateral changes of sea ice are obtained from prognostic energy budgets at the vertical boundaries of the snow-ice cover. For the momentum balance, sea ice is considered as a two-dimensional continuum in its dynamical interaction with atmosphere and ocean.

The ocean model contains the marine biogeochemistry model PELAGOS (Vichi et al., 2007a) which is the global implementation of the Biogeochemical Flux Model (BFM, http://bfm.cmcc.it). A model assessment against observational datasets is presented in Vichi et al. (2007b) for a climatological simulation and in Vichi and Masina (2009) for an interannual simulation forced with observed atmospheric fluxes. The model includes a comprehensive set of marine biogeochemistry relations for major inorganic and organic compounds and for the lower trophic levels of the marine ecosystem. Three phytoplankton groups (diatoms, nano- and picophytoplankton), three zooplankton groups (nano-, micro- and mesozooplankton) and one bacterioplankton group are described according to their physiological requirements and feeding interactions. Diatoms are the largest phytoplankton group, having high nutrient requirements, elevated growth rates, and being grazed by mesozooplankton. In this model, diatoms are the dominant phytoplanktonic group in the Equatorial Pacific and at subpolar and mid-latitudes, whereas the smaller-sized nano- and picophytoplankton dominate subtropical and tropical domains. Nutrient uptake is parameterized following a Droop kinetics (Vichi et al., 2007a) which allows for multi-nutrient limitation and variable internally-regulated nutrient ratios. Chlorophyll synthesis is down-regulated when the rate of light absorption exceeds the utilization of photons for carbon fixation (Geider et al., 1997).

Living groups excrete, in different quantities, dissolved and particulate organic carbon, which bacterioplankton remineralizes into dissolved inorganic compounds. Particulate organic carbon, mainly produced by the largest phyto- and zooplankton, is parameterized as sinking through the water column with a constant speed of 5 m day^{-1}.

Solar radiation in the climate model is the sum of visible and infrared wavelengths, absorbed by the ocean according to the Paulson and Simpson (1977) double exponential formulation:

$$I(x, y, z) = I_0(x, y) \left[R e^{k_{IR} z} + (1 - R) e^{k_{VIS} z} \right], \tag{2-1}$$

where z is the vertical coordinate oriented upwards between the bottom depth where $z = -H$ and the surface where $z = 0$, I is irradiance at depth z, I_0 is the spatially-varying incoming solar radiation at the ocean surface, R the partitioning between infrared (58%) and visible (42%) wavelengths, and k_{IR} and k_{VIS} the infrared and visible attenuation coefficients typical of clear open ocean waters (Jerlov, 1968). Whereas infrared radiation is totally absorbed in the first model layer, visible radiation may reach ~100 m depth (corresponding to an attenuation depth for shortwave radiation equal to 23 m). When ocean biogeochemistry is present, the ability of visible radiation of penetrating at depth is dependent also on chlorophyll pigments (and to a lesser extent on detrital matter) which strongly absorb in the short-wavelength. The coefficient k_{VIS} is then computed at each depth z as the sum of the constant seawater absorption coefficient k_w (set to 0.043 m^{-1}, i.e. the inverse of the attenuation depth) and of the biological attenuation coefficient k_{bio} (Vichi et al., 2007a) integrated down to depth z:

$$k_{VIS}(z) = k_w + \frac{1}{z} \int_z^0 k_{bio}(z') \, dz' \tag{2-2}$$

$$k_{bio}(z) = c_p P(z) + c_R R(z) \tag{2-3}$$

In Eq. (2-3) P and R are the chlorophyll and detrital matter concentrations at each depth z, and c_p and c_R their respective specific absorption coefficients (0.03 m^2 mg^{-1} for chlorophyll and 10^{-4} m^2 mg^{-1} for detritus).

Radiation absorption by seawater and biological matter causes local radiative heating in the ocean according to the following formula:

$$\frac{\partial T}{\partial t} = \frac{1}{\rho\, C_P} \frac{\partial I}{\partial z} \; , \qquad\qquad (2\text{-}4)$$

where $\partial T/\partial t$ is the temperature variation in time, ρ is ocean density, and C_P the ocean heat capacity (4×10^3 J K^{-1} kg^{-1}). The radiative heating term in Eq. (2-4) is added to the ocean temperature trend equation aside heat advection and diffusion.

In the version of the coupled climate model containing land surface, the land and vegetation model SILVA (Alessandri, 2006) is used to simulate soil hydrology and thermodynamics, snow, and vegetation processes relevant to climate. The model computes land surface characteristics such as albedo, roughness length, conductance, and evapo-transpiration as a function of the soil water content and vegetation state. The addition of a land and vegetation component to the atmosphere-ocean-sea ice-marine biogeochemistry coupled model allows for a closure of the global carbon cycle.

2.2 Model development

As part of the PhD thesis, a full description of the dissolved inorganic carbon (DIC) dynamics was incorporated inside PELAGOS in order to adequately simulate the ocean components of the carbon cycle. In the ocean, inorganic carbon exists in three different forms: free carbon dioxide $\left([CO_2] = [CO_2]_{aq} + [H_2CO_3]\right)$, bicarbonate ion ($HCO_3^-$), and carbonate ion ($CO_3^{2-}$). The carbonate species reach the following equilibrium:

$$CO_2 + H_2O \xleftrightarrow{\;K_1\;} HCO_3^- + H^+ \xleftrightarrow{\;K_2\;} CO_3^{2-} + 2H^+ \qquad\qquad (2\text{-}5)$$
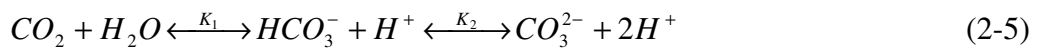
defined by the equilibrium constants K_1 and K_2 for the first and second reaction respectively (Zeebe and Wolf-Gladrow, 2001). The carbonate system in seawater is described in terms of 7 chemical species, i.e., free carbon dioxide, bicarbonate ion, carbonate ion, carbon dioxide partial pressure in seawater (pCO_2), hydrogen ion concentration $(pH = -\log_{10}([H^+]))$, total carbon concentration (DIC), and total alkalinity (TA), which are governed by the following relations:

$$K_1 = \frac{[HCO_3^-] \cdot [H^+]}{[CO_2]} \qquad\qquad (2\text{-}6)$$

$$K_2 = \frac{[CO_3^{2-}] \cdot [H^+]}{[HCO_3^-]} \tag{2-7}$$

$$DIC = [CO_2] + [HCO_3^-] + [CO_3^{2-}] \tag{2-8}$$

$$pCO_2 = \frac{[CO_2]}{K_0} \tag{2-9}$$

$$TA = [HCO_3^-] + 2[CO_3^{2-}] + [B(OH)_4^-] + [OH^-] + [HPO_4^{2-}] + 2[PO_4^{3-}] + \ldots$$

$$+ [H_s SiO_4^-] - [H^+]_F - [HSO_4^-] - [HF] - [H_3 PO_4]. \tag{2-10}$$

The species appearing in Eq. (2-10) are expressed in terms of their equilibrium constants and of their elemental concentrations. Total alkalinity is therefore computed as a function of:

$$TA = f\left([H^+], DIC, K_1, K_2, K_w, K_b, K_{1p}, K_{2p}, K_{3p}, K_{si}, K_s, K_f, bt, st, pt, ft, sit\right) \tag{2-11}$$

where K_1 and K_2 are the equilibrium constants for carbonic acid and bicarbonate ion calculated as a function of temperature and salinity according to Roy et al. (1993); K_0 is the Henry's constant which regulates CO_2 solubility in seawater and it is calculated according to Weiss (1974) as a function of temperature; K_w is the ion product of seawater calculated according to Millero (1995) using composite data recommended Dickson and Goyet (1994); K_b is the dissociation constant for boric acid $(B(OH)_3)$ calculated according to Millero (1995); K_{1p}, K_{2p}, and K_{3p} are the dissociation constants for phosphoric acid (H_3PO_4), dihydrogen phosphate ion $(H_2PO_4^-)$ and hydrogen phosphate ion (HPO_4^{2-}) respectively, calculated according to Millero (1995); K_{si} is the dissociation constant for silicic acid $(Si(OH)_4)$ computed according to Millero (1995); K_s is the dissociation constant for bisulphate ion (HSO_4^-) calculated according to Dickson (1990); K_f is the dissociation constant for hydrogen fluoride (HF) calculated according to Dickson and Riley (1979) converting to total "hydrogen" scale as in Dickson and Goyet (1994). The species bt is the total boron concentration $([B(OH)_3] + [B(OH)_4^-])$ calculated according to Uppstrom (1974), st is the total sulphate concentration $([HSO_4^-] + [SO_4^{2-}])$ calculated according to Morris and Riley (1966), and ft is the total fluoride concentration $([HF] + [F^-])$ calculated according to Riley (1965). The species pt, i.e. the total phosphorus concentration

9

$\left([H_3PO_4] + [H_2PO_4^-] + [HPO_4^{2-}] + [PO_4^{3-}]\right)$, and sit, i.e. the total silica concentration $\left([Si(OH)_4] + [H_3SiO_4^-]\right)$, are model state variables. The fore mentioned calculations have been performed following the US Department of Energy (DOE) "Handbook of Methods for the Analysis of the Various Parameters of the Carbon Dioxide System in Seawater" (Dickson and Goyet, 1994), with the application of the total "hydrogen" scale for all computations. A pressure correction on each of the equilibrium constants is applied following Millero (1995) and Zeebe and Wolf-Gladrow (2001).

This system contains 7 unknown variables $\left(DIC, TA, CO_2, HCO_3^-, CO_3^{2-}, H^+, pCO_2\right)$ and is defined by 5 equations (Eqs. 2-6 to 2-10). The system is therefore determined when two of the seven variables are known: in this case these are total inorganic carbon (DIC), varying as a function of physical and biogeochemical processes, and alkalinity (TA), varying as a function of physical processes only, as biogeochemical processes leading to alkalinity changes (i.e. calcium carbonate production and dissolution, and riverine inputs of alkalinity) are not implemented in the model. The local equilibrium carbonate chemistry is solved according to the simplified method proposed by Follows et al. (2006) for the computation of $[H^+]$ from which other variables $\left(CO_3^{2-}, HCO_3^-, CO_2, pCO_2\right)$ may then be calculated. The pH value is calculated as $-\log_{10} H^+$.

The difference between atmospheric and surface ocean CO_2 partial pressure drives a CO_2 flux between the ocean and the atmosphere. The air to sea CO_2 transfer over the ocean is parameterized according to Wanninkhof (1992):

$$flux(CO_2)_{air-sea} = K_0 \cdot k_{av} \cdot \left(pCO_{2(air)} - pCO_{2(sea)}\right) \qquad (2\text{-}12)$$

where $pCO_{2(air)}$ and $pCO_{2(sea)}$ are the air and sea CO_2 partial pressures at the atmosphere-ocean interface, K_0 is the fore mentioned solubility coefficient for CO_2 in seawater, and k_{av} is the gas transfer coefficient for steady winds (Wanninkhof, 1992) computed as:

$$k_{av} = 0.3 \cdot u^2 \cdot \left(\frac{Sc}{660}\right)^{-0.5} \qquad (2\text{-}13)$$

where u is the wind speed and Sc is the Schmidt number, defined as the kinematic viscosity of water divided by the diffusion coefficient of the gas, and estimated according to (Wanninkhof, 1992):

$$Sc = 2073.1 - 125.62 \cdot T + 3.6276 \cdot T^2 - 0.043219 \cdot T^3. \qquad (2\text{-}14)$$

The implementation of carbonate chemistry for the closure of the carbon cycle adds 2 dynamically transported variables (total alkalinity and total dissolved inorganic carbon) and 5 diagnostic variables for the carbonate speciation (aqueous CO_2, bicarbonate and carbonate concentrations, pCO_2, pH and ocean-atmosphere CO_2 flux).

2.2   Experiment set up

The coupled model described in Section 2.1 is used to produce a number of simulations which are shown schematically in Fig. 2-1. A coupled simulation containing the physical components only of the coupled model, i.e. atmosphere (ECHAM5), ocean (OPA 8.2) and sea ice (LIM), is named A for "abiotic". Experiment A is initialized with climatological temperature and salinity data from the World Ocean Atlas 1998 (Antonov et al., 1998; Boyer et al., 1998) and is integrated for 400 years. Another coupled simulation is performed with the same physical core as experiment A with the addition of the marine biogeochemistry model PELAGOS and is named B for "biotic". The B experiment is initialized with the physics of the year 100 of the A experiment and integrated further for 300 years. Both experiments A and B are conducted under constant greenhouse gas atmospheric concentrations, i.e. CO_2, CH_4, N_2O, and CFC; in particular, CO_2 concentrations are equal to 348 ppm, a value typical of the 1980s (Fig. 2-2). Marine biogeochemistry in experiment B is initialized as follows: macronutrients, dissolved inorganic carbon and alkalinity are prescribed from World Ocean Atlas 2001 climatologies (Conkright et al., 2002), dissolved iron concentration is initialized as homogeneous zonal bands based on sparse data collected by Gregg et al. (2003) and the remaining variables are set to uniform concentrations, with chlorophyll concentrations computed as a constant ratio of phytoplankton carbon. During the model integration, atmospheric iron deposition is taken into account by applying climatological model data from Tegen and Fung (1994) and assuming a dissolution fraction of 1%.
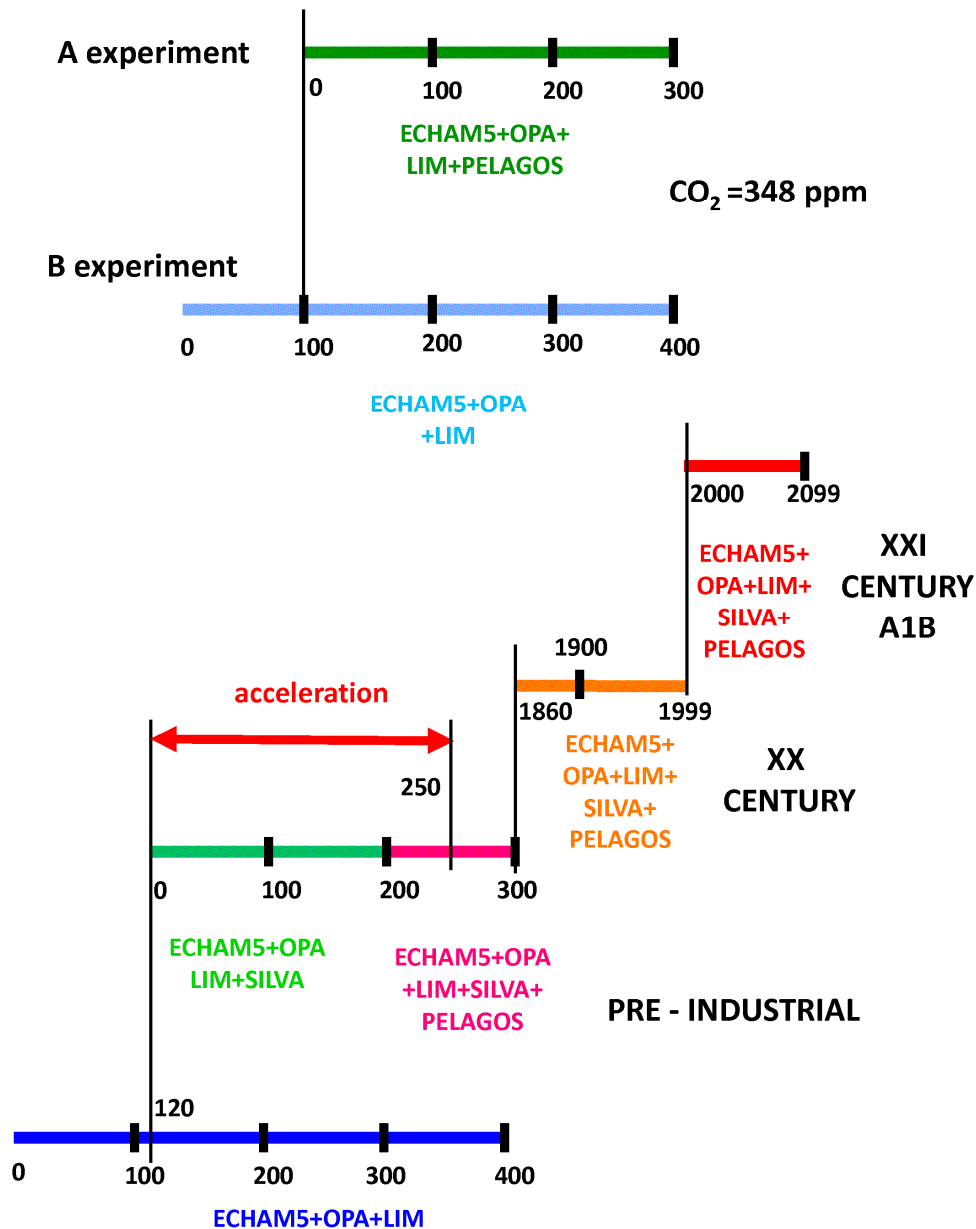
Figure 2-1: Experiments analyzed in this study: in experiments A and B atmospheric CO_2 levels are set to 348 ppm; in the pre-industrial experiments greenhouse gases are set to the climatological value for the year 1860; in the "XX century" experiment greenhouse gases are those observed for the period 1860-1999; in the "XXI century" experiment greenhouse gases are prescribed according to the A1B scenario. Model components, used in different combinations among the simulations, are ECHAM5 (atmosphere), OPA 8.2 (ocean), LIM (sea ice), PELAGOS (marine biogeochemistry), SILVA (land and vegetation).

A set of centennial simulations have been performed within the framework of the EU Project ENSEMBLES (http://ensembles-eu.metoffice.com/). In particular, ENSEMBLES designed a carbon cycle concerted experiment, in which atmospheric greenhouse gases (hereafter GHG) concentrations are used to drive the carbon cycle model instead of GHG emissions, following the simulation strategy proposed by

Hibbard et al. (2007). A number of pre-industrial simulations were performed under climatological GHGs (CO_2, CH_4, N_2O, and CFC), ozone, sulfate, and aerosol concentrations relative to the year 1860, which for atmospheric CO_2 is equal to 286 ppm. A pre-industrial simulation performed with the physical core of the coupled model was initialized following the method by Stouffer et al. (2004) from historical oceanic observations representative of current temperature and salinity distributions (Levitus et al., 1998). Another pre-industrial simulation containing the interactive terrestrial vegetation model SILVA was initialized from the year 120 of the physics-only pre-industrial experiment and integrated for 200 years. This simulation was used to initialize the physics and terrestrial vegetation of another pre-industrial experiment containing the interactive marine biogeochemistry model PELAGOS, where marine biogeochemistry was initialized identically as in the B experiment described above.

In order for the ocean and terrestrial biosphere carbon pools to equilibrate with preindustrial atmospheric CO_2 concentrations, an artificial acceleration method was performed, similarly to Alessandri (2006); specifically for the ocean, the global ocean-atmosphere CO_2 fluxes drive an artificially enhanced ocean outgassing where the excess carbon is removed homogeneously from the oceanic inorganic carbon pool. After the oceanic carbon pools have reached equilibrium with atmospheric GHGs, the simulation is continued for another 50 years and used to initialize a historical 1860-1999 century simulation containing all model components, and forced with observed atmospheric concentrations of atmospheric GHGs, sulphates, ozone, and aerosols (made available within the ENSEMBLES multi-model experiment). The year 1999 of the XX century is used to initialize a XXI century projected climate simulation performed with all components of the coupled model. Time-varying GHGs, sulphate, ozone, and aerosol concentrations are prescribed employing the Intergovernmental Panel on Climate Change (IPCC) Special Report on Emissions Scenarios (SRES) "business-as-usual" A1B scenario (Nakicenovic and Swart, 2000). The time evolution of atmospheric CO_2 concentrations during 1860-1999 and for the A1B scenario is shown in Figure 2-2.
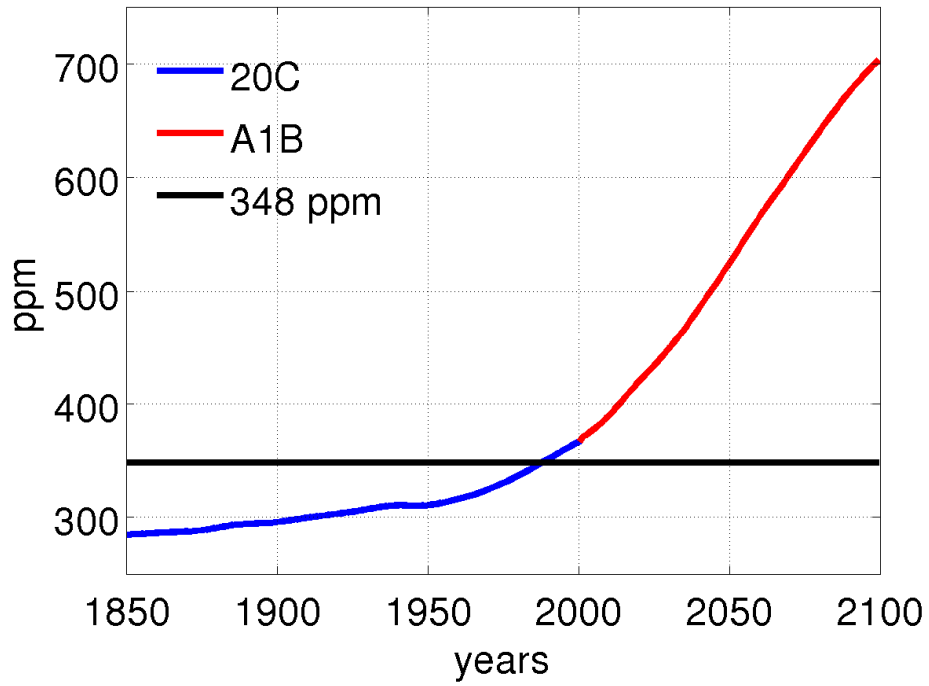
Fig. 2-2: Time evolution of prescribed atmospheric CO_2 concentrations in the A and B simulations, i.e. 348 ppm(black), for the 20th century simulation, i.e. those observed during the years 1860-1999 (blue), and for 21st century simulation according to the A1B scenario (red).

2.3 Model climatology and biases

Model climatologies are analyzed over the last 150 years of the B experiment and over the last 30 years of the XX century simulation, and compared with observational data sets. Fig. 2-3 shows in colors the annual SST bias with respect to 1950-2002 Hadley SST (Rayner et al., 2003) and the climatology of each experiment in contours. In the B experiment SST exhibits negative biases in the central equatorial Pacific (~2°C), in the northwestern North Atlantic (~6°C), in the northern Pacific subtropical gyre (~2°C) and in the Southern Ocean between 30°-60°S (2-3°C), and positive biases in the eastern tropical basins (~4°C) and in the North Pacific at around 45°N (~5°C). The last 30 years of the XX century exhibit similar spatial patterns even though the ocean surface is significantly colder. This counterintuitive result is due to the fact that sulfate aerosol concentration, exerting a negative feedback on surface temperatures, is higher in the last 30 years of the XX century than in the B experiment.
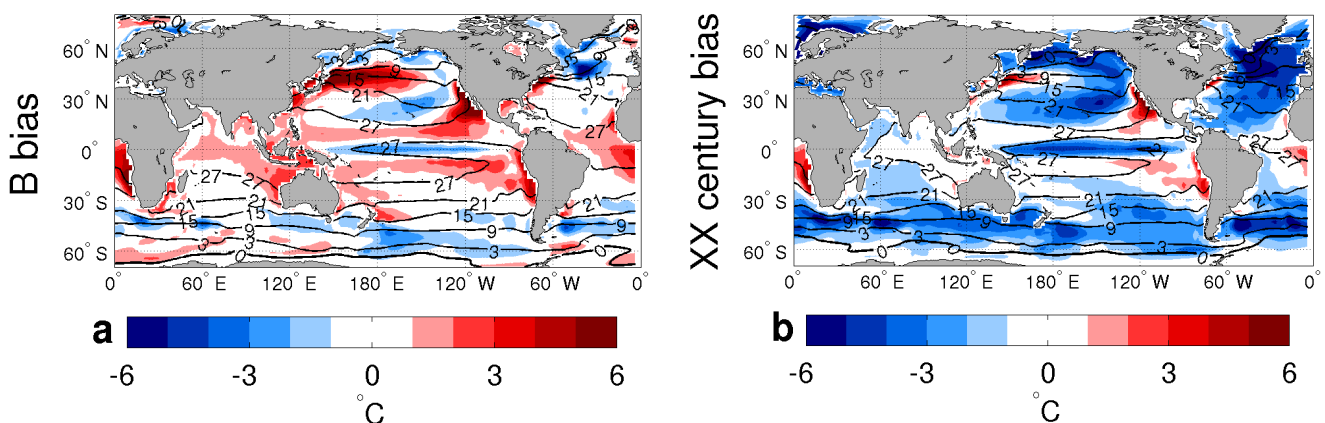

Fig. 2-3: Colors: Annual SST model bias (°C) with respect to Hadley SST, contours: model climatology; **(a)** B experiment, **(b)** last 30 years of the XX century.

Annual precipitation simulated in the B and XX century experiments is compared with Climate Prediction Center Merged Analysis of Precipitation (CMAP) estimates for 1979-2002 (Xie and Arkin, 1996) in Fig. 2-4. The model is capable of capturing the main features of the precipitation field even though precipitation in the Tropics is slightly overestimated and affected by the presence of a double Intertropical Convergence Zone (hereafter ITCZ), and over the North Atlantic and North Pacific storm tracks tend to be shifted more poleward than observed.

Similarly to other coarse resolution coupled simulations (Meehl et al., 2007), the SST and precipitation biases shown in Figs. 2-3 and 2-4 originate from issues regarding model physics, air-sea coupling and grid resolution. In particular, in the eastern tropical Pacific and Atlantic basins the misrepresentation of low stratus clouds and of deep convection processes could account for some of the SST and precipitation biases (Lin, 2007), whereas overly strong easterlies, simplified formulations of air-sea momentum fluxes (Jungclaus et al., 2006; Guilyardi et al., 2009) and reduced tropical instability wave activity are the likely cause for cold bias in the central equatorial Pacific. The North Atlantic negative SST bias is mostly related to the displaced pathways (Fig. 2-5) of the Gulf Stream and the North Atlantic Current (Reverdin et al., 2003) which reduce heat transport into the subpolar gyre.
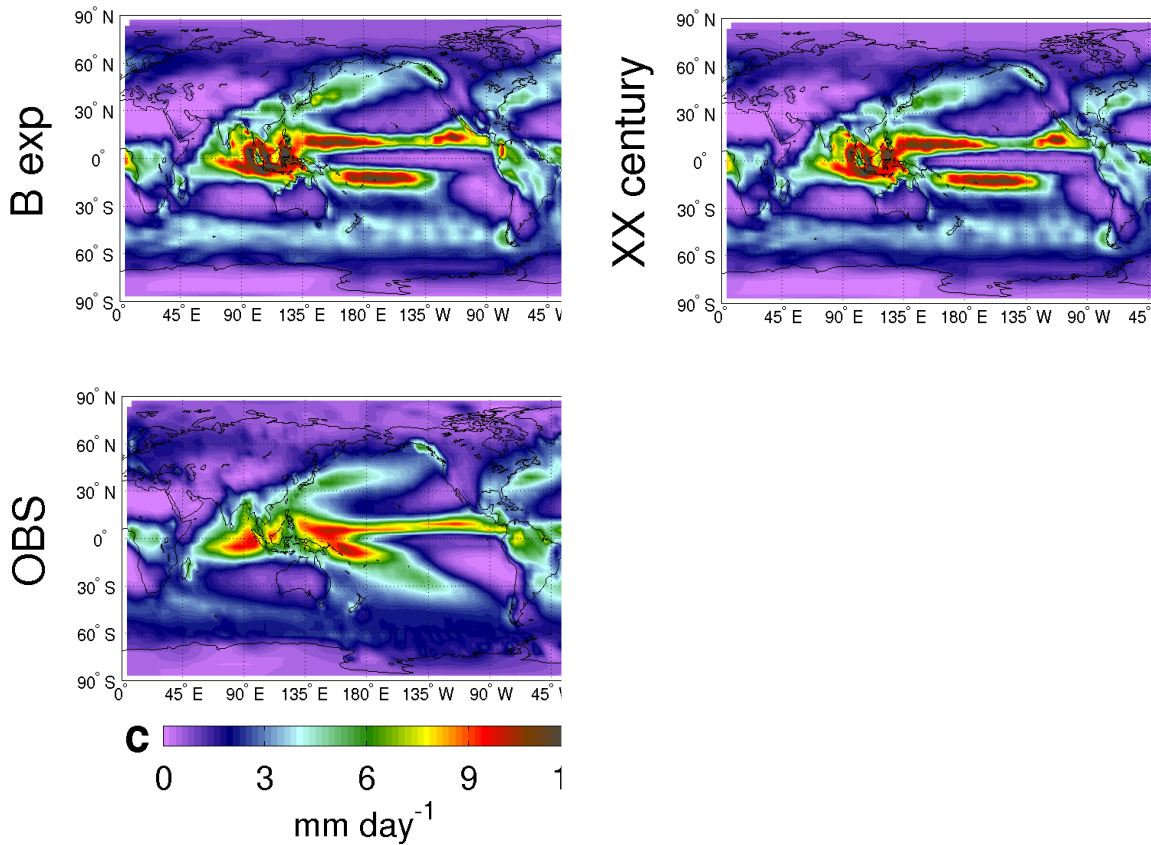

Fig. 2-4: Simulated annual precipitation (mm day^{-1}) in **(a)** B experiment, **(b)** last 30 years of the XX century **(c)** CMAP estimates.
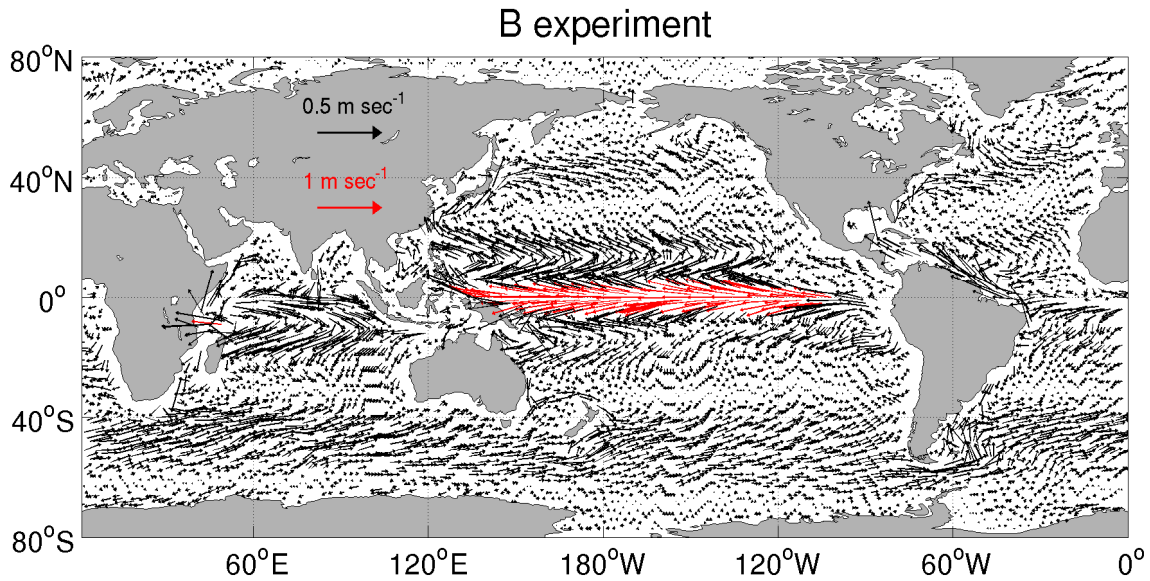
Fig. 2-5: B experiment annual surface currents (m sec^{-2}). Currents having a magnitude exceeding 0.65 m sec^{-1} are scaled of a factor 2 for better visualization (red arrows).

Annual wind stress biases with respect to ERA-40 reanalysis (Uppala et al., 2005) are shown in Fig. 2-6 for B and XX century experiments. In both the experiments, easterly trade winds in the northern subtropical Pacific are overestimated (up to 0.1 N m^{-2}), and mid-latitude westerlies are poleward-shifted in the Northern Pacific and equatorward-shifted in the Southern Ocean. Wind biases are possibly originating from inaccurate meridional SST gradients which affect vertical shears of zonal winds through the thermal wind relation (Holton, 1992). Annual latent heat fluxes are compared with NCEP reanalysis (Kalnay et al., 1996), and their biases shown in Fig. 2-7 for B and XX century experiments together with their climatological values, where positive values indicate ocean heat gains. Latent heat losses tend to be overestimated where SST values are overestimated (e.g. subtropical gyres, Kuroshio extension region in the western North Pacific), whereas they tend to be underestimated where SST values are lower than observed (e.g. subpolar North Atlantic, equatorial Pacific).
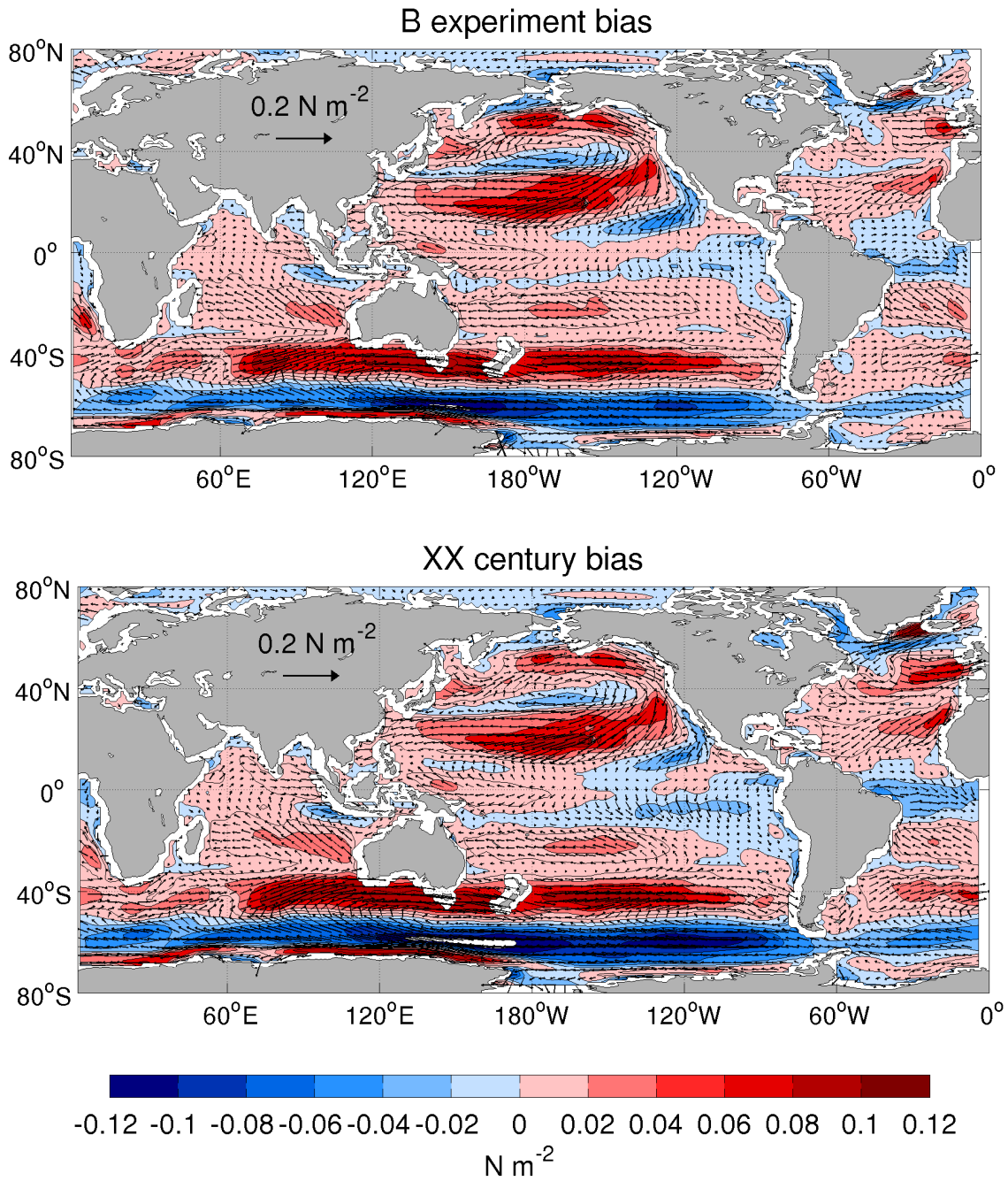
Fig. 2-6: Simulated annual wind stress bias (N m^{-2}) with respect to ERA-40 reanalysis (colors indicate magnitude) and model climatology (contours); **(top)** B experiment, **(bottom)** last 30 years of the XX century.
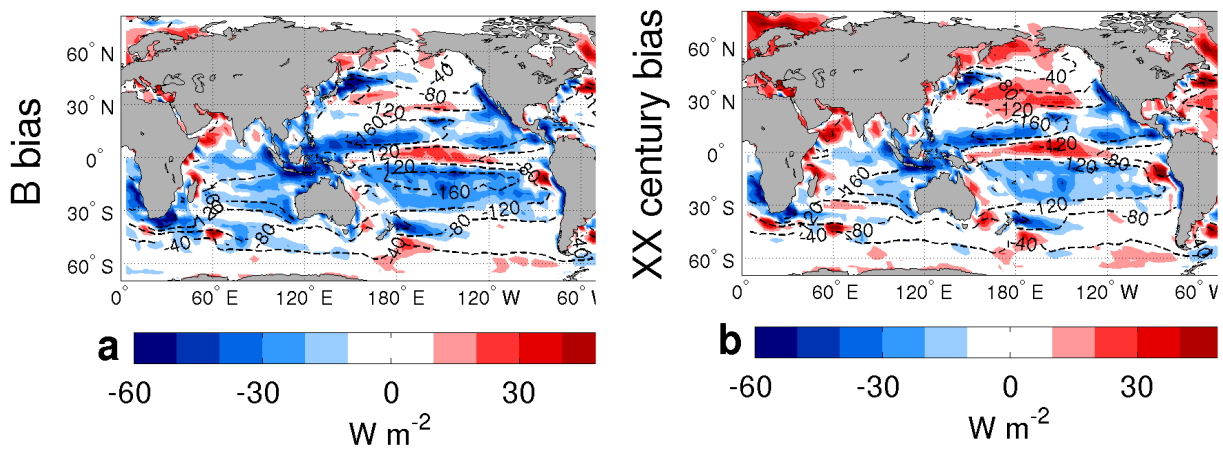
Fig. 2-7: Simulated annual latent heat flux bias (W m^{-2}) with respect to NCEP reanalysis (colors) and model climatology (contours); **(a)** B experiment, **(b)** last 30 years of the XX century.
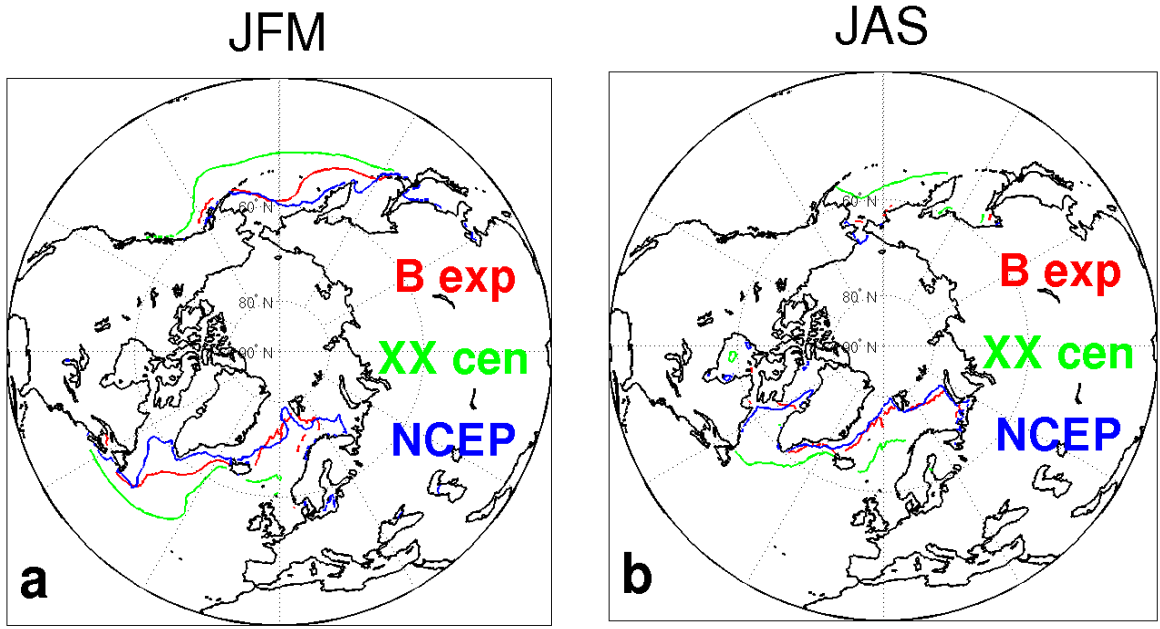
Fig. 2-8: sea ice edge, diagnosed as 1% sea ice cover for B experiment (red), last 30 years of the XX century experiment (green), NCEP reanalysis (blue) in January-March **(JFM, left)** and July-September **(JAS, right)**.

The northern hemisphere sea ice edge, diagnosed as 1% sea ice cover, in B and XX century simulations is shown in Fig. 2-8 together with the NCEP reanalysis data (Kalnay et al., 1996) for winter (JFM) and summer (JAS) months. In the B experiment winter sea ice is generally overestimated in the Labrador Sea and in the western North Pacific whereas it is rather well simulated in summer. In the XX century sea ice is

highly overestimated in both the North Atlantic and North Pacific basins in relation to negative SST biases in the northern hemisphere (Fig. 2-3b).
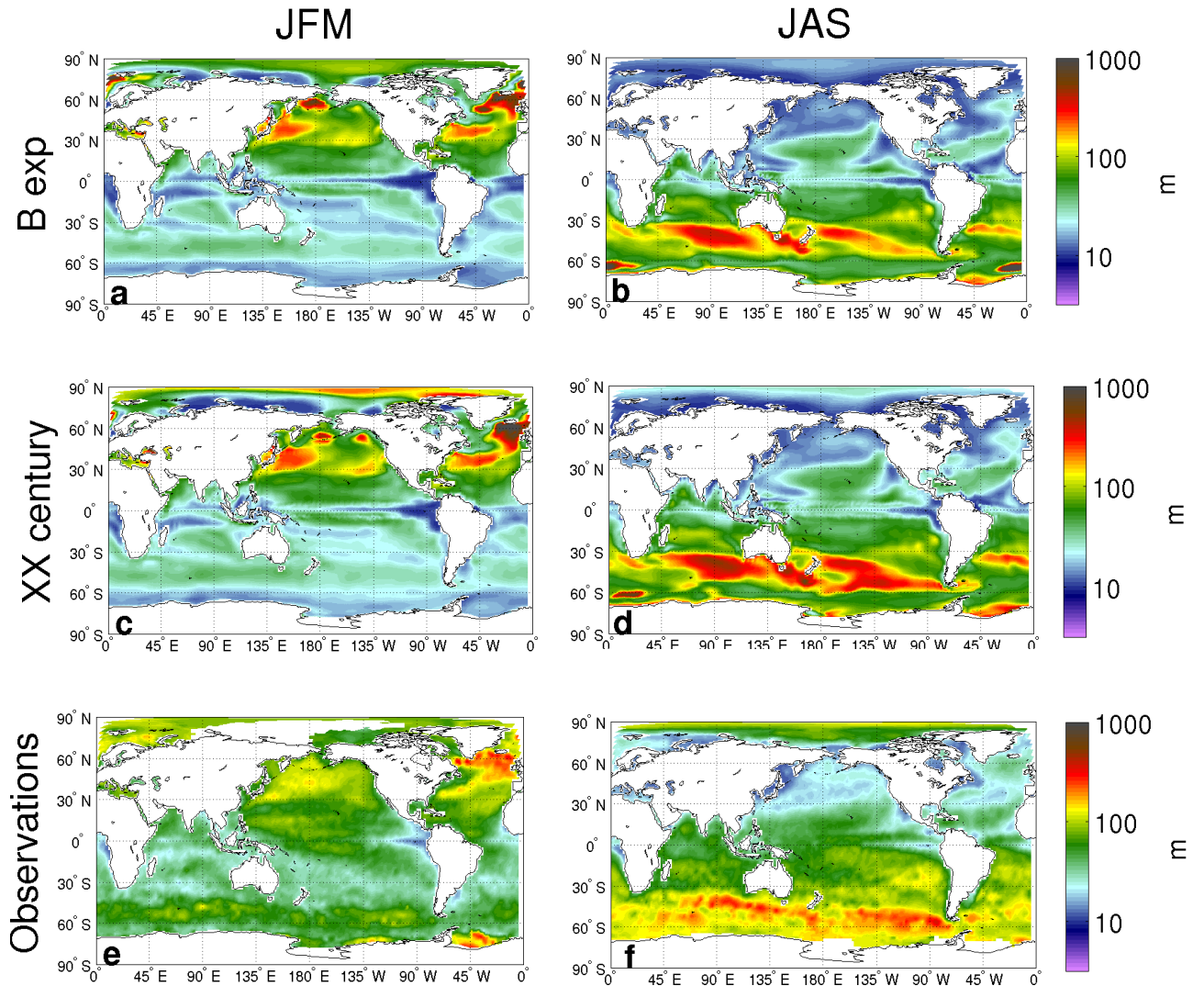

Fig. 2-9: Mixed layer depth (m) plotted in logarithmic scale in January-March (JFM, left) and July-September (JAS, right) for **(a,b)** B experiment, **(c,d)** XX century experiment, and **(e,f)** de Boyer-Montégut et al. (2004) observational estimates.

Mixed layer depth (MLD) in B and XX century experiments is shown in logarithmic scale in Fig. 2-9 for January-March (JFM) and July-September (JAS) and compared with de Boyer-Montégut et al. (2004) estimates. It is to be remarked that MLD in the model is computed diagnostically as the depth at which ocean density is 0.1 kg m^{-3} higher than the surface, whereas in de Boyer Montégut et al. (2004) it is diagnosed as the depth at which temperature is 0.2 °C lower than the surface. As discussed by de Boyer Montégut et al. (2004), the temperature criterium is more suitable because of

higher spatial coverage of observational data and because it detects boundaries between density-compensated water masses. However MLD values calculated with two different methods (de Boyer Montégut et al., 2004) yield sufficiently similar results for the purpose of the present comparison. When compared with observational estimates, both the B and the XX century simulations show overestimation of JFM MLD in the Atlantic Nordic Seas and in the subpolar North Pacific, and underestimation in the Labrador Sea, the latter caused by overestimated sea ice (Fig. 2-8). In the Southern Ocean MLD is generally underestimated south of 60°S in both JFM (austral summer) and JAS (austral winter), and overestimated equatorward of 60°S in JAS (austral winter). The equatorward shift of MLD maximum in the Southern Ocean is possibly related to the incorrect equatorward displacement of westerly winds (Fig. 2-6).

Annual chlorophyll concentrations averaged over the euphotic layer depth in B and XX century experiments are shown in logarithmic scale in Fig. 2-10 and compared with SeaWiFS satellite estimates (McClain, 2009) and with World Ocean Atlas (Conkright et al., 2002) data averaged over the first 100 m depth. The main features of the chlorophyll field are correctly represented by the model simulation, in terms both of magnitude and of spatial structure, i.e. chlorophyll values are higher in subpolar regions (up to 0.5 mg m^{-3} in the North Pacific and Southern Ocean, up to 0.2 mg m^{-3} in the North Atlantic) and in the Tropics (up to 0.3 mg m^{-3} in the equatorial Pacific), and are lower at subtropical latitudes. However it may also be seen that chlorophyll values are underestimated at subtropical latitudes in both hemispheres, whereas they are overestimated south of 40°S in the Southern Ocean. In the North Atlantic Ocean chlorophyll values tend to be underestimated, even though the seasonal maximum is correctly captured in terms of both timing and amplitude (Fig. 2-11).
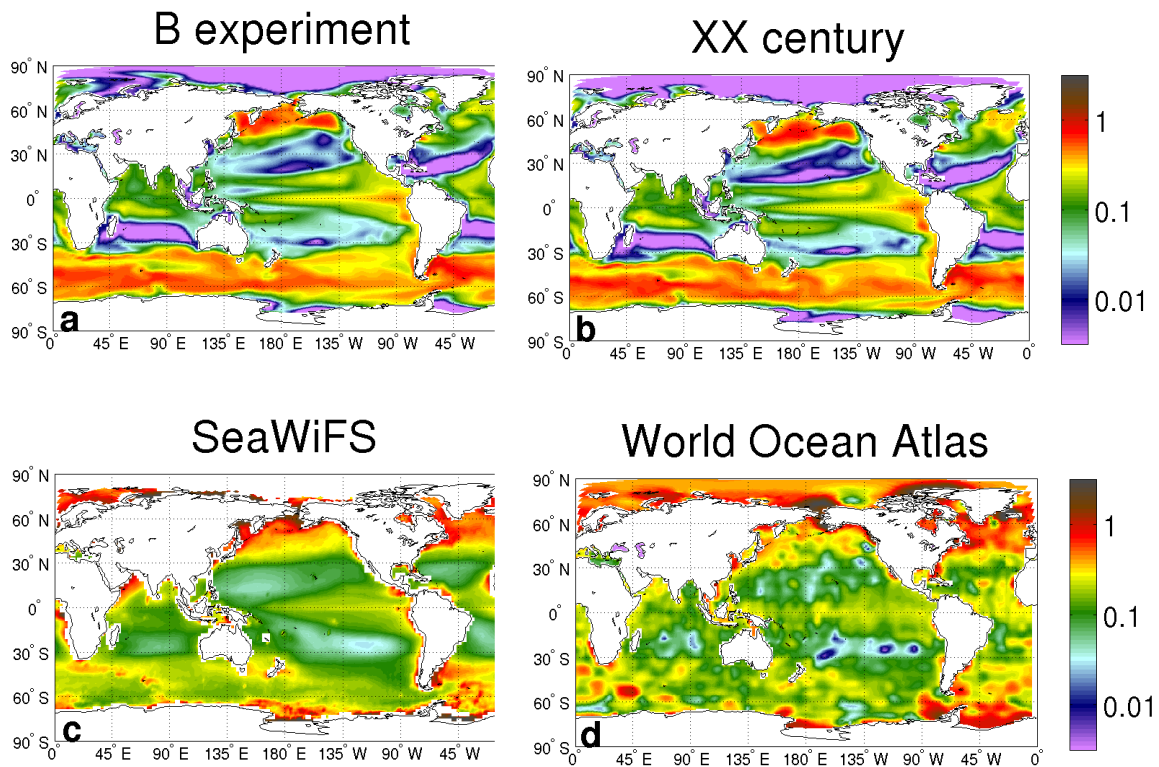
Fig. 2-10: Annual chlorophyll concentration in the euphotic layer (mg m^{-3}) plotted in logarithmic for the **(a)** B experiment, **(b)** last 30 years of the XX century experiment, **(c)** SeaWiFS satellite estimates and **(d)** World Ocean Atlas observational data.

The reasons for the biases in the chlorophyll mean state arise from inaccuracies in both physical and biogeochemical models. For instance, the positive bias in the Southern Ocean is related to an inadequate representation of the mixed layer seasonal cycle, which is too deep in the winter months and too shallow in the subsequent summer months (Fig. 2-9). Moreover the equatorward displacement of the MLD maximum impacts the spatial distribution of the chlorophyll maximum as well. The chlorophyll underestimation in the subpolar North Atlantic Ocean is probably related to a number of reasons: (1) winter chlorophyll values are lower-than-observed because of the overestimated depth of the winter mixed layer (Fig. 2-11) which exerts a light limitation on phytoplankton growth; (2) the lower-than-observed summer values are related to underestimated nutrient concentrations (not shown) which are largely consumed and exported from the euphotic layer depth during the spring months; (3) in the course of the whole 300-year model integration, surface nutrient and chlorophyll values exhibit a systematic decrease, possibly caused by an overly strong export of nutrients from the surface layers into deeper ocean layers, where they are likely conveyed by the meridional overturning circulation towards south. This behavior may be seen in Fig. 2-

12a showing a time series of B experiment chlorophyll concentration integrated in the euphotic layer and spatially averaged north of 35°N, where it may be seen that chlorophyll values tend to stabilize in the last 100 years of the simulation.
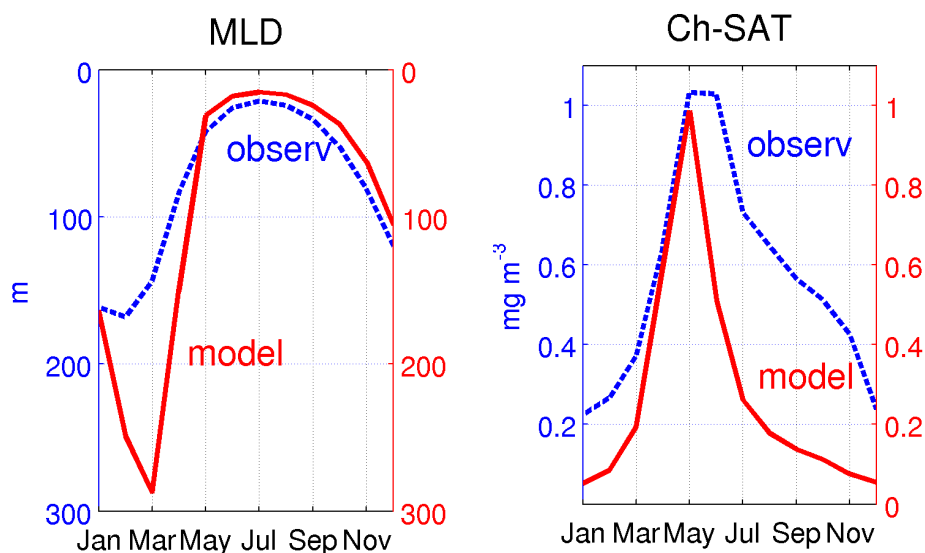

Fig. 2-11 Observed (blue, dashed line) and simulated (red, full line) climatological seasonal cycles, computed over the subpolar North Atlantic. **Left**: mixed layer depth (MLD) in m, where the observed values are from de Boyer Montégut et al. (2004). **Right**: chlorophyll concentration (Ch-SAT) in mg m^{-3}, where observed values are SeaWiFS satellite estimates (McClain, 2009), and simulated values are vertically averaged until the 3rd optical depth.

It needs to be stressed that the goodness of a biogeochemical model lies in its capability of correctly simulating not only mean bulk biogeochemical properties but also the rates at which organic matter is processed within the food web, which influence upper ocean carbon transformation processes and ultimately carbon sequestration in deeper ocean layers. As shown by Vichi and Masina (2009), the PELAGOS model used in this study has skill at simulating net primary production over the global ocean, when compared with satellite-derived estimates and an independent data set of *in situ* observations in the equatorial Pacific.

For the analysis of chlorophyll interannual and decadal variability in the B experiment, characterized by constant atmospheric CO_2 concentrations, it is convenient to have chlorophyll anomaly time series detrended from systematic tendencies unrelated to climate variability. A second order polynomial fit of the last 200 years of the chlorophyll time series is therefore computed at each grid point and its spatial average north of 35°N shown Fig. 2-12a (red line). A fit with an exponential function was also

attempted but it did not give satisfactory results in all parts of the basin. Evidently, various time scales are involved in the adjustment process to initial conditions and thus one cannot assume a simple exponential model of chlorophyll temporal evolution in all grid points. The obtained polynomial coefficients are used to detrend the time series of B experiment chlorophyll concentration at each grid point. From Fig. 2-12b it may be seen that after the detrending operation over the last 200 years of the time series the chlorophyll anomalies oscillate around zero with fluctuations which are then related to climatic variability.
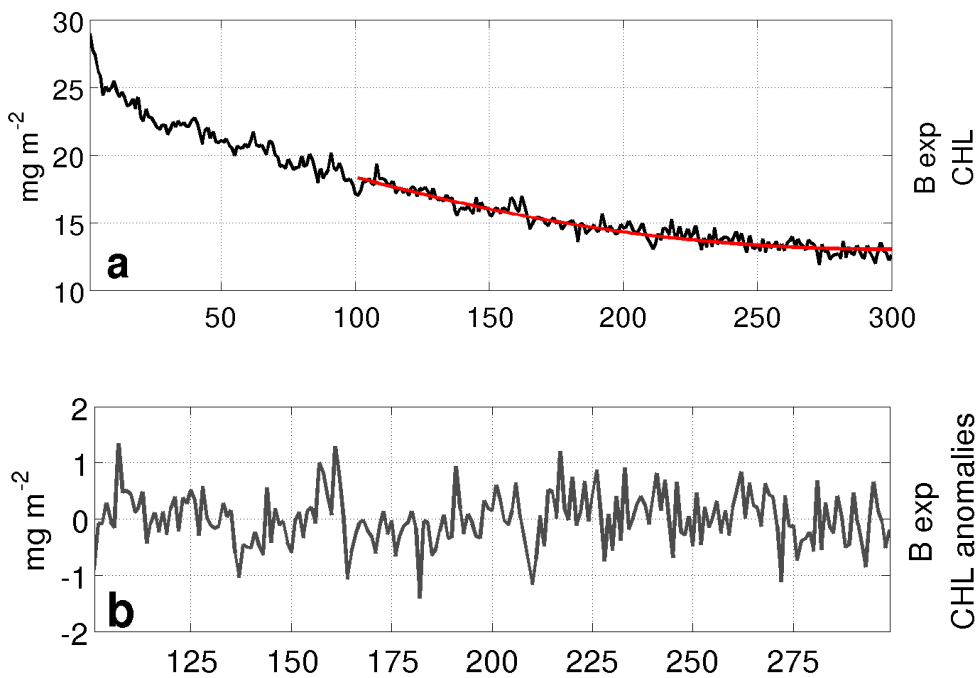
Fig. 2-12: Time series of annual chlorophyll (CHL) concentration integrated in the euphotic layer (mg m^{-2}) and averaged north of 35°N. **(a)** B experiment CHL time series (black) and second order polynomial fit (red) over the last 200 years of simulation, **(b)** last 200 years of the B experiment CHL anomalies after detrending.

For the analysis of the marine biogeochemical response to increased CO_2 concentrations in the XXI century simulations, a polynomial fit of the time series cannot be performed as for experiment B. In fact the changes in surface chlorophyll are likely to be mostly forced by external climate trends. In Fig. 2-13 globally averaged time series of annual chlorophyll concentration values are shown for the pre-industrial simulation (where atmospheric gases and aerosols are climatologically set to the year 1860 values), for the historical simulation (where atmospheric gases and aerosols are those measured during the 1860-1999 period), and for the XXI century projection (where atmospheric gases and aerosols are those estimated by the A1B scenario). It has to be remembered that

marine biogeochemistry was initialized (identically as for the B experiment) at the beginning of the pre-industrial simulation. It may be seen that chlorophyll exhibits a large decrease during the first 100 years simulation, as similarly seen and discussed for the B experiment in the northern hemisphere (Fig. 2-12). Afterwards chlorophyll exhibits a tendency towards stabilization (as in the B experiment) before showing another large drop in the XXI century projection. It is very likely that the first chlorophyll drop in the pre-industrial era, i.e. performed under constant CO_2 concentrations, is due to dynamics internal to the coupled model, whereas the second drop in the XXI century, i.e. after chlorophyll has roughly stabilized, is due to external climate forcing.
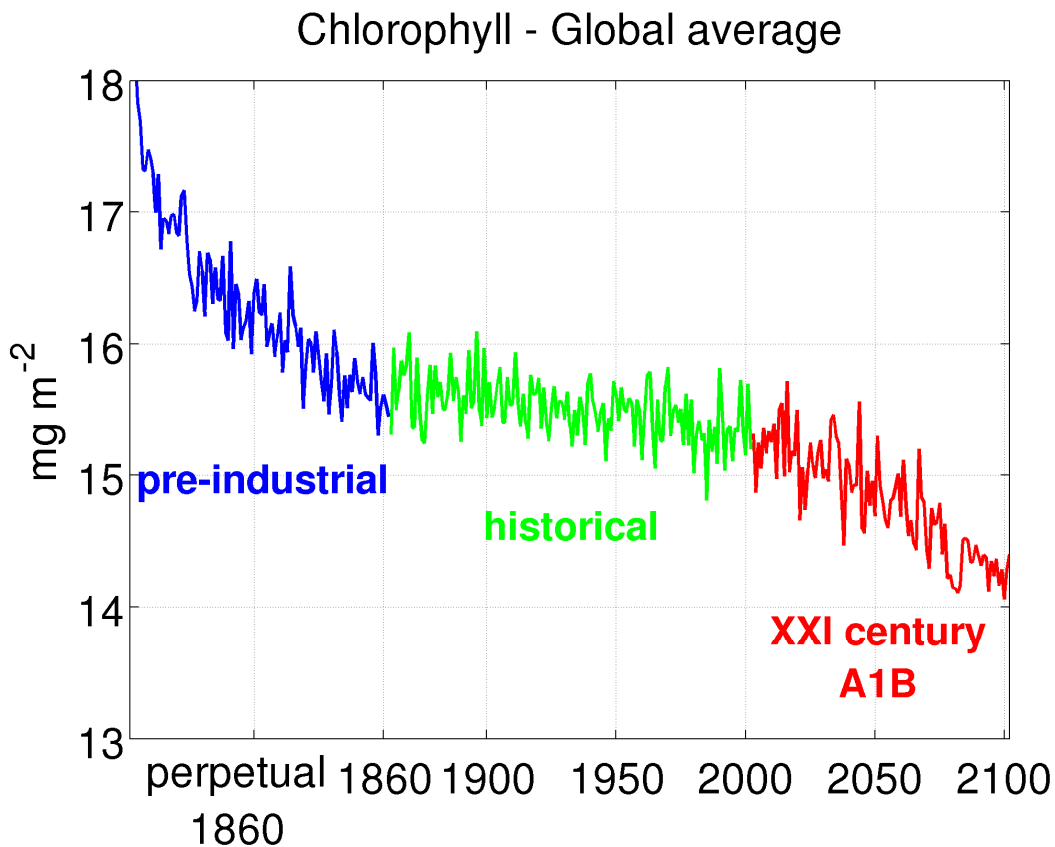
Fig. 2-13 Time series of annual chlorophyll concentration integrated over the euphotic layer depth and averaged over the global ocean (mg m^{-2}) for the pre-industrial simulation (blue), historical simulation from 1860 to 1999 (green), and A1B scenario for the XXI century (red).

Finally, a comparison between the simulated surface CO_2 partial pressure (hereafter pCO_2) in the last 30 years of the XX century and observed pCO_2 data obtained from the Lamont Doherty Earth Observatory (LDEO) dataset (Takahashi et al., 2009a) covering the period 1970-2005 is shown in Fig. 2-14. Observed and simulated data are binned

onto a regular 2x2 degrees grid and annually averaged. The model reproduces the pattern of high pCO$_2$ in the large scale upwelling of the Pacific Ocean, related to entrainment to the surface of carbon-rich subsurface waters. It does not have skill however to reproduce the regions of high pCO$_2$ in the Indian Ocean because of weaker and shallower than observed upwelling, indicating that this area acts as sinks and not as source in the XX century simulation.
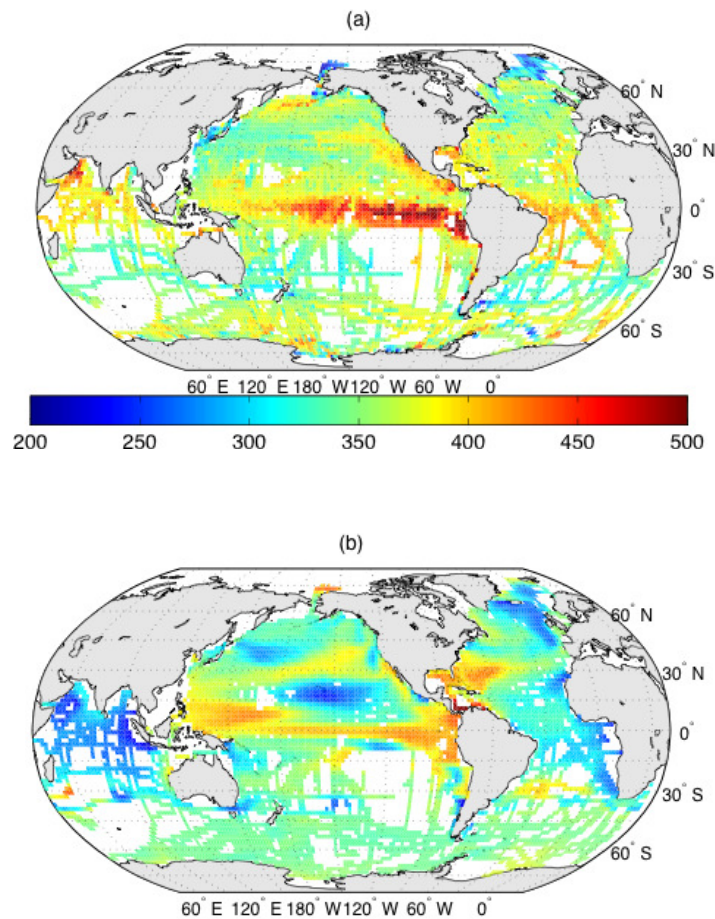
2-14 Maps of 2x2 degrees binned data of surface pCO$_2$ (µatm) from **(a)** LDEO dataset (Takahashi et al., 2009), **(b)** annual climatology of the last 30 years of the XX century simulation. From Vichi et al., 2010 (in preparation).

Chapter 3

Feedbacks of biological radiative heating in a coupled climate model

Summary This study addresses the mechanisms by which upper ocean phytoplankton may generate feedbacks on the global climate by means of solar radiation absorption during photosynthetic reactions. Phytoplankton radiation absorption gives rise to a local radiative heating pattern capable of propagating into the coupled and dynamical climate system and of generating feedbacks onto oceanic and atmospheric properties. Here a coupled model containing interactive marine biogeochemistry is used to perform a 300-year simulation which is compared with a physics-only simulation, thus enabling the analysis of the effects of the addition of biological radiative heating on the physical climate. It is found that in the dynamically coupled climate system the heating perturbation induced by biology propagates within the climate system and generates feedbacks on virtually all its components. A general increase of sea surface temperatures around 0.5°-1°C is accompanied by an enhancement of latent heat losses to the atmosphere which determine increases in atmospheric temperatures and water vapor content up to 6%. The equatorial maximum in biological heating causes an intensification of the Hadley circulation which acts as a teleconnection mechanism affecting cloudiness and solar radiation patterns from tropical to subtropical latitudes. Changes in temperature meridional gradients at extratropical latitudes modify the vertical shear of zonal winds and give rise to anticyclonic anomalies in the mid-latitude atmospheric circulation. Modified atmospheric circulation drives 5-10% modifications in the upper ocean circulation and related heat transports. In response to changes in incoming solar radiation and in ocean circulation, upper-ocean heat content decreases at tropical latitudes and increases at middle latitudes. The biologically-induced modifications in the physical climate might interact with the other sources of internal and external climate variability and might need to be kept into consideration in climate impact studies.

3.1 Introduction

The upper ocean contains a variety of living and dead particles which absorb, scatter and reflect incoming solar radiation (Morel and Antoine, 1994). Among these are chlorophyll pigments which are internal constituents of phytoplanktonic organisms used to absorb visible radiation for photosynthetic reactions. This process interacts with the vertical distribution of shortwave radiation through the water column and thus with the upper ocean heat budget. Bio-optical feedbacks are relevant in the context of climate research as they are virtually ubiquitous and intimately intertwined with time- and space-varying physical forcing factors.

Most climate models use a constant attenuation scale for visible radiation of ~20 m depth which comes from observational estimates of open ocean water clarity (Jerlov, 1968; Paulson and Simpson, 1977). This assumption however does not consider the large variations of bio-optical properties that can be found throughout the ocean on various temporal and spatial scales. For instance, local variations in temperature linked to biological radiative heating in the tropical Pacific were observed to strongly respond to ocean variability associated with El Niño Southern Oscillation (Strutton and Chavez, 2004); using remotely sensed data for the Arabian Sea, Sathyendranath et al. (1991) find that the distribution of phytoplankton, which is mainly governed by upwelling seasonality, exerts a controlling influence on the seasonal evolution of sea surface temperature.

Whereas the local effect of chlorophyll radiation absorption may be measured instrumentally, its full-scale effects on the climate system may only be addressed in modeling studies. A key region is the tropical Pacific, characterized by high chlorophyll concentrations and by pronounced ocean-atmosphere coupling. In forced ocean configurations biological heating was found to affect equatorial sea surface temperatures (Nakamoto et al., 2001; Loeptien et al., 2009) and it was suggested that this might improve some of the systematic errors found in coupled models (Murtugudde et al., 2002). The sea surface temperature (SST) response to biology is strongly dependent on dynamical feedbacks involving changes in mixed layer depth (hereafter MLD) and currents. It is found that changes in equatorial and off-equatorial MLD are connected to modifications of meridional ocean transports (Sweeney et al., 2005; Manizza et al., 2008; Loeptien et al., 2009) and zonal current velocities through geostrophic adjustment (Nakamoto et al., 2001; Lengaigne et al., 2007). In addition to

the local effect induced by biology on the Equator, non-local processes may also be important in affecting equatorial SSTs. For instance, the meridional advection of off-equatorial heat anomalies induced by biology is found to be relevant in affecting equatorial temperatures and their seasonal cycle (Sweeney et al., 2005; Lengaigne et al., 2007; Gnanadesikan and Anderson, 2009).

In the dynamically coupled ocean-atmosphere system, we also expect local biological heating anomalies to propagate into the climate system and generate feedbacks onto its components which are not easily predictable from the initial perturbation alone. In an atmospheric model forced by biologically-perturbed sea surface temperatures (Shell et al., 2003) and in coupled model experiments (Wetzel et al., 2006; Lengaigne et al., 2007; Gnanadesikan and Anderson, 2009) ocean biota generates changes in surface winds, in the Walker circulation, and in tropical precipitation patterns. The role of coupled ocean-atmosphere processes is however still not clear. On one hand the atmospheric response to biological heating is found to enhance temperature anomalies through wind stress feedbacks (Anderson et al., 2007; Lengaigne et al., 2007), on the other hand atmospheric feedbacks are found to weaken the biological perturbation through turbulent heat fluxes (Oschlies, 2004; Park et al., 2005). Finally, changes in the tropical ocean-atmosphere mean state may modify El Niño Southern Oscillation variability: hybrid and coupled models have been used to assess the role of ocean biota on tropical variability in response to changes in mean seasonal cycles (Marzeion et al., 2005; Lengaigne et al., 2007), air-sea coupling (Timmermann and Jin, 2002; Anderson et al., 2009), and thermocline depths (Wetzel et al. 2006).

A number of studies have focused on how biology interacts with the temperate and high latitude climate. Forced and coupled models containing interactive marine biogeochemistry were used to analyze biologically induced changes in ocean temperature, stratification, sea ice and ocean circulation (Oschlies, 2004; Wetzel et al., 2006; Manizza et al., 2008; Lengaigne et al., 2009). They find that the seasonal cycle of the MLD is amplified because of increased turbulent heat fluxes and changes in the ocean temperature vertical structure produced by biology. Spring biological heating is found to enhance sea ice melting and to produce freshwater anomalies which slightly impact the large-scale meridional overturning circulation (Lengaigne et al., 2009). Teleconnection processes with tropical latitudes arise in relation to Hadley circulation changes (Shell et al., 2003) which modify cloudiness and solar heat flux patterns at subtropical and middle latitudes (Wetzel et al., 2006). In the Southern Ocean, sea

surface temperatures anomalies induced by biology feed back on the wind stress curl field and thus play an indirect effect on ocean meridional overturning and water mass formation (Gnanadesikan and Anderson, 2009).

The understanding of how the global climate system as a whole responds to the bio-optical perturbation still remains a challenge. Even though the local effect of biological radiative heating has been observationally estimated by means of combined satellite and ocean measurements (e.g. Sathyendranath et al., 1991; Strutton and Chavez, 2004), the estimation of how this local effect may affect global climate is not possible in an observational framework as a "control" condition where biology is absent is not available. Yet the study of bio-optical feedbacks on the global climate is relevant in climate research as they may interact with the response of the Earth System to anthropogenic climate change.

The strategy in this study is thus to use a coupled ocean-atmosphere model containing interactive marine biogeochemistry which is capable of simulating the major interactions and feedbacks among different climate components on a global scale. The use of imposed chlorophyll structures would not be suitable for this study as it would not allow for internally consistent bio-physical feedbacks. A 300-year simulation containing full coupling with biology is compared with a physics-only control experiment with the purpose of analyzing bio-feedbacks on the adjusted state of a coupled climate system.

Scientific questions:

- Which regional responses arise in response to biological radiative heating?

- Which are the oceanic and atmospheric mechanisms driving these responses?

- Do these mechanisms act as positive or negative feedbacks on global temperatures?

This chapter is organized as follows: section 3.2 shows the biologically-induced changes in the ocean-atmosphere mean state. The discussion of dynamical mechanisms giving rise to these changes in the Tropics and Extratropics is deferred to Section 3.3. Section 3.4 briefly describes the impact of biological radiative heating on Tropical and Extratropical interannual variability. Concluding remarks are given in Section 3.5.

3.2 Changes in the ocean and atmosphere mean state

To assess the influence of interactive marine biogeochemistry on global climate, two 300-year simulations performed under constant CO_2 atmospheric levels (described in Section 2.3) are compared. The first is a physics-only control simulation and is named A for "Abiotic"; the second contains full interaction with marine biogeochemistry and is named B for "Biotic". The last 150 years of each simulation are used for the analysis of all variables except heat trend terms which are available only for 100 years of simulation.

In experiment A ocean attenuation depth for visible radiation is held constant to 23 m, whereas in experiment B it varies spatially and temporally as a function of chlorophyll and detrital matter concentrations. In Fig. 3-1a we show B minus A attenuation depths calculated following equations 2-2 and 2-3 over the euphotic depth. A decrease in attenuation depths of 3 to 6 m occurs in correspondence of high chlorophyll structures, indicating an enhanced upper ocean heat trapping. Biological radiative heating the B experiment is computed the difference between total and "pure" seawater radiative heating. Areas of enhanced local biological radiative heating (Fig. 3-1b) occur in boreal and austral subpolar latitudes and in the equatorial Pacific, with annual mean values of 0.4-0.6 °C month^{-1} at the surface. We remark that radiative heating is only one of the components of the upper ocean heat budget alongside advective, diffusive and ocean-atmosphere heat fluxes: these other terms compensate for excess radiative heating in order to maintain the climate system in dynamical equilibrium. Biological radiative heating is the only difference between the two experiments and its effect on oceanic and atmospheric properties will now be described. The discussion of local and remote mechanisms leading to these changes will be deferred to Section 3.3.

The addition of biology to the coupled model overall warms the ocean surface (Fig. 3-2a). In the eastern tropical Pacific and at middle and subpolar latitudes SST in experiment B is ~0.4°C higher than in A, with peaks of more than 1°C in some localized regions of the North Pacific and North Atlantic Oceans. SST differences are instead close to zero or negative in some limited areas at high latitudes and in the tropical Pacific Ocean. Following SST changes, the ocean is in general more stratified in experiment B with respect to A (Fig. 3-2b), especially at middle and subpolar latitudes and in the central equatorial Pacific, where percentual changes in mixed layer depth (hereafter MLD) may reach 20%. Heat content integrated between the surface and

300 m depth (Fig. 3-2c) is higher by ~5×10^8J m^{-2} at subtropical and middle latitudes, whereas it tends to be lower (~3×10^8 J m^{-2}) at tropical latitudes (20°S-20°N) and poleward of 50°S and 50°N. Heat content changes arise from the complex interplay of oceanic and atmospheric mechanisms, as discussed in the next section. B minus A differences in SST, heat content and MLD are statistically significant at 99% on large portions of the global ocean (Fig. 3-3), where statistical significance is determined by means of a Student's t-test.
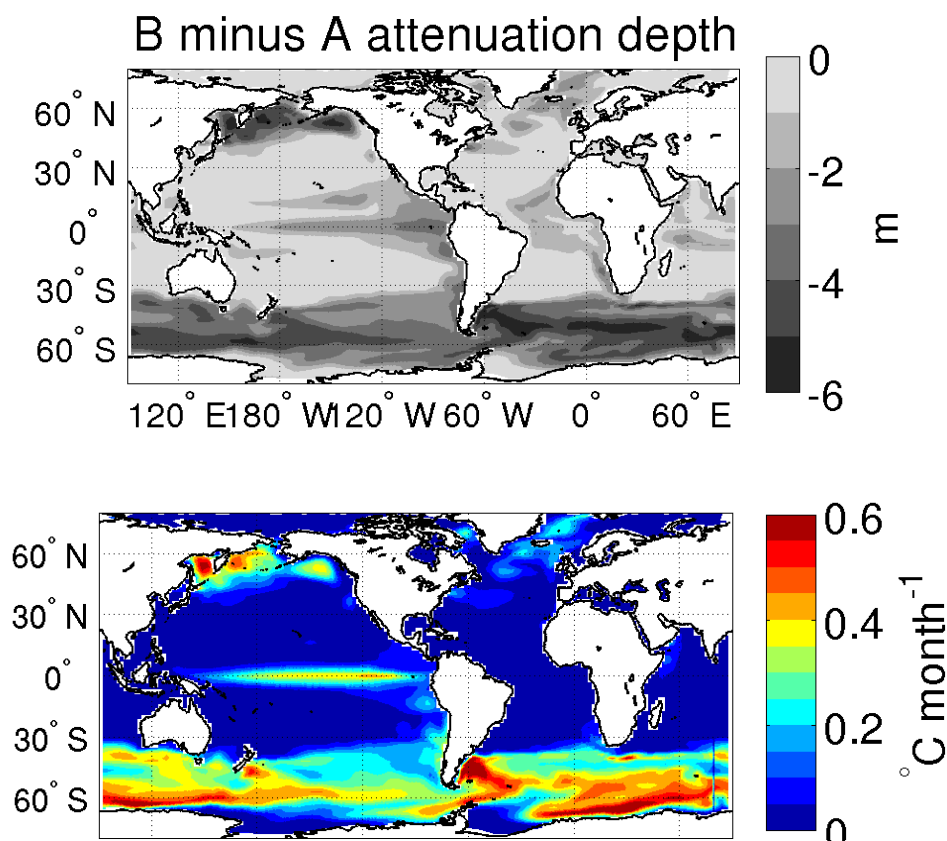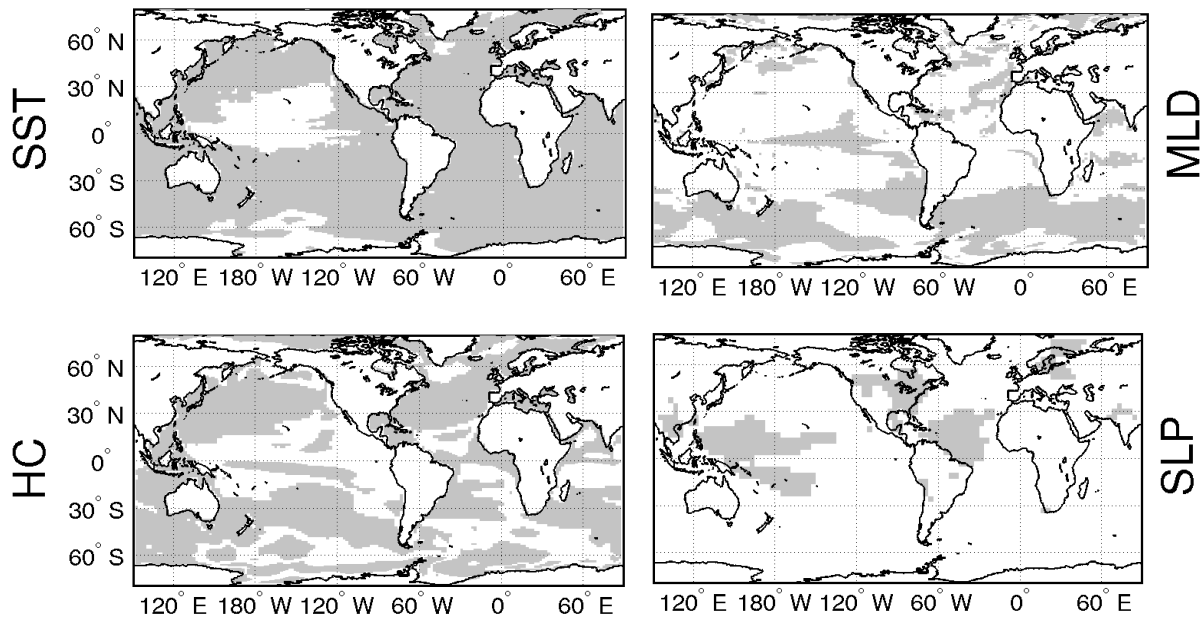

Fig. 3-1: **(top)** B minus A annual mean differences of attenuation depth (m); **(bottom)** B experiment biological heating at the surface (°C month^{-1}).
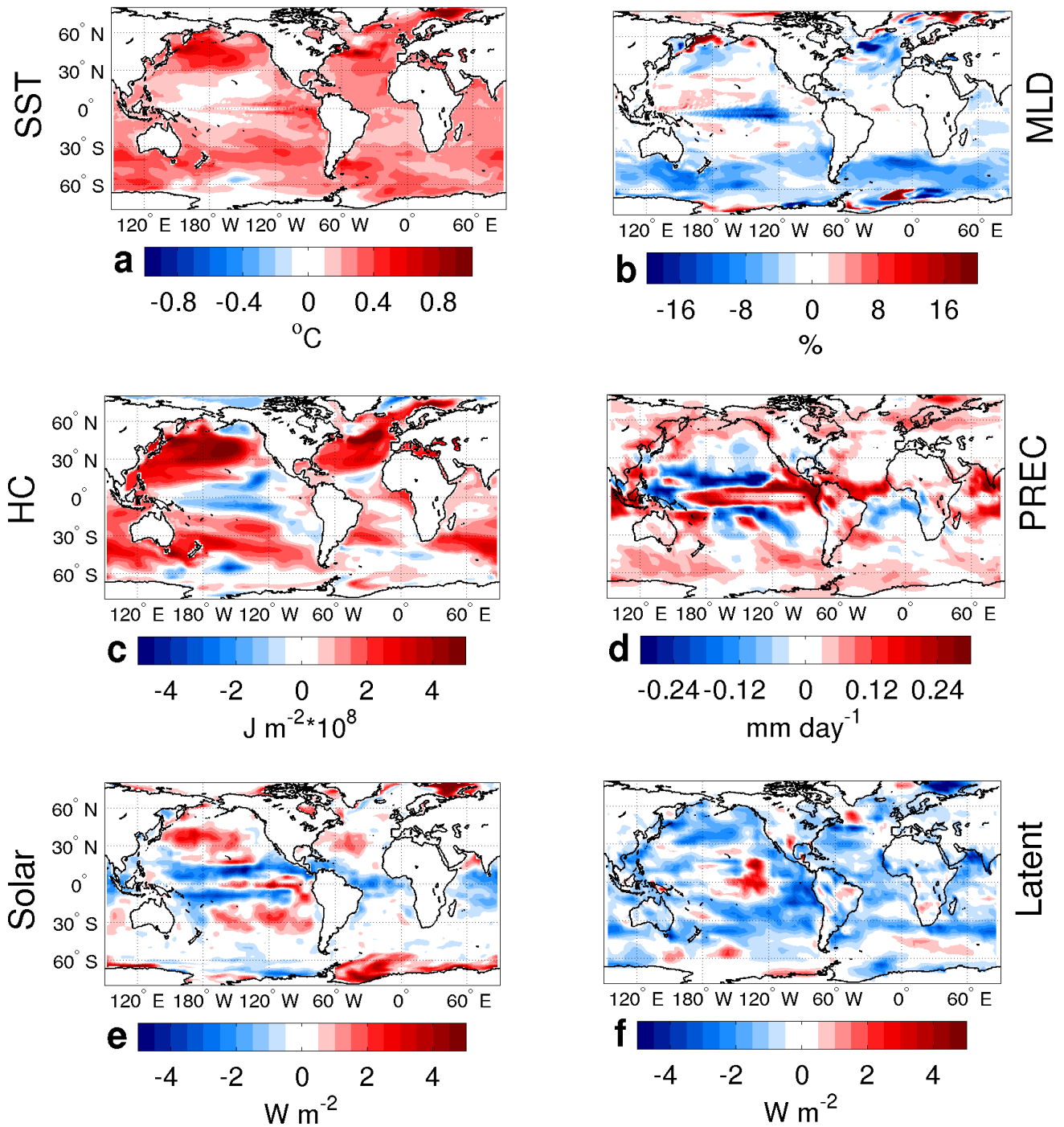
Fig. 3-2: B minus A annual mean differences of **(a)** sea surface temperature (SST) in °C, **(b)** mixed layer depth (MLD), indicated as the percentual change with respect to the A experiment, **(c)** 0-300 m integrated heat content (HC) in J m⁻², **(d)** precipitation (PREC), in mm day⁻¹, **(e)** solar radiation at the ocean surface (W m⁻²) and **(f)** ocean-atmosphere latent heat fluxes (W m⁻²), where positive heat fluxes indicate an ocean heat gain.

Feedbacks on atmospheric variables and on air-sea heat fluxes are also detected. Precipitation (Fig. 3-2d) increases by more than 0.3 mm day⁻¹ between 10°S-10°N in the Pacific, whereas it generally decreases between 15°-30° in both hemispheres. Changes

appear in general to respond to local SST changes and the Intertropical Convergence Zone (ITCZ) is not significantly displaced. Incoming solar radiation at the ocean surface (Fig. 3-2e) is overall lower at tropical latitudes (except on the equatorial Pacific) whereas it is higher at subtropical and middle latitudes. Changes in incoming shortwave radiation in experiment B are connected to the vertical integral of cloud cover (not shown), which is up to 2% higher in the tropical belt (except on the equatorial Pacific) and down to 2% lower at subtropical and middle latitudes. Changes in cloudiness are related to atmospheric circulation changes, as it will be discussed in the next section. Ocean-atmosphere latent heat fluxes (Fig. 3-2f) - defined positive downwards – in general decrease in B, indicating that an ocean with biology looses more heat to the atmosphere through evaporative fluxes. Some limited areas of positive B minus A latent fluxes occur however in the tropical Pacific, in northwestern Atlantic Ocean and in the Southern Ocean. In most areas, solar and non-solar heat flux changes range between ±5 W m^{-2}.

Fig. 3-3 Statistical significance at a 99% confidence interval of B minus A annual mean differences of **(a)** sea surface temperature (SST), **(b)** mixed layer depth (MLD), **(c)** 0-300 m integrated heat content (HC), **(d)** sea level pressure (SLP).

The presence of biology induces anomalies in surface atmospheric circulation through changes in wind velocities (Fig. 3-4, arrows). Wind patterns appear to respond to sea level pressure changes (Fig. 3-5), whose relation with biological heating will be discussed in Section 3.3. Sea level pressure changes are in general statistically not

significant at extratropical latitudes and in the eastern parts of the tropical basins (Fig. 3-3d), where interannual fluctuations exceed changes due to biology. At extratropical latitudes, increased sea level pressure is associated with negative wind stress curl anomalies (Fig. 3-4, colors) in the northern hemisphere (positive in the southern hemisphere), indicating increased anticyclonic vorticity of surface winds. Wind speed changes are around 0.5 m sec^{-1}, i.e. 5-10% with respect to the A experiment. At tropical latitudes wind changes in B with respect to A are especially high in the Pacific Ocean (differences up to 1 m sec^{-1}). Sea level pressure decreases in the eastern Pacific and increases in the central part of the basin, causing westerly wind anomalies to arise east of 130°W. In the central-western Pacific sea level pressure in B is relatively lower on the equator with respect to subtropical latitudes, causing increased wind convergence on the Equator. Easterlies are then weakened in the eastern part of the basin, whereas in the central-western part of the basin they increase their magnitude and their convergence on the Equator.
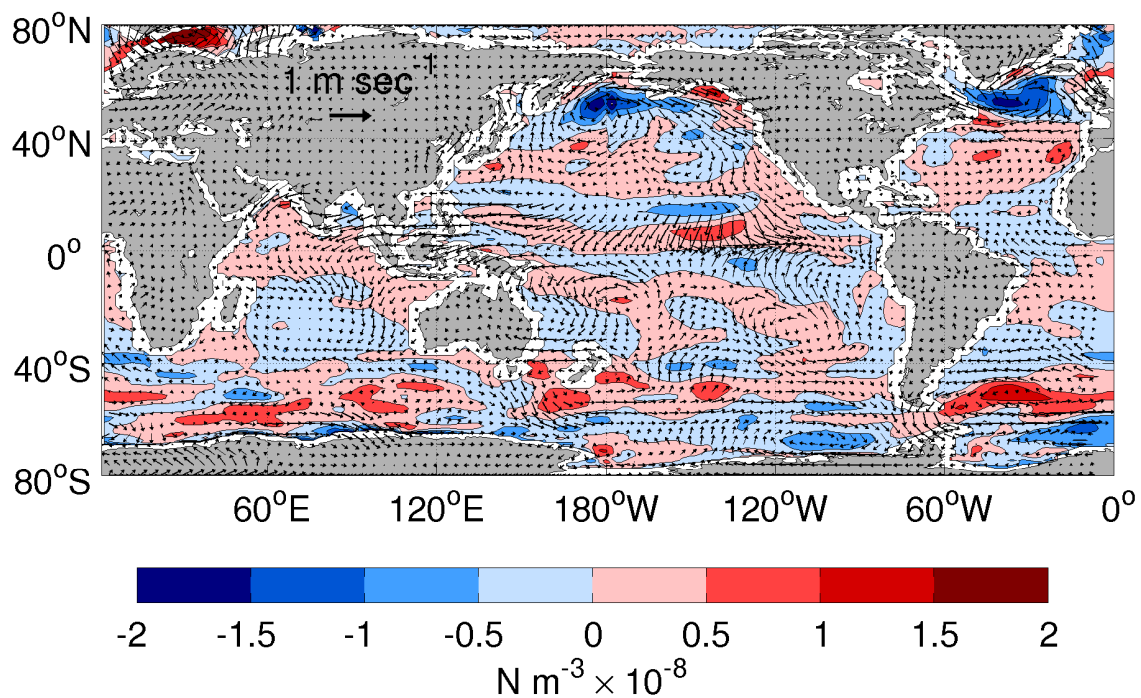
Fig. 3-4: B minus A annual differences of wind velocities in m sec^{-1} at 1000 mbar (arrows) and associated wind stress curl in 1×10^{-8} N m^{-3} (colors).

Changes in wind patterns may in turn affect ocean circulation through changes in wind stress curl (Fig. 3-4, colors). At middle latitudes (between 40°-60°), negative wind stress curl changes of $1\text{-}2\times10^{-8}$ N m^{-3} in the northern hemisphere (positive in the

southern hemisphere) correspond to anomalous downward Ekman velocities of ~1 cm day^{-1}. Poleward of 60°S, wind stress curl differences are mostly negative and their value of ~1×10^{-8} N m^{-3} corresponds to an upward Ekman velocity of ~0.5 cm day^{-1}. In the tropical Pacific wind stress curl differences are positive (negative) equatorward of 10°N (10°S) with values up to 1×10^{-8} N m^{-3}, corresponding to anomalous upward Ekman velocities exceeding 5 cm day^{-1}.
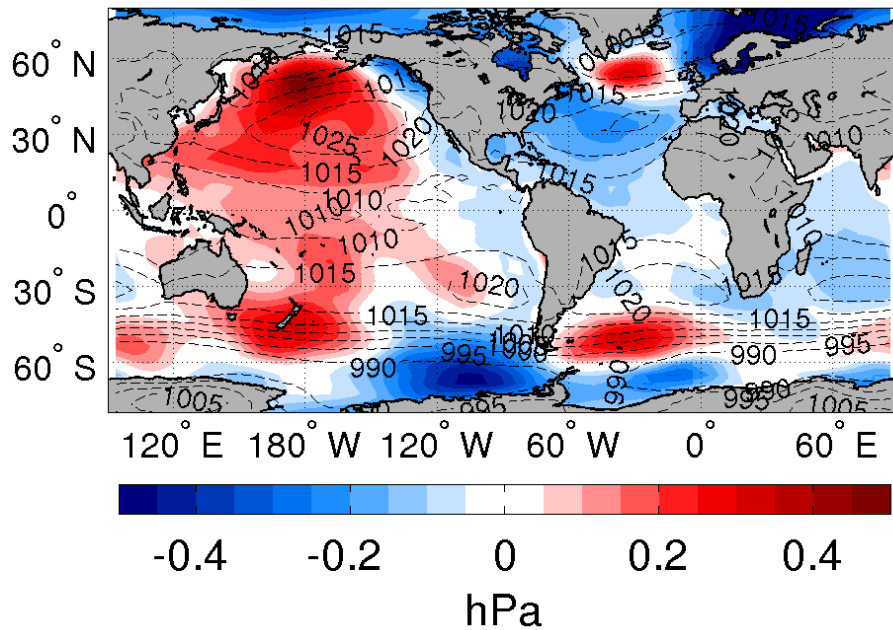
Fig. 3-5: B minus A annual differences of sea level pressure (hPa) and A annual climatology in contours. Shading intervals are 0.05 hPa and contour intervals 5 hPa.

Surface ocean circulation (Fig. 3-6) is modified as a result of thermal and wind anomalies produced by biological radiative heating. Largest changes (red arrows) occur in the central-western tropical Pacific, where the westward South Equatorial Current and the meridional divergence from the Equator are intensified (induced currents > 0.45 cm sec^{-1}). Anticyclonic circulation in the North Atlantic and North Pacific basins is enhanced, with current velocity changes between 0.1-0.45 cm sec^{-1} (blue arrows). In the Southern Ocean equatorward surface anomalies (0.1-0.45 cm sec^{-1}) occur throughout the basin between 40°-60°S.
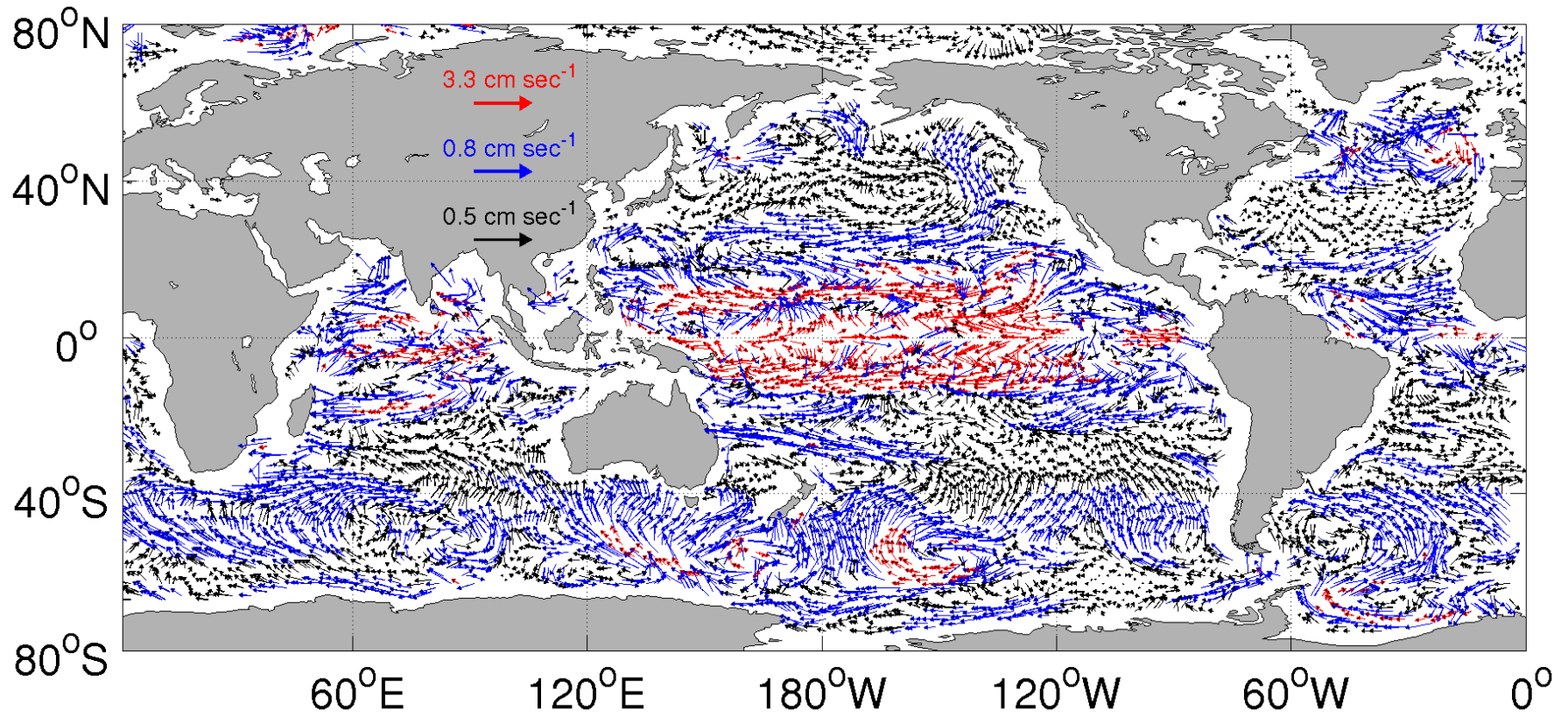
The vertical structure of oceanic and atmospheric response to biological heating will now be addressed. Fig. 3-7 shows meridional sections of B minus A zonally averaged atmospheric and oceanic temperatures and atmospheric water vapor, expressed as
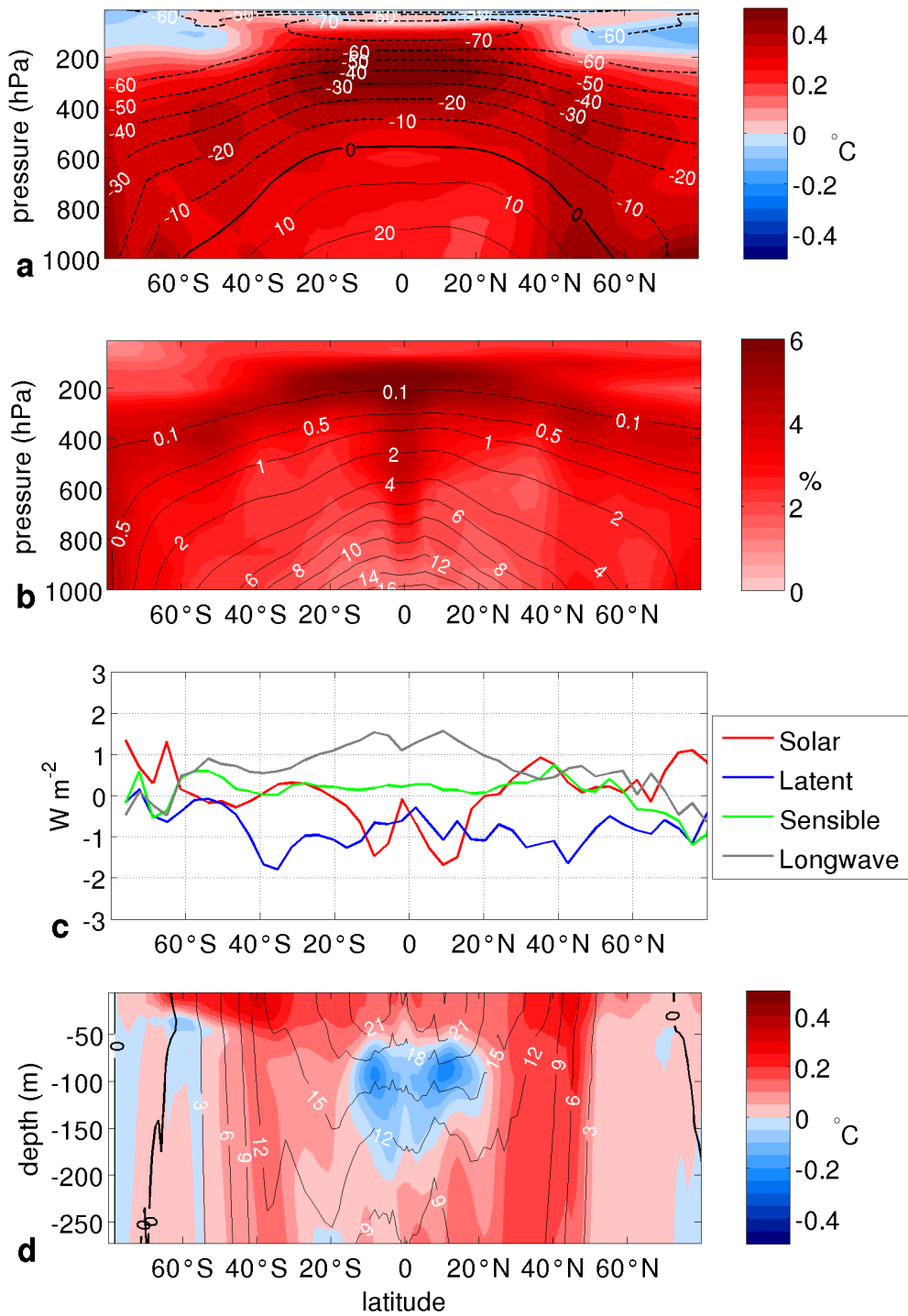
percentual changes with respect to A. Since the response to biology is rather homogeneous along longitude, and more variable along latitude (Fig. 3-2), the zonal average is representative of the investigated signals. Atmospheric temperature differences (Fig. 3-7a) are mostly positive, with values exceeding 0.5°C at tropical latitudes (between 200 and 400 hPa) and at middle latitudes (for pressures > 400 hPa); negative values occur instead at high latitudes for pressures <200 hPa. Zonally averaged ocean temperature differences (Fig. 3-7d) may reach ±0.5 °C in the first 300 m depth, whereas they are minimal below (not shown). At middle latitudes (40°-50° in both hemispheres) positive temperature anomalies occur throughout the first 300 m depth, with highest values in the first 100 m depth (~0.4°C). At tropical latitudes ocean temperature differences are positive (but lower than 0.1°C) until 50 m depth, whereas negative values of -0.2°C are found between 50 and 200 m depth in two circular structures centered on 10°S and 10°N. Water vapor percentual changes in B with respect to A are positive throughout the atmosphere (especially at tropical latitudes) because of the overall enhancement of evaporative fluxes (Fig. 3-2f).

The ocean-atmosphere thermal coupling occurs by means of surface heat fluxes, which contribute to the redistribution of the biological heat perturbation between ocean and atmosphere. Zonally averaged B minus A surface heat fluxes, distinguished in incoming shortwave radiation, outgoing longwave radiation, sensible and latent heat fluxes, are shown in Fig. 3-7c, where positive fluxes indicate an ocean heat gain and negative values an ocean heat loss. Incoming solar radiation in B is lower at tropical latitudes and higher at middle and high latitudes. Longwave radiation differences are mostly positive, except at high latitudes where they are slightly negative. Latent heat flux differences are negative at all latitudes, with higher losses at around 40°N and 40°S. Sensible heat flux differences are smaller with respect to other fluxes and are mostly positive, indicating that in the adjusted state of the simulation the ocean surface is slightly cooler than the overlying atmosphere. On global average the net surface heat flux is close to zero, indicating that the atmosphere and upper-ocean have adjusted to biology reaching a new thermal equilibrium. In this adjusted state, latent heat fluxes are the main contributor to redistributing the biological heat perturbation to the atmosphere, whereas sensible heat fluxes transfer back to the ocean a small part of the exchanged heat. Changes in solar and longwave radiation, also importantly involved in the redistribution of heat between

the ocean and atmosphere compartments, are mainly related to modifications in the atmospheric circulation, as it will be discussed in the following Section.

Fig. 3-6 B minus A annual differences of surface currents (cm sec^{-1}). Note different scaling for velocity differences >0.45 cm sec^{-1} (depicted in red), velocities included between 0.15 and 0.45 cm sec^{-1} (depicted in blue), and lower than 0.15 cm sec^{-1} (depicted in black).

Fig. 3-7 Zonal averages of **(a)** B minus A (colors) and A (contours) atmospheric temperature (°C) plotted as a function of atmospheric pressure, **(b)** B minus A (colors, %) and A (contours, kg/kg×10⁻³) water vapor plotted as function of atmospheric pressure, **(c)** B minus A surface heat fluxes (W m⁻²) distinguished between solar (red), latent (blue), sensible (green), and longwave (grey), where positive values indicate an ocean heat gain, **(d)** B minus A (colors) and A (contours) ocean temperature (°C) plotted until 300 m depth.

3.3 Discussion of mechanisms

In Section 3.2 it was shown that the addition of a biological radiative heating perturbation of ~0.4°C month^{-1} into the coupled climate model significantly affects most components of the climate system, including ocean temperature and circulation, ocean-atmosphere heat fluxes, atmospheric temperatures and water vapor, and atmospheric circulation and associated precipitation and solar radiation patterns. Results have also highlighted a meridional ocean heat content redistribution between tropical latitudes which cool, and subtropical and middle latitudes which warm. These results raise several questions, for instance: (1) which processes compensate for the ~0.4°C month^{-1} biological heating to produce a new equilibrium point in which SST is on average ~0.4°C higher? (2) Why does ocean heat content decrease in the tropical Pacific even though chlorophyll values are high? (3) Through which mechanisms does biology interact with atmospheric circulation at tropical and extratropical latitudes? These and other issues will be analyzed in the following two sections separately for the Tropics and Extratropics as they involve different mechanisms.

3.3.1   Dynamical feedbacks in the Tropics

To investigate tropical responses to ocean biota, we focus on the tropical Pacific where biology and biologically-induced changes on the physics are more pronounced. However many of the discussed arguments also hold for the tropical Atlantic Ocean. In the tropical Pacific, B minus A surface radiative heating differences (Fig. 3-8a) are positive (0.6 °C month^{-1}) on the Equator and negative in the surrounding off-equatorial belts. This modified radiative heating pattern, caused by the sum of biological radiative heating (Fig. 3-1b) and changes in incoming shortwave radiation (Fig. 3-2e), is importantly involved in generating tropical Pacific SST differences.

The feedback of ocean biota on physics is different between eastern and western tropical Pacific. In the eastern tropical Pacific positive SST anomalies generate direct thermally-driven ascending motions in the atmosphere associated with decreased sea level pressure (Fig. 3-5). The resulting weakening of the west-east sea level pressure zonal gradient induces westerly wind anomalies in the eastern Pacific (Fig. 3-4) through Bjerknes feedback. Lower tropospheric easterly winds and upper troposphere westerly winds decrease by ~0.5 m sec^{-1} (Fig. 3-9), indicating an overall weakening of the

eastern branch of the Walker circulation, i.e. the zonal atmospheric cell driven by east-west pressure differences (Bjerknes, 1969).
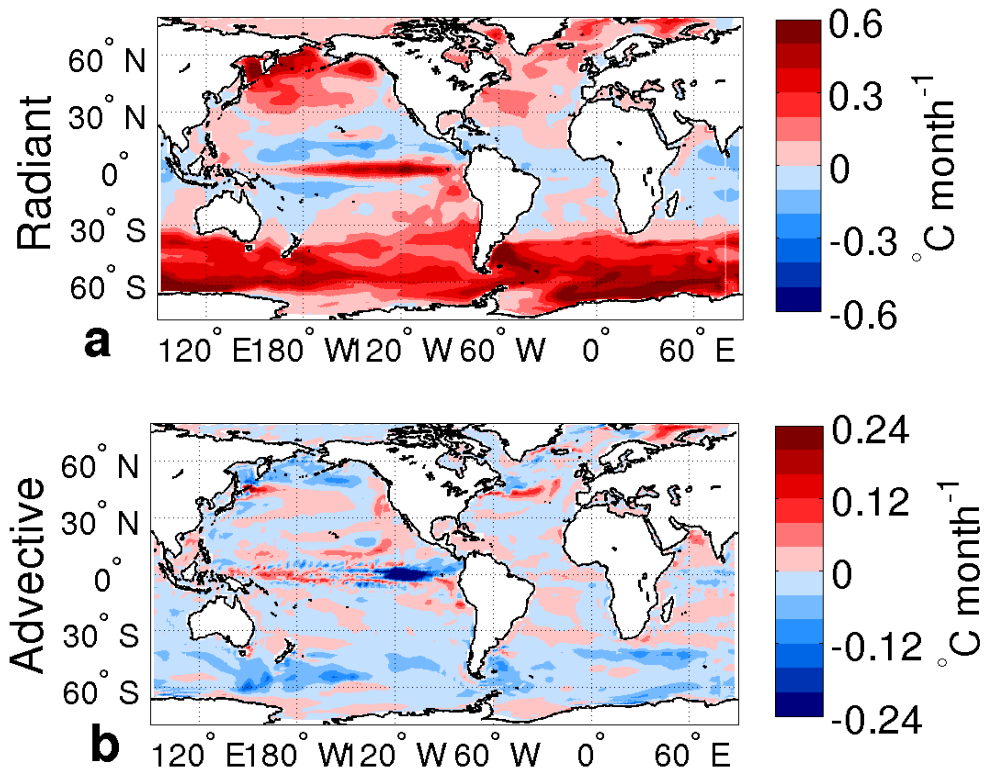
Fig. 3-8: Annual means of B minus A surface heating terms (°C month^{-1}) due to **(a)** radiative processes and **(c)** advective processes (sum of zonal, meridional and vertical components). Note the different color scales.
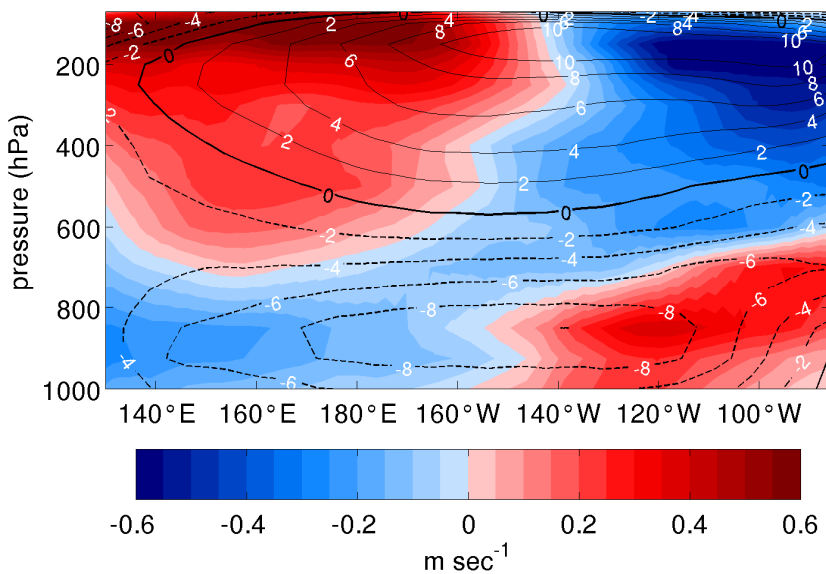
Fig. 3-9 Zonal section in the Equatorial Pacific of atmospheric zonal velocities (m sec^{-1}) averaged between 5°S-5°N and plotted as a function of atmospheric pressure (hPa). Colors: B minus A, contours: A. Positive values correspond to eastward motion.

In the central and western Pacific, large-scale changes in the sea level pressure field (Fig. 3-5) create relatively lower sea level pressures on the equator with respect to subtropical latitudes, causing trade winds to strengthen and to enhance their converge on the Equator. Consistently, in the western Pacific the Walker circulation is enhanced (Fig. 3-9). The Hadley circulation, i.e. the meridional atmospheric cell connecting tropical ascending motion to subtropical descending motion, is also strengthened in response to concentrated heating in the equatorial belt (Hou and Lindzen ,1992), related to the chlorophyll maximum. Wind convergence increases on the equator, anomalous upward atmospheric velocities of ~1 hPa day^{-1} occur over the tropical Pacific (Fig. 3-10a) and poleward wind anomalies between 0.1-0.2 m sec^{-1} are detected in the upper troposphere (Fig. 3-10b). Increased atmospheric upward motion over the Tropics is associated with the advection of heat anomalies in the upper troposphere (Fig. 3-7a) and with enhanced tropical precipitation (Fig. 3-2d), as also found by Wetzel et al., (2006), and cloudiness (not shown). This process, which causes a decrease in incoming shortwave radiation at the ocean surface (Fig. 3-2e), exerts a negative feedback on tropical SSTs. Exception to this pattern is a tight band on the equatorial Pacific, where increased upwelling and advective cooling (which will be discussed further on) have opposite effects on cloudiness and incoming shortwave radiation.

Latent heat fluxes (Fig. 3-2f) are importantly involved in damping biologically-induced SST anomalies and are certainly a major agent limiting SST differences between the two experiments. This important feedback would not be captured by ocean-only models, which are in fact often characterized by more pronounced biologically-induced SST perturbations (e.g. Nakamoto et al., 2001, Murtugudde et al., 2002). In addition, increased evaporative fluxes cause atmospheric humidity (Fig. 3-7b) and cloudiness to increase globally, leading to a decrease in the outgoing longwave radiation (Fig. 3-7c) by means of cloud and water vapor feedbacks (Held and Soden, 2000). This process exerts a positive climatic feedback on SSTs (Forster et al., 2007).
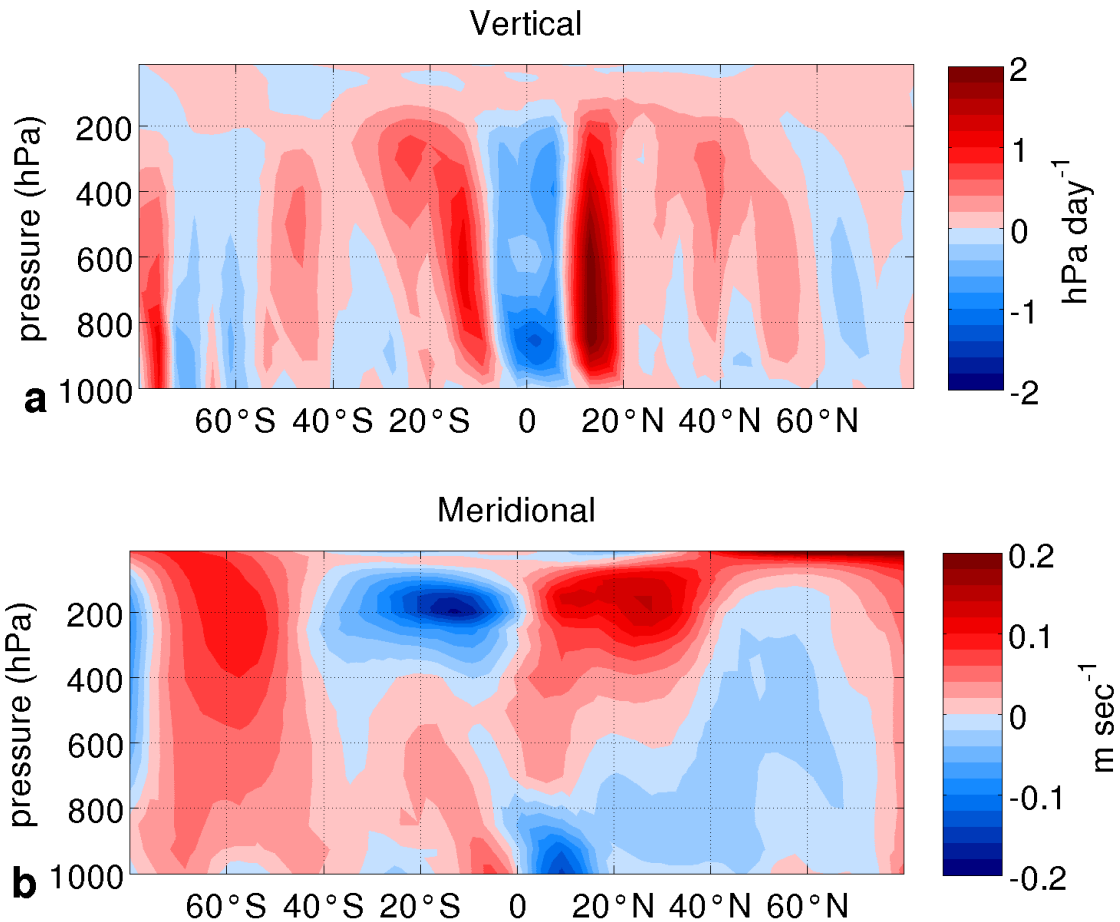
Fig. 3-10: Meridional sections in the central Pacific of B minus A **(a)** vertical atmospheric velocity (hPa day^{-1}) and **(b)** meridional atmospheric velocity (m sec^{-1}). Quantities are zonally averaged between 145°E and 100°W. Positive values indicate downward **(a)** and northward **(b)** motion.

After having analyzed tropical atmospheric feedbacks, the oceanic responses will now be investigated. The changes in the wind patterns in the central equatorial Pacific (Fig. 3-4) play a relevant role in producing circulation anomalies (Fig. 3-6). Increased easterlies accelerate the South Equatorial Current and increase cyclonic wind stress curl anomalies which increase equatorial upwelling (Fig. 3-11a). Geostrophic processes may also be at play in modifying equatorial Pacific circulation. Zonal sections of ocean temperature differences, latitudinally averaged between 2°S-2°N in the tropical Pacific (Fig. 3-12a), show a subsurface cooling of up to 0.5°C close to the thermocline depth (Fig. 3-12a, lines). This is related to radiative cooling induced by chlorophyll structures, (Fig. 3-12b) which cause the water column to absorb more radiation in the upper ocean and to have less radiation in layers underneath. As a result the thermocline shoals by ~10 m in the central-eastern Pacific and increases its east-west gradient. The subsurface

meridional convergence of off-equatorial waters therefore increases (Fig. 3-11b) through geostrophic adjustment. At the Equator, where the Coriolis force vanishes, the increased fluid convergence in part rises to the surface to sustain the enhanced divergence, and in part accelerates eastward inside the Equatorial Undercurrent (Philander, 1990). This is evident from Fig. 3-12c, where zonal velocities in the upper thermocline exhibit an eastward increase (up to 6 cm sec^{-1}) all along the Equator, and a slight westward increase below. This pattern corresponds to a slight upward shift and a ~1 Sv enhancement (not shown) of the Equatorial Undercurrent.
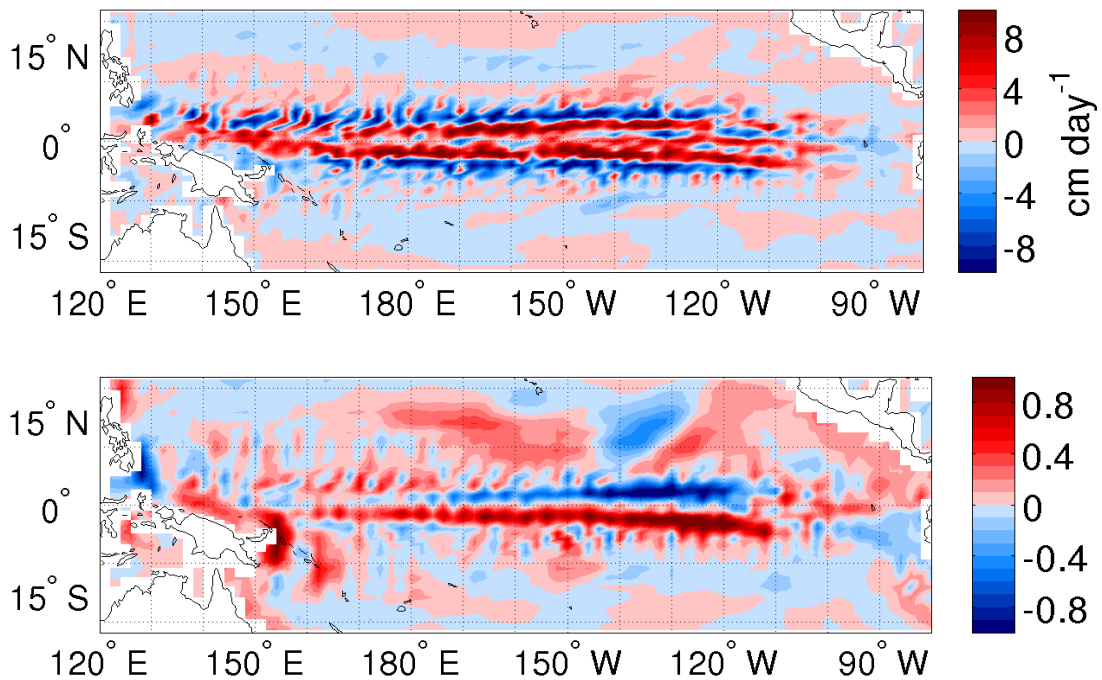
Fig. 3-11: Equatorial Pacific map of B minus A **(a)** ocean vertical velocity (cm day^{-1}) averaged over the first 50 m depth, where positive values indicate upward motion, and **(b)** meridional ocean velocity (cm sec^{-1}) at 50 m depth, where positive values indicate northward motion.

We note that non-local atmospheric feedbacks (which add cyclonic vorticity to the ocean) and local biological processes (which enhance the thermocline east-west tilt) both act to increase shallow meridional overturning and upwelling in the central equatorial Pacific. From Fig. 3-8b it may be seen that surface advection contributes to cooling the ocean surface of the eastern equatorial Pacific by more than 0.2°C month^{-1}, with the dominant term being vertical advection (not shown). Ocean dynamics exerts a negative feedback on equatorial upper ocean temperatures, which therefore do not increase as much as one might expect from biological heating alone.

Shallow tropical mixing (Fig. 2-8a,b) reduces the ventilation of subsurface layers: surface radiative warming then has the possibility of being damped by means of ocean evaporative heat losses, whereas subsurface chlorophyll-induced cold anomalies have less chances of being dissipated. Thus in the Tropics the effect of absorbing solar radiation closer to the sea surface is a net cooling of the water column, as also seen by Oschlies (2004) for the North Atlantic. This mechanism, in association with decreased incoming shortwave radiation and with increased equatorial upwelling, is responsible for the overall 0-300 m heat content decrease in the tropical Pacific (and to a lesser extent in the tropical Atlantic).

Increased precipitation (Fig. 3-2d), stronger upwelling (Fig. 3-11a) and enhanced vertical temperature gradients (Fig. 3-12a) are all processes which concur in enhancing the water column vertical density gradient and thus stratification (Fig. 3-2b). In previous studies using forced ocean configurations, increased equatorial stratification gave rise to (1) enhanced poleward volume transports in the mixed layer (Sweeney et al., 2005; Loeptien et al., 2009) and (2) an increased mixed layer depth meridional gradient which enhances zonal currents through geostrophy (Nakamoto et al., 2001). Also in this study these processes likely act to make equatorial circulation in the central equatorial Pacific stronger.

Considering the increase in upwelling occurring in the central equatorial Pacific, we would expect to see a decrease in SST rather than a slight increase. Evidently, surface biological heating dominates on counteracting dynamical feedbacks in setting the equatorial SST response to biology. Counteracting feedbacks on equatorial SSTs triggered by biology were also found in other coupled model studies. For instance, Lengaigne et al. (2007) find that increased SSTs give rise to decreased easterlies and weaker equatorial upwelling: this positive feedback on equatorial SSTs is however counteracted by meridional advection of biologically-induced negative subsurface anomalies. Anderson et al. (2007) also find that off-equatorial chlorophyll values play a relevant role in supplying cool subsurface waters to the equatorial Pacific: however in their coupled model this advective effect dominates over surface radiative heating, causing SST to decrease. Equatorial Pacific SST changes therefore appear to be very sensitive to atmospheric and oceanic feedbacks triggered by biology, which in turn depend on the model used and on the experimental design. This indicates that in the

tropical Pacific the response to ocean biology might not be entirely robust among coupled models.
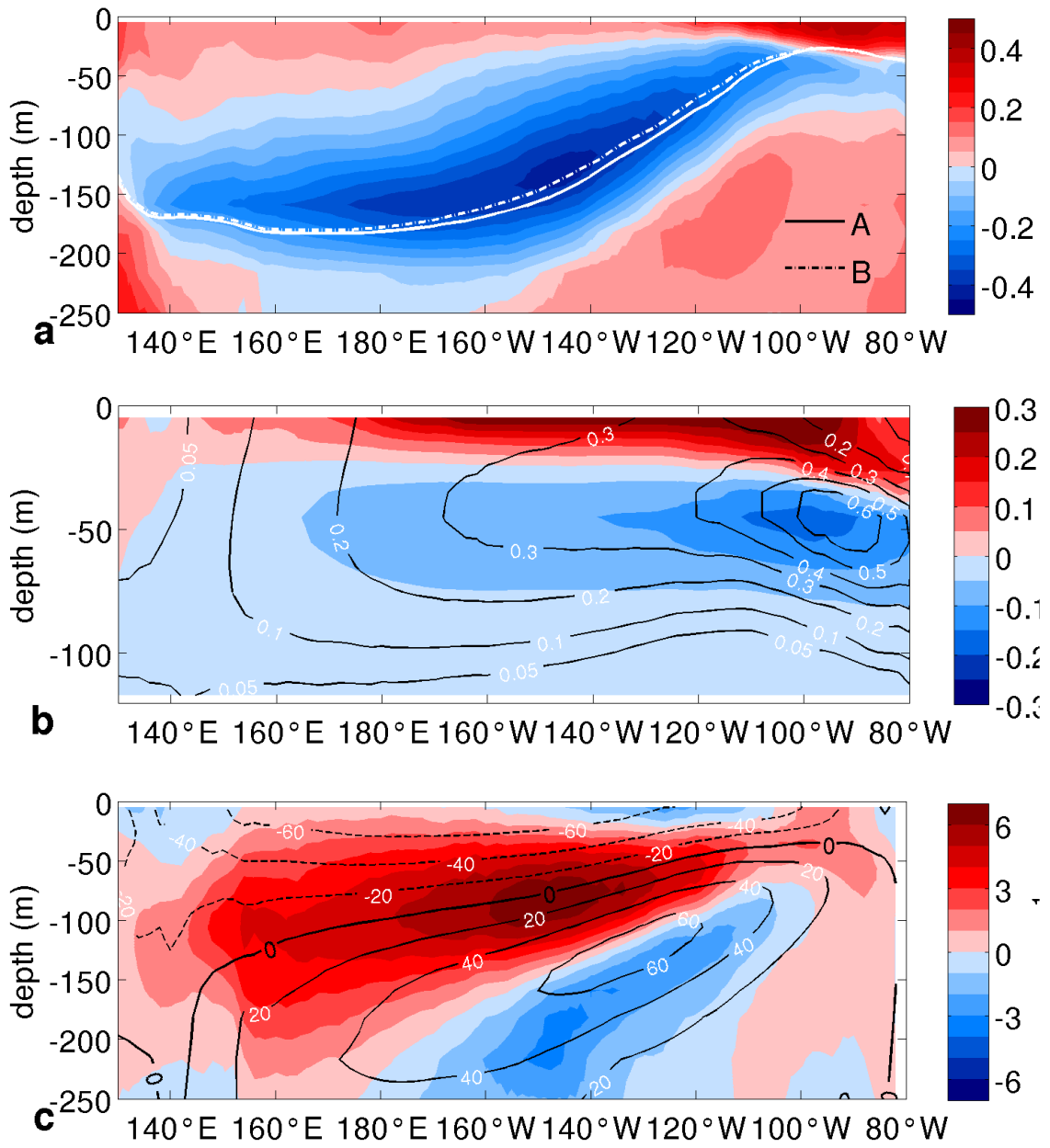
Fig. 3-12 Zonal sections in the equatorial Pacific (2°S-2N average) of **(a)** B minus A ocean temperatures in °C (colors) and thermocline depth (full line: A experiment, dashed line: B experiment), **(b)** B minus A radiative heating differences in °C month^{-1} (colors) and chlorophyll concentration in mg m^{-3} (contours), **(c)** B minus A (colors) and A (contours) zonal current velocities in cm sec^{-1}. Note the different depth scale of panel **(b)**.

3.3.2 Dynamical feedbacks in the Extratropics

Biological radiative heating (Fig. 3-1b) and increased shortwave radiation (Fig. 3-2e) concur in enhancing surface radiative heating at extratropical latitudes (Fig. 3-8a). The increase in radiative heating due to biology generates warm SST anomalies, in agreement with other studies using ocean-only (Oschlies, 2004; Manizza et al., 2005) and coupled model configurations (Wetzel et al., 2006). The biological perturbation is partly dissipated by increased evaporative heat losses to the atmosphere (Fig. 3-2f), which then exert a negative feedback on SST anomalies.

B minus A SST differences have a maximum increase at ~45° and an overall slight decrease poleward of 50° in both hemispheres (Figs. 3-2a and 3-7d). Meridional temperature gradients therefore decrease between subtropical and middle latitudes, and increase between middle and high latitudes. The vertical shear of zonal winds adjusts by means of the thermal wind relation by decreasing between ~20-40° and increasing between ~40°-60° in both hemispheres (Fig. 3-13). When integrated throughout the atmospheric column, these wind shear changes lead to anomalous anticyclonic structures centered at ~50° in both hemispheres. Moreover near the troposphere-stratosphere boundary meridional temperature gradients are also enhanced (Fig. 3-7a) resulting in enhanced westerlies above that level by the thermal wind balance.

Anticyclonic atmospheric circulation corresponds to increased mid-latitude atmospheric descending motion (Fig. 3-10a) and positive sea level pressure differences (Fig. 3-5). The Hadley cell amplification (Fig. 3-10) is responsible for subtropical and middle latitude increases in descending motion, which cause clouds to decrease and incoming shortwave radiation to increase, thus exerting a positive feedback on subtropical and mid-latitude SSTs. This atmospheric teleconnection between tropical and extratropical latitudes, referred to as "atmospheric bridge" (Liu and Alexander, 2007), appears to be effective in transferring the biological perturbation generated in the Tropics to extratropical latitudes. Increased middle latitude SSTs, in connection to intensified Hadley circulation, were also found by Shell et al. (2003) and Wetzel et al. (2006).
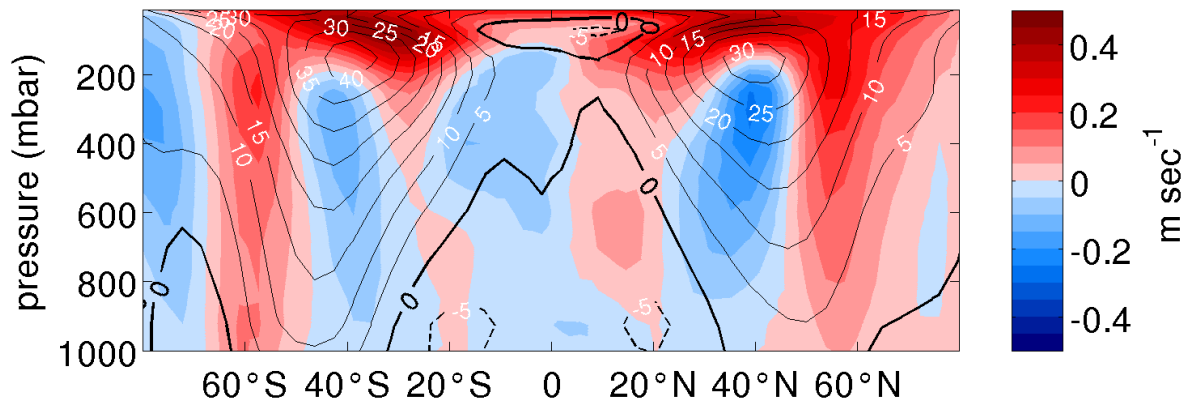
Fig. 3-13 Atmospheric zonal velocities (m sec^{-1}) zonally averaged over the globe. Colors: B minus A differences; contours: A experiment.

In the North Atlantic and North Pacific, anticyclonic wind anomalies (Fig. 3-4) drive anticyclonic ocean circulation anomalies (Fig. 3-14, arrows) which are geostrophically adjusted to sea surface height changes (Fig. 3-14, colors). It has to be remarked that the model does not simulate steric sea surface height changes, which are therefore solely due to changes in ocean divergence. The induced currents resulting from the anomalous circulation are responsible for an increase in the Gulf Stream and North Atlantic Current in the North Atlantic, and of the Kuroshio and North Pacific Current in the North Pacific. Signatures of these circulation changes may be seen in the advective heating structures found between 40°-50°N which reinforce the warm SST anomaly, and in the advective cooling structures between 50°-65°N (Fig. 3-8b) which counteract the warm SST anomaly. In the Southern Ocean, increased westerly winds at ~60°S (Figs. 3-4 and 3-13b) give rise to positive wind stress curl anomalies (Fig. 3-4, colors). Surface ocean currents respond to wind stress curl changes by increasing northward ocean transport between 40-60°S (Fig. 3-6) which causes advective cooling throughout the Southern Ocean (Fig. 3-8b). This process counteracts surface radiative warming due to ocean biology (Fig. 3-8a). Gnanadesikan and Anderson (2009) also find that temperature changes induced by ocean biota in the Southern Ocean are connected to ocean meridional overturning changes through variations in wind stress curl.

Hemispheric asymmetry in the SST response to ocean biota may be seen, with boreal latitudes warming more than austral latitudes despite lower chlorophyll concentrations. This result might be due to the ability of northern hemisphere deep mixed layer depths to store biological radiative heating anomalies in subsurface layers more efficiently than in the southern hemisphere, where instead vigorous current systems tend to cancel the

biological heat perturbation. Moreover the different geometry and latitudinal extents of the Southern Ocean with respect to the North Atlantic and North Pacific basins may also give rise to different dynamical feedbacks.
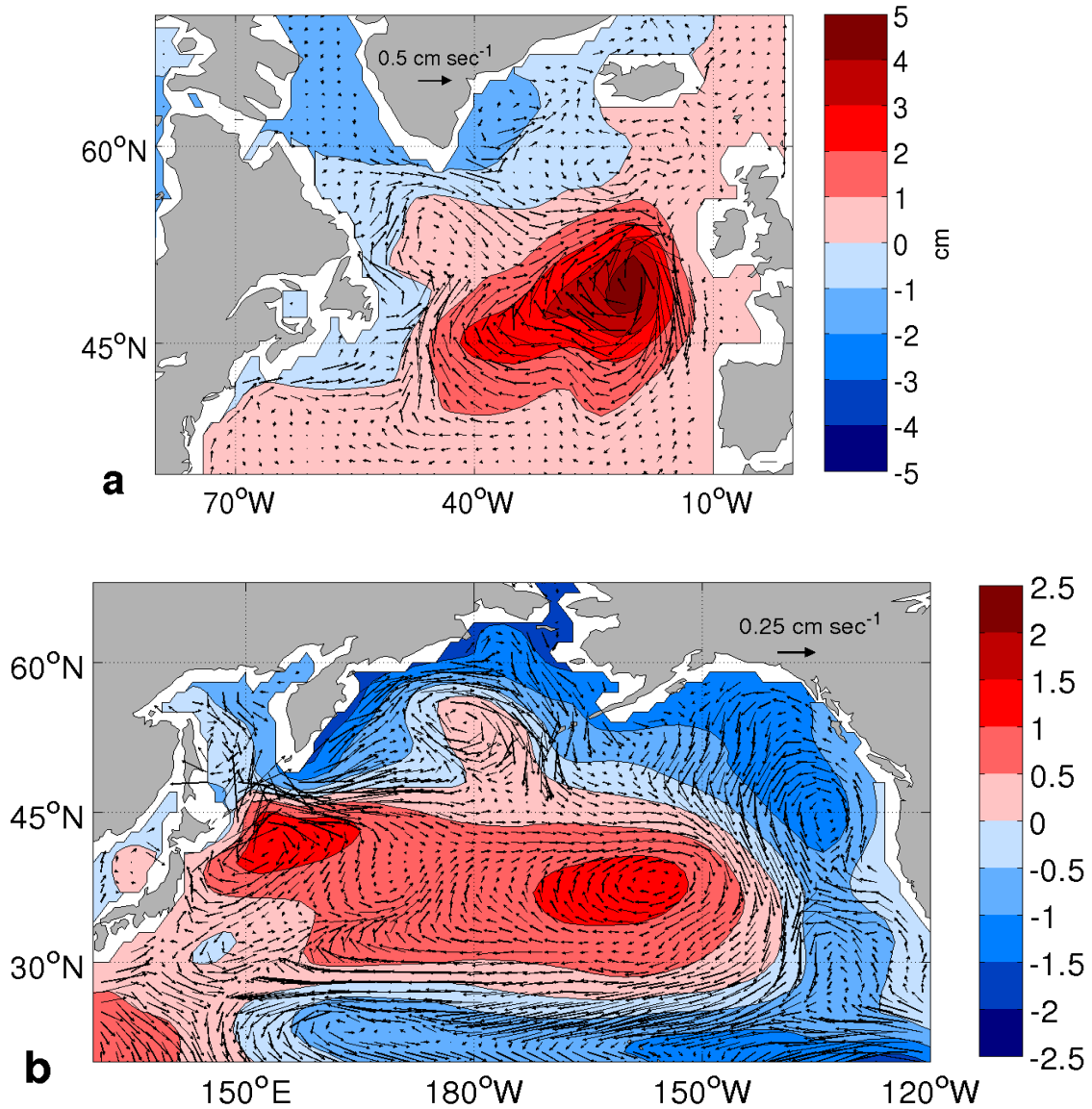
Fig. 3-14 B minus A surface current velocities in cm sec^{-1} (arrows) and sea surface height in cm (colors) in the **(a)** North Atlantic and **(b)** North Pacific. Note the different color and arrow scales between the two panels.

Northern and southern hemispheres however share a common increase in stratification at middle and subpolar latitudes (Fig. 3-2b), related to increased vertical temperature gradients (Fig. 3-7d) which stabilize the water column. The zonally averaged seasonal evolution of MLD in B and its percentual change with respect to A is shown in Fig. 3-

15. Strong seasonal variability is evident, with deepest mixed layers (MLD) occurring in each hemisphere's winter. Between 50-60°N and 60-70°S we find an increase in stratification in summer and a decrease in winter, implying an amplification of the MLD seasonal cycle. This behavior was also detected at subpolar latitudes by Oschlies (2004) and Manizza et al (2008), who give the following interpretation: in summer, when the mixed layer depth is shallower than the light penetration depth, enhanced biological heat trapping leads to increased SST and shallower MLD. However increased SSTs enhance ocean buoyancy losses which accumulate over the annual cycle and eventually result in a deepening of the winter mixed layer. Moreover it is possible that during winter, deep mixing entrains to the surface cold anomalies developed during the preceding months in association with subsurface biological radiative cooling. This destabilizes the upper water column and further increases the MLD. We remark that the seasonal amplification of the MLD is accompanied by a slight delay of the spring stratification onset in both hemispheres.
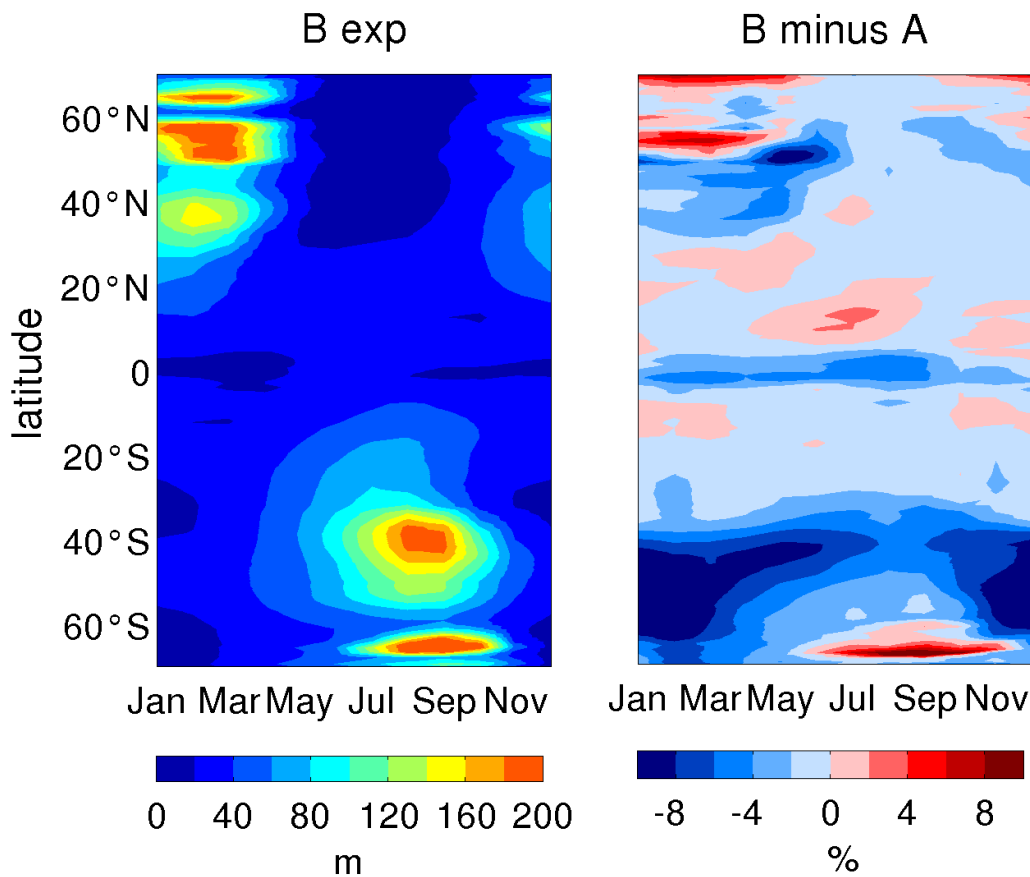
Fig. 3-15: Mean seasonal cycles of zonally averaged **(left)** mixed later depth in the B experiment and **(right)** B minus A mixed later depth.

3.4 Changes in variability

After having analyzed the changes in the physical mean state induced by biological radiative heating, here the feedbacks on ocean-atmosphere variability are briefly addressed. In Fig. 3-16 diagnostics for the eastern tropical Pacific (Niño3 region: 5°S-5°N; 150°W-90°W) are shown. SST in the Niño3 region is slightly higher in the B experiment but the amplitude of its seasonal cycle is not modified (Fig. 3-16a). Time series of SST anomalies in the Niño3 region (Niño3 index) show a tendency in the B experiment towards an increased number of high index phases (positive and negative) at the expenses of lower amplitude events (Fig. 3-16b). Consistently, standard deviation of the Niño3 index increases from 1.0 in the A experiment to 1.2 in the B experiment. Increased standard deviation of the Niño3 index in B cannot be explained by reduced seasonal cycle, as found in previous studies (Marzeion et al., 2005; Lengaigne et al., 2007). It could be however related to shoaling of the thermocline in B which enhances the sensitivity of the upper ocean layer to coupled ocean-atmosphere fluxes. The power density spectrum of the Niño3 index shows a peak between at a 30-40 month period (i.e. 2-3 years) and no significant shift appears to occur between the two experiments.

At extratropical latitudes, leading modes of atmospheric variability are extrapolated by means of Empirical Orthogonal Function (EOF) analysis computed on winter sea level pressure (hereafter SLP) anomalies. The first mode of SLP variability in the North Atlantic sector, the North Atlantic Oscillation (NAO, Hurrell et al., 2003), and the second mode of winter SLP variability in the North Pacific sector, the North Pacific Oscillation (NPO, Rogers, 1981) both involve meridional redistributions of atmospheric mass between subtropical and subpolar latitudes. The variance explained by the NAO increases from 53% in A to 60% in B, and the variance explained by the NPO increases from 22% in A to 27% in B. The first mode of SLP variability in the North Pacific sector, involving fluctuations of the Aleutian Low strength with coherent SLP changes over the whole North Pacific, decreases from 52% in A to 44% in B. An interpretation to these results could be the bio-optical feedbacks, because of their ability of modifying meridional temperature and SLP gradients (Figs. 3-2a, 3-6, 3-7a), are effective in enhancing the variance of those modes involving fluctuations of subtropical-subpolar SLP differences, i.e. the NAO and the NPO. However it has to be noted that the variance explained by the described modes of variability is biased towards

overestimated values (as found also in other coupled models, e.g. Miller et al., 2006). Therefore these interpretations have to be taken with care.
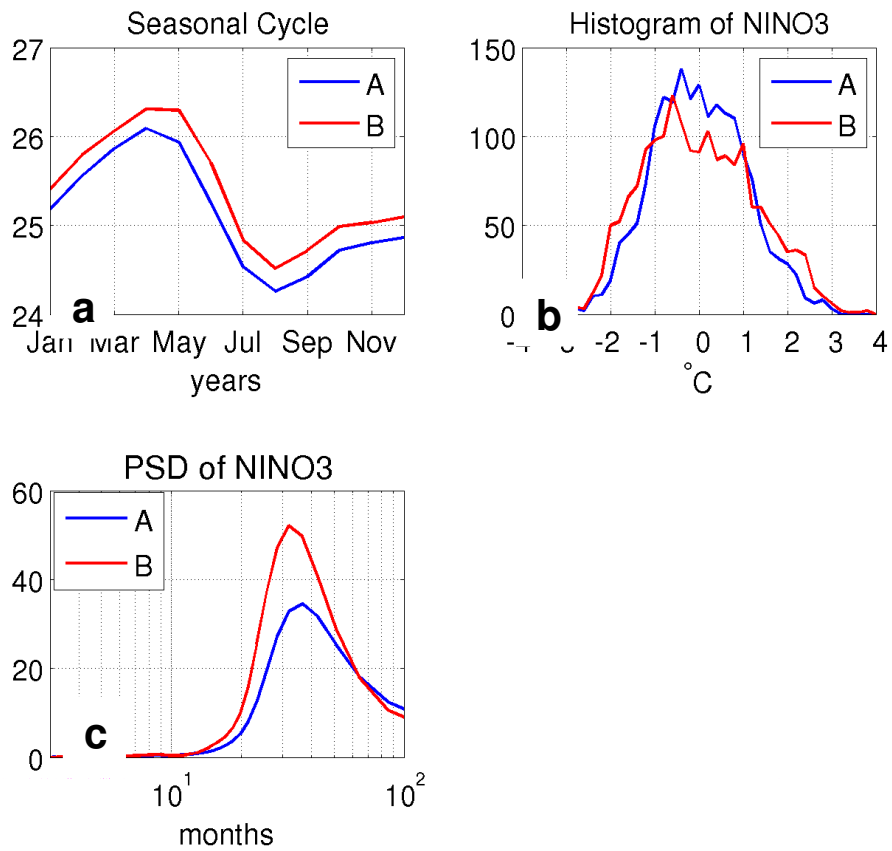
Fig 3.16: Niño3 region (5°S-5°N; 150°W-90°W) SST diagnostics for experiments A (blue lines) and B (red lines): **(a)** SST seasonal cycle, **(b)** histogram of Niño3 index, **(c)** power density spectrum of Niño3 index.

3.5 Conclusions

Global bio-optical feedbacks arising from the absorption of solar radiation by ocean phytoplankton were investigated in a state-of-the-art fully coupled model containing interactive marine biogeochemistry. This modeling framework allowed bio-optical feedbacks to be fully represented at the global scale and to be at all times internally consistent marine biogeochemical structures. A 300-year experiment was performed with the full version of the coupled model and compared with a control simulation characterized by a constant attenuation depth for visible radiation over the entire ocean domain. It is found that in the dynamically coupled climate system the heating perturbation induced by biology propagates within the climate system and generates feedbacks around 5-10% on virtually all its components. Biological radiative heating raises sea surface temperature (SST) of about 0.5°-1°C, and triggers various intrinsically coupled mechanisms within the climate system:

1. Increased ocean latent heat losses raise atmospheric temperatures and water vapor. <u>Implication:</u> Increased atmospheric water vapor exerts a positive feedback onto global temperatures because of its capability of absorbing longwave radiation. This may suggest that marine biogeochemistry contributes to some extent to the Earth's greenhouse gas effect.

2. The equatorial Pacific maximum in biological heating causes an intensification of the Hadley circulation which acts as a teleconnection mechanism affecting cloudiness and solar radiation patterns from tropical to subtropical latitudes. <u>Implication:</u> Changes in solar radiation exert a negative feedback on SST at tropical latitudes, and a positive feedback at Extratropical latitudes.

3. Changes in SST meridional gradients at extratropical latitudes modify the vertical shear of zonal winds and give rise to anticyclonic anomalies in the mid-latitude atmospheric circulation, thus modifying ocean circulation. Related ocean heat transport modifications locally affect SSTs.

4. Increased wind convergence onto the Equator induces cyclonic wind stress curl anomalies which drive near-surface upwelling. <u>Implication:</u> increased upwelling exerts a negative feedback onto equatorial SSTs.

5. At subpolar latitudes, biological radiative heating interacts with seasonal mixing and heat fluxes by generating an amplification of the mixed layer depth seasonal cycle.

The response of the climate system to biological heating by phytoplanktonic organisms resembles in many ways that to anthropogenic carbon emissions as simulated in climate projections for the XXI century (Meehl et al., 2007), even though with lower magnitudes. Increased atmospheric water vapor, upper-tropospheric heating localized over the Tropics, cooling at the troposphere-stratosphere boundary north of ~45°N and associated mid-latitude westerly jet response, decreased sea ice, decreased heat content in some tropical areas, and increased (decreased) precipitation over the Tropics (Subtropics) are all processes in common between the two climate perturbations. A hypothesis that can be made to interpret these results is that phytoplankton contributes to a small extent to the greenhouse gas effect. Interestingly, even though the two climate perturbations (anthropogenic and bio-optical) are located one in the atmosphere and the other in the ocean, the climate system adjusts as a whole to the perturbations and the origin of the initial perturbation cannot be any longer distinguished.

Chapter 4

# Bio-physical ocean responses to the North Atlantic Oscillation in a coupled model

Summary This study aims at analyzing the response of the ocean physical and biogeochemical properties to the North Atlantic Oscillation (NAO), the primary mode of climate variability in the North Atlantic sector. While physical responses to the NAO are rather well documented, the study of marine biogeochemical responses is made difficult by the shortness of available time series or limited spatial coverage. Here a coupled ocean-atmosphere model containing a complex marine biogeochemistry model is used to perform a 300-year global simulation under constant CO_2 concentrations in which NAO variability is internally generated. It is found that NAO variability affects ocean properties through changes in momentum, heat and freshwater fluxes which drive coherent anomaly patterns in sea surface temperature, ocean mixing and circulation. Nutrients, chlorophyll and zooplankton concentrations are tightly related to NAO interannual variability mainly through changes in mixed layer depth. In particular, increased mixing in the subpolar gyre during positive NAO phases decreases phytoplankton biomass in winter and increases it in the following spring bloom because of higher nutrient availability. The modification of the lower trophic levels of the ecosystem affect in turn particulate organic matter production and air-sea CO_2 fluxes, with potentially relevant feedbacks on climate. By analyzing the lagged response to the NAO it is found that ocean temperature and salinity anomalies persist and propagate in successive years after their generation by NAO forcing. On the other hand marine biogeochemistry has limited memory of NAO forcing as its variability is mainly governed by interannual fluctuations of vertical mixing. The interannual and low-frequency bio-physical ocean responses to the NAO differ. During persistent positive NAO phases, changes in ocean circulation, i.e. an intensification of the subpolar gyre and an "inter gyre-gyre" anticyclonic circulation anomaly at mid-latitudes, modify the temperature and salinity fields, with impacts on stratification and on marine biogeochemistry.

4.1 Introduction

Multiyear time series at fixed points and ship-based measurements of upper North Atlantic Ocean biogeochemical and ecological properties show interannual-to-decadal fluctuations (Barton et al., 2003; Bates, 2007) which are suggested to be largely influenced by large-scale patterns of meteorological variability. The primary mode of climatic variability in the North Atlantic sector from interannual to decadal time scales is the North Atlantic Oscillation (Bjerknes, 1964) which refers to a redistribution of atmospheric mass between Arctic and subtropical Atlantic. The North Atlantic Oscillation (NAO) is characterized at the surface by a north-south dipole of simultaneous out-of-phase sea level pressure anomalies (Walker and Bliss, 1932); it is thus a measure of the strength and position of maximum surface westerly winds across the Atlantic. The temporal evolution of the NAO is described by the NAO index, calculated as the normalized time series of sea level pressure differences between Portugal and Iceland (Hurrell, 1995). Positive index phases (NAO+) correspond to increased pressure gradients and thus to stronger-than-average westerly winds; negative index phases (NAO-) correspond to reduced pressure gradients and thus to a weaker and more zonally-oriented storm track (Fig. 4-1).

Large scale meteorological fluctuations associated with the NAO drive coherent patterns of spatial and temporal variability of North Atlantic Ocean properties. On interannual time scales, North Atlantic Ocean sea surface temperatures and circulation vary primarily in response to changes in the surface winds, air-sea heat exchanges, and freshwater fluxes associated with changes in surface wind fields (Bjerknes, 1964). A NAO+ phase shows positive sea surface temperature anomalies in the subtropics and in the marginal seas of northern Europe, and negative anomalies at subpolar and tropical latitudes (Visbeck et al., 2003). On longer time scales the additional contribution of ocean dynamics is suggested to be playing an active role in determining the temporal and spatial evolution of surface and subsurface temperature anomalies (Kushnir, 1994; Eden and Jung, 2001). The ocean, owing to its elevated heat capacity, is capable of integrating atmospheric forcing and of giving rise to delayed effects in the ocean circulation. For instance, observational evidence suggests delayed responses to NAO wind forcing of the Gulf Stream – North Atlantic Current system and of the subpolar gyre strength (Curry and McCartney, 2001; Frankignoul et al., 2001; Flatau et al., 2003; Haekkinen and Rhines, 2004) which in modeling studies have been suggested to

produce reverberations on the meridional overturning circulation (Eden and Willebrand, 2001; Boening et al., 2006; Bellucci et al., 2008; Deshayes and Frankignoul, 2008). The excitation of baroclinic Rossby waves in response to perturbations of the meridional overturning circulation is also suggested to be a relevant mechanism on decadal time scales in determining the adjustment of mid-latitude gyres to changing surface forcing (Frankignoul et al., 1997).
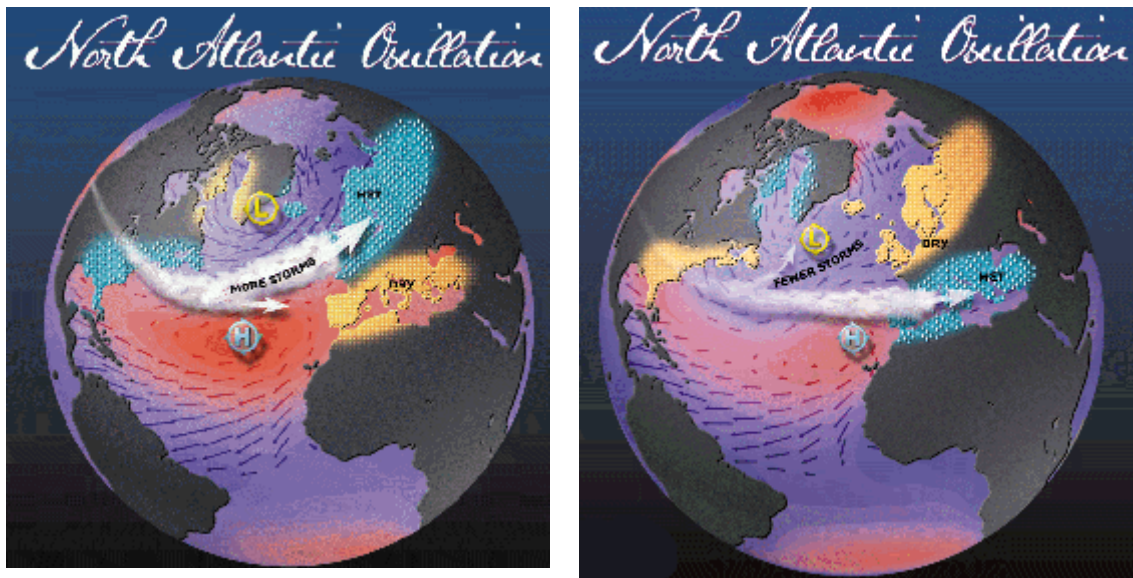
Fig. 4-1 Schematic illustration of the path and strength of winter storms around high (H) and low (L) pressure zones in the North Atlantic corresponding to positive (left) and negative (right) NAO phases. From http://www.ldeo.columbia.edu/res/pi/NAO/

Regional patterns of NAO variability are capable of affecting ocean ecosystems through their local effects on upper-ocean mixing, solar radiation and ocean temperature (Drinkwater et al., 2003). In particular during a NAO+ phase, strengthened and poleward-shifted westerlies lead to surface cooling and deeper mixing at subpolar and tropical latitudes, and enhanced temperatures and stratification at middle latitudes (Cayan, 1992). Observational evidence of the influence of meteorological variability on marine biogeochemistry and phytoplankton ecology has been obtained in past studies from time series at fixed points, such as the subtropical Bermuda Atlantic Time Series (BATS) station (Follows and Dutkiewicz, 2002; Gruber et al., 2002; Bates, 2007) and the subpolar Ocean Weather Station "India" (Follows and Dutkiewicz, 2002), from Continuous Plankton Recorder (CPR) measurements of phytoplankton relative abundance (Barton et al., 2003; Leterme et al., 2005), and from satellite chlorophyll estimates (Follows and Dutkiewicz, 2002; Siegel et al., 2002; Henson et al., 2006; 2009).

The response of phytoplankton variability to changes in mixing is hypothesized by Dutkiewicz et al. (2001) to be regionally dependent on the ratio between the Sverdrup critical depth, defining the compensation level between phytoplankton growth and loss rates (Sverdrup, 1953), and the local mixed layer depth. In fact when the mixed layer depth exceeds Sverdrup's critical layer (around 30-60 m according to Follows and Dutkiewicz, 2002), there is insufficient light to drive net production and a phytoplankton bloom will not occur. Follows and Dutkiewicz (2002) show that the ratio between Sverdrup's critical depth and the local mixed layer depth exhibits a poleward decrease over the North Atlantic basin, indicative of an increased light vs. nutrient limitation from subtropical to subpolar latitudes.

At subtropical latitudes increased winter mixing, occurring during NAO- phases, leads to a stronger bloom in response to enhanced nutrient supply (Follows and Dutkiewicz, 2002). At subpolar latitudes the phytoplankton response to NAO wind fluctuations appears more complex. Barton et al. (2003) analyze CPR measurements during 1948-2000 and detect, in association with NAO+ phases, a positive trend of phytoplankton abundance in the transition zone (45°-55°N) between subtropical and subpolar latitudes, and negative trends to the north and to the south. They hypothesize that deeper mixing would lead to enhanced nutrient entrainment and chlorophyll in the transition zone, but to decreased primary productivity at subarctic latitudes because of Sverdrup's light limitation theory. Conversely, in two ~3-year observational data sets Follows and Dutkiewicz (2002) find no discernible interannual signal in chlorophyll variability at subpolar latitudes - in contrast to subtropical latitudes - whereas spatial variability is much larger. Henson et al., (2006) investigate chlorophyll satellite products in the Irminger Basin and find that winter pre-conditioning is critical in determining the timing of the phytoplankton spring bloom and its magnitude, which is inversely correlated with the frequency of winter storms.

The North Atlantic Ocean is the largest ocean sink for atmospheric CO_2 in the Northern Hemisphere (Gruber et al., 2009). Changes in the ocean state associated with the NAO may also affect the capacity of the North Atlantic Ocean to absorb CO_2 from the atmosphere, as documented by Gruber et al., (2002) and Bates (2007) for the subtropical Bermuda Atlantic Time Series station, Olsen et al., (2003) for the northern North Atlantic, and Santana-Casiano et al. (2007) for the eastern Atlantic ESTOC station. Positive NAO phases are found to be associated by an increased ocean capacity of

absorbing atmospheric CO_2, as also suggested by Thomas et al. (2008) in their modeling study for the period 1979–2004.

A better knowledge of the mechanisms underlying marine biogeochemistry responses to meteorological fluctuations is relevant in Earth system science. In fact, understanding the biogeochemical responses to changes in physical climate on interannual time scales may provide insight into potential responses to long-term human-induced climate trends. Moreover, quantifying the magnitude of natural fluctuations may help to distinguish them from human-induced trends in present-day observed time series; for instance, the effects on marine biogeochemistry of the persistently positive NAO phases in the last decades (Hurrell et al., 2003) could possibly be exchanged with impacts of anthropogenic climate change. Finally, if it is true human-induced climate change may force ocean variability towards a preferential state (Gillett et al., 2003), we can expect a corresponding response also in marine biogeochemical structures.

Yet, whereas ocean physical NAO responses are rather well documented in observational data sets, the analysis of biogeochemical NAO responses is made difficult by reduced spatial and temporal coverage of available observational data sets. Ocean general circulation models containing interactive marine biogeochemistry and forced by specified or observed surface heat fluxes have thus been used to investigate the biogeochemical ocean responses to the NAO (Oschlies, 2001; Henson et al., 2009). However an analysis of this interaction within a fully coupled climate framework, capable of internally generating NAO-like variability and of capturing the major features of atmosphere-ocean-marine biogeochemistry coupling, is still lacking.

In the present study, a climate coupled model containing interactive marine biogeochemistry, is used to produce a 300-year simulation under constant present-day atmospheric CO_2 concentrations. The objective of this study is to quantify basin-scale responses of marine biogeochemistry to NAO variability from interannual to decadal time scales and to identify driving mechanisms within a fully coupled climate framework. With respect to previous studies the approach chosen in this work presents several advantages: (1) a multi-centennial time series provides more robust statistics and allows a separate investigation between interannual and decadal variability; (2) the coupled model allows for a dynamically consistent framework where feedbacks from the ocean to the atmosphere (including those induced by biology) are simulated; (3) constant CO_2 atmospheric levels prevent interference of human-induced climate change

onto the investigated natural signal. The outcomes of this study may help to interpret observations obtained on smaller spatial and temporal domains and may give insight into basin-scale changes in upper ocean carbon fluxes with the atmosphere and deeper ocean.

Scientific questions:

1. Which are the physical mechanisms driving changes in spatial structure, magnitude and seasonality of biogeochemical properties in response to the NAO?

2. Which are the lagged and low-frequency physical ocean response to the NAO and which is their impact on marine biogeochemistry?

This chapter is organized as follows: in section 4.2 the North Atlantic atmospheric variability simulated by the coupled model will be presented. Section 4.3 investigates the physical and biogeochemical ocean responses to NAO interannual fluctuations in terms of spatial structures and seasonal evolution. Section 4.4 shows the lagged response to NAO forcing whereas Section 4.5 analyses the in-phase and in-quadrature responses to low-frequency NAO forcing. Section 4.6 discusses gives concluding remarks.

4.2 North Atlantic atmospheric variability

North Atlantic variability is investigated by means of Empirical Orthogonal Function (EOF) analysis calculated on December-March (DJFM) sea level pressure (hereafter SLP) anomalies in the North Atlantic sector (20°-70°N, 90°W-40°E). The NAO spatial pattern is identified as the leading eigenvector of the cross-covariance matrix and the NAO index as the standardized leading principal component time series. NAO variability explains 60% of SLP variance vs. 37% found in observations (Hurrell et al., 2003), a bias common to other coupled models which tend to overestimate the percentage of variance explained by the Northern Annular Mode (Miller et al., 2006). The NAO index (Fig. 4-2a, bars) exhibits strong variability on interannual time scales and its decorrelation time scale is of 1 year, i.e. comparatively lower than the 3 years of the observed NAO index (Hurrell et al. 2003). Even though decadal cycles are detected in a 9-year running average (Fig. 4-2a, black line), the model tends to overestimate the

energy at interannual time scales at the expenses of decadal and multi-decadal time scales. This bias is common to other coupled models (Gillett et al., 2005) possibly caused by misrepresentations of stratosphere-troposphere coupling processes (Scaife et al., 2005).

The NAO spatial pattern expressed in amplitude of hPa is obtained by regressing wintertime SLP anomalies on the NAO index (Fig. 4-2b, colors). During positive NAO phases (hereafter NAO+) anomalously high surface pressures south of 55°N are associated with anomalously low pressures throughout the Arctic. NAO+ phases act to enhance meridional pressure gradients and to displace towards north the climatological centers of maximum SLP (Fig. 4-2b, contours), thereby affecting wind direction, speed and maxima location. From Fig. 4-2c it may be seen that during NAO+ phases, westerlies are enhanced north of 45°N and weakened between 30°-45°N. Wintertime wind stress curl (Fig. 4-2d) responds to the northward shift of westerly winds by giving rise to an anticyclonic wind anomaly between 35°-55°N and a cyclonic anomaly to the south. We can then expect an enhanced anticyclonic wind driven circulation located between the subtropical and subpolar gyres (the "inter-gyre gyre", Marshall et al., 2001). During NAO+ phases the zero-wind-stress-curl line, which affects storm track pathways and the location of the Gulf Stream and of North Atlantic Current, increases its southwest to northeast tilt over the North Atlantic. The described patterns compare well with observations both in terms of amplitude and of spatial structure (Marshall et al., 2001; Hurrell et al., 2003; Visbeck et al., 2003).
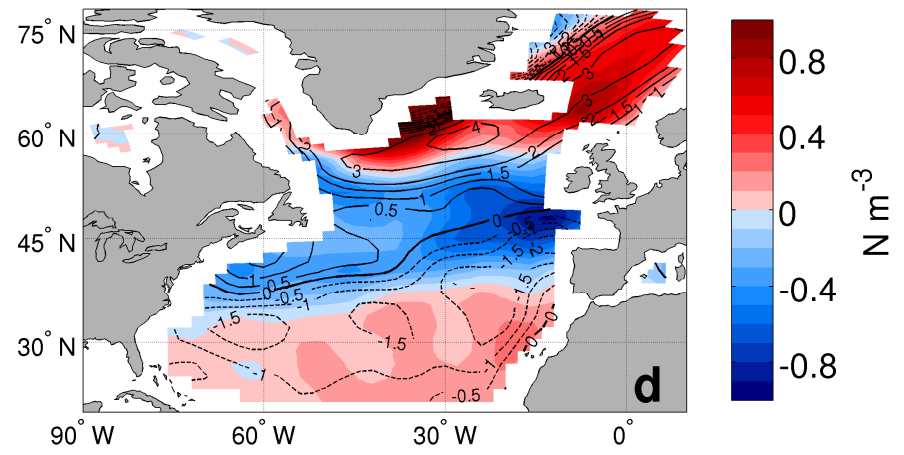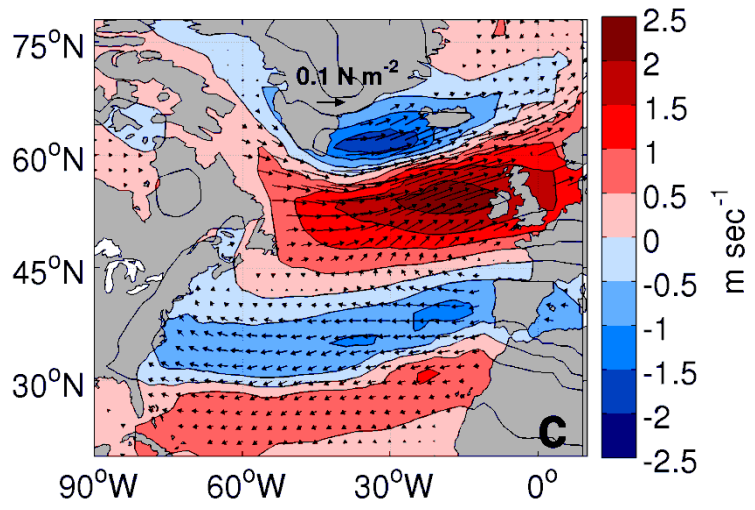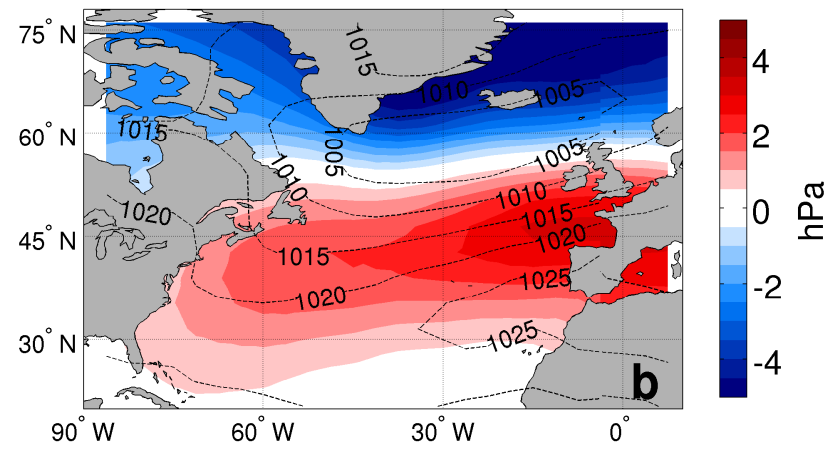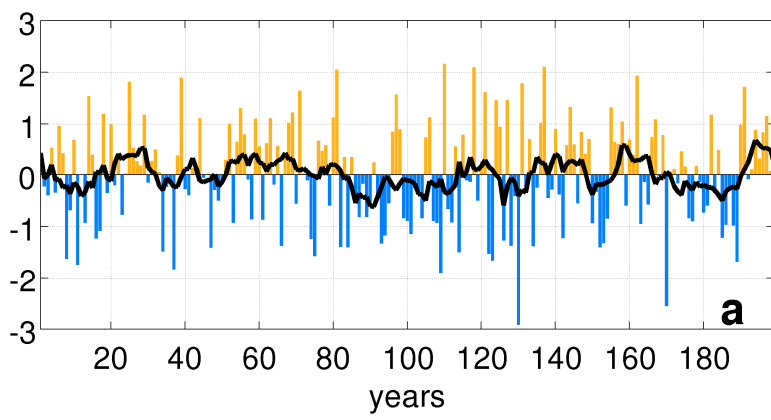
Fig. 4-2 DJFM North Atlantic atmospheric variability. **(a)** NAO index (NAO+ in yellow bars, NAO-in blue bars) and its 9-point running mean (black line), **(b)** sea level pressure (hPa) climatology (contours) and regression onto NAO index (colors), **(c)** regression onto NAO index of wind stress (arrows, in N m⁻²) and wind speed at 10 m height (colors, in m sec⁻¹), **(d)** wind stress curl (N m⁻³×10⁻⁷) climatology (contours) and regression onto NAO index (colors).
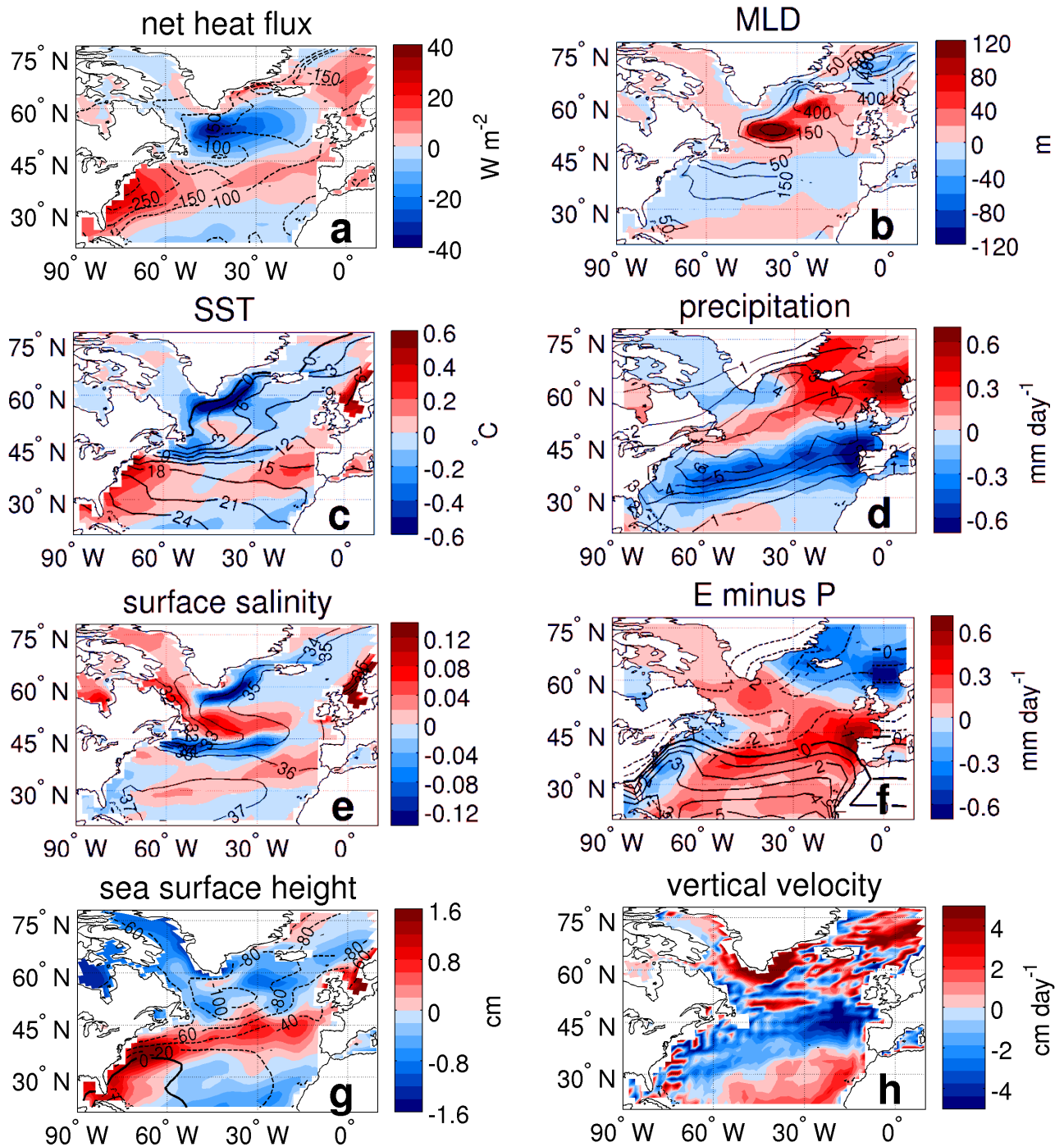
63

4.3 Direct response to the NAO
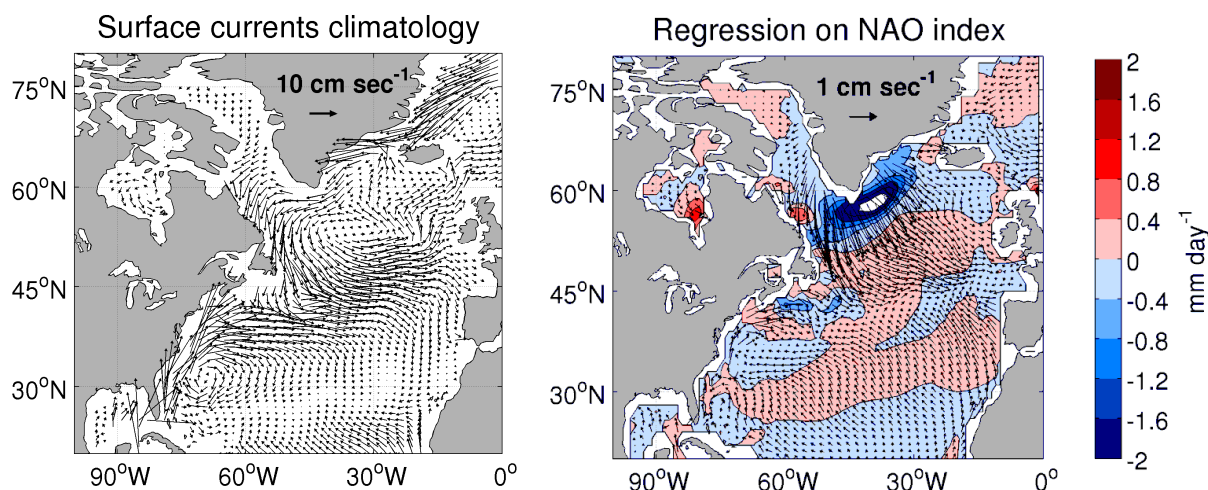
4.3.1 Spatial response

In this section the effect of interannual wind fluctuations on physical and biogeochemical properties over the North Atlantic Ocean will be explored. Physical variables are seasonally averaged over the winter season (DJFM) which is the period of strongest response to atmospheric forcing; for marine biogeochemistry, since we do not yet know when the highest response to NAO will take place, an annual average is performed. Here in Section 4.3.1 we focus on the temporally averaged spatial response, whereas the investigation of the seasonal response is deferred to Section 4.3.2. Fig. 4-3 shows the regression between the standardized NAO index and DJFM time series of physical variables (in colors) described by the regression coefficient of the variable onto the NAO index. For reference, the respective climatological values are included as contours. The displayed anomalies thus correspond to NAO index values equal to 1 (Fig. 4-2a): however it has to be noted that a strong NAO index will produce about twice the anomalies shown in Fig. 4-3.

Coherent patterns of spatial variability are detected in response to interannual wind fluctuations. Changes in wind speed and atmospheric circulation affect net heat fluxes (Fig. 4-3a) mainly in response to sensible and latent heat fluxes (Cayan, 1992). During NAO+ phases ocean heat losses increase in the subpolar gyre and south of 30°N (~30% with respect to climatology) whereas they decrease at middle latitudes and in the Norwegian Sea. Associated buoyancy changes affect upper ocean mixing (Fig. 4-3b), with largest modifications occurring in the subpolar gyre, where the MLD deepening exceeds 120 m (>30% variation with respect to climatology). Increased stratification occurs instead at mid-latitudes, even though changes are less pronounced than at higher latitudes. The SST response (Fig. 4-3c) to local variations in surface heat fluxes results in a tripolar structure of simultaneous SST decrease at subpolar and tropical latitudes, and increase at mid-latitudes. Compared to observed variability (Visbeck et al., 2003), the simulated SST response to NAO is reasonably simulated, even though a positive SST anomaly interrupts the negative pattern at subpolar latitudes. This is possibly due to an overly strong response of the MLD to NAO+ forcing which promotes mixing to the surface layer of relatively warmer subsurface waters.

During NAO+ phases, the northward displacement of the storm track and associated moisture transport result in a precipitation increase of about 10-20% with respect to climatology north of 45°N and decrease between 30°-45°N and in the Labrador Sea (Fig. 4-3d). Salinity (Fig. 4-3e) decreases by more than 0.1 at 40-45°N and east of Greenland, and increases in the subpolar gyre, in the western Labrador Sea and at subtropical latitudes. Salinity changes appear to arise from modifications in surface freshwater fluxes (Fig. 4-3f) and from changes in surface freshwater advection (Fig. 4-4 right). Evaporation minus precipitation (E minus P) is enhanced throughout the subpolar latitudes (0.2-0.3 mm day^{-1}) because of increased evaporation (related to latent heat losses) and at middle latitudes (0.3-0.5 mm day^{-1}) because of decreased precipitation. Surface freshwater fluxes due to advective processes increase by more than 2 mm day^{-1} south of Greenland because of enhanced southward motion of surface currents (Fig. 4-4 right), which arise as a wind-driven response to wind stress curl anomalies. The importance of wind-driven advective processes in determining the response of total freshwater flux to NAO on interannual time scales was also shown by Visbeck et al. (2003). During NAO+ phases sea surface height (Fig. 4-3g) increases at mid-latitudes, caused by enhanced heat and mass convergence by large-scale surface current anomalies (Fig. 4-4 right).
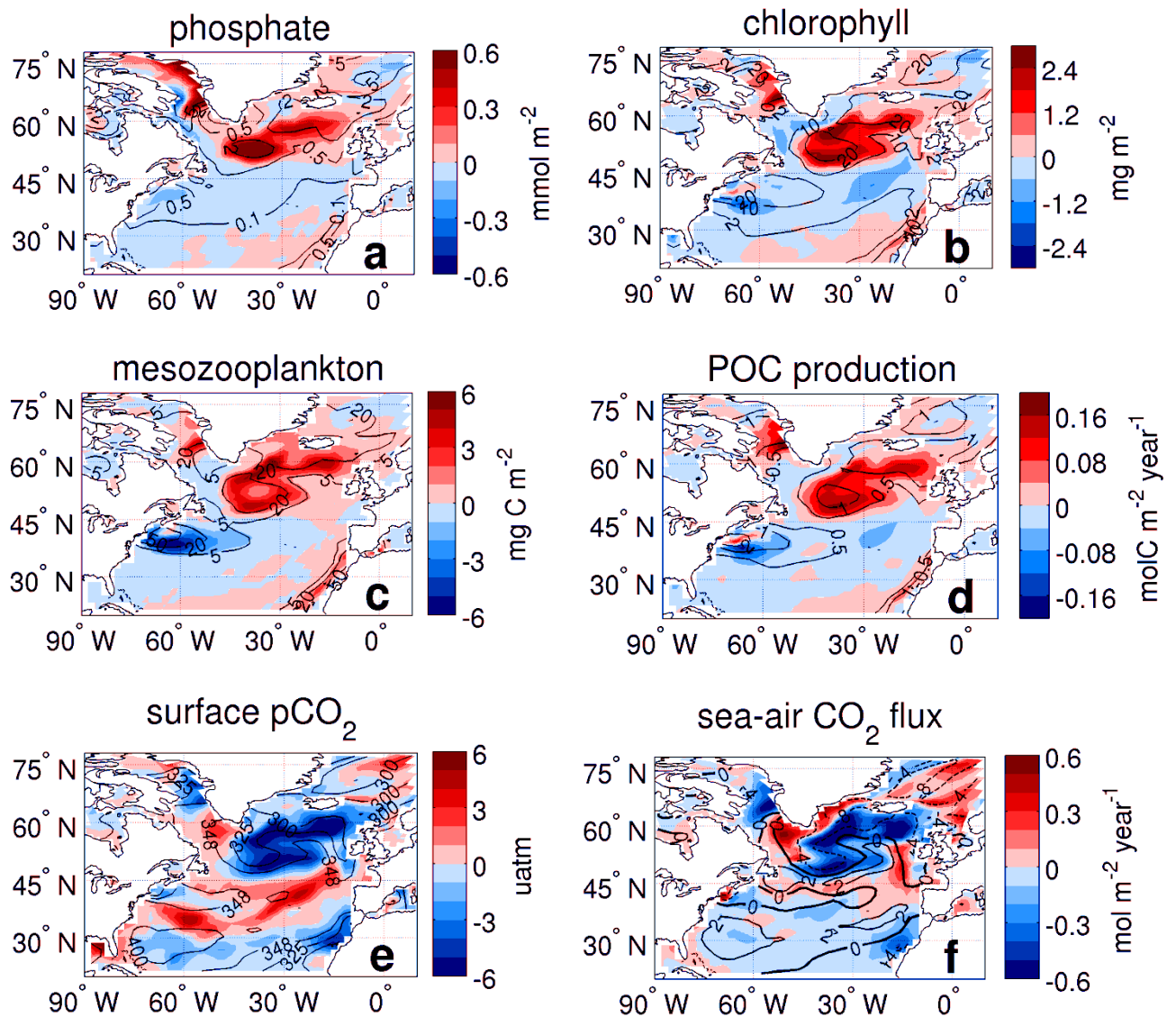
Fig. 4-3 DJFM climatologies (contours) and regression onto the NAO index (colors) of DJFM anomalies of **(a)** net surface heat flux in W m^{-2} (defined positive downwards), **(b)** mixed layer depth (MLD) in m, **(c)** sea surface temperature (SST) in °C, **(d)** precipitation in mm day^{-1}, **(e)** surface salinity, **(f)** evaporation minus precipitation (E minus P) in mm day^{-1}, **(g)** sea surface height in cm, **(h)** ocean vertical velocity at 50 m depth in cm day^{-1}.

Fig. 4-4 (left) DJFM surface current climatology (cm sec^{-1}), **(right)** DJFM surface currents regressed onto NAO index and salinity flux due to surface horizontal advection (mm day^{-1}).

Having assessed that the physical ocean response simulated by our model is reasonably similar to observational estimates, we now investigate how changes in upper ocean physics during winter affect spatial structures of marine biogeochemistry throughout the year. To this end we show in Fig. 4-5 linear regressions between annual time series of selected biogeochemical properties and standardized NAO index. The depicted variables are integrated throughout the euphotic layer in panels a-d and defined at the surface in panels e-f.

Phosphate concentration (Fig. 4-5a), which in this model is one of the major nutrients limiting phytoplankton growth, is overall positively correlated to winter MLD variations, indicating higher nutrient supply (~30%) when winter vertical mixing is deeper (i.e. NAO+). The NAO explains ~10-30% of phosphate fluctuations in the subpolar gyre and in the western mid-latitudes (Fig. 4-6a). In addition to changes in mixing, subsurface ocean vertical velocities (Fig. 4-3h) induced by anomalous wind stress curl (Fig. 4-2d) may also lead to changes in nutrient supply (as found by Oschlies, 2001). However since the simulated NAO anomalies of ocean vertical velocities are in the order of a few cm day^{-1}, we expect that on interannual time scales changes in mixing will have a stronger effect on nutrient entrainment than vertical advection.

Fig. 4-5 Climatologies (contours) and regression onto NAO index (colors) of annual anomalies of **(a)** phosphate in mmol m^{-2}, **(b)** total chlorophyll in mg m^{-2}, **(c)** mesozooplankton in mg C m^{-2}, **(d)** particulate organic carbon (POC) production in mol C m^{-2} year^{-1}, **(e)** surface CO_2 partial pressure (pCO$_2$) in µatm, **(f)** sea-air CO_2 flux (defined positive upwards) in mol C m^{-2} year^{-1}. Variables in panels a-d are integrated over the euphotic depth.

Phytoplankton growth can be described as a local balance between nutrient availability, which is positively correlated with vertical mixing, and residence time within the sunlit euphotic layer, which instead increases with stratification. In fact vertical mixing beyond a threshold depth may result in reduced phytoplankton growth because the cells, though nutrient-replete, continue to be mixed down to a depth where they become light-limited. This threshold depth, estimated by Follows and Dutkiewicz (2002) to be around 20-60 m according to solar radiation levels, is generally not met at low latitudes whereas it is commonly exceeded at high latitudes during the winter months (Siegel et al., 2002). According to latitude and season, nutrient and light limitation may thus exert

differing pressures on phytoplankton growth. In the present study we observe that during NAO+ phases, chlorophyll concentration (Fig. 4-5b), which can be considered as a proxy of phytoplankton biomass, increases by ~10% in the subpolar gyre, in the eastern Labrador Sea, and off the northwestern African coast, whereas it decreases at middle latitudes.
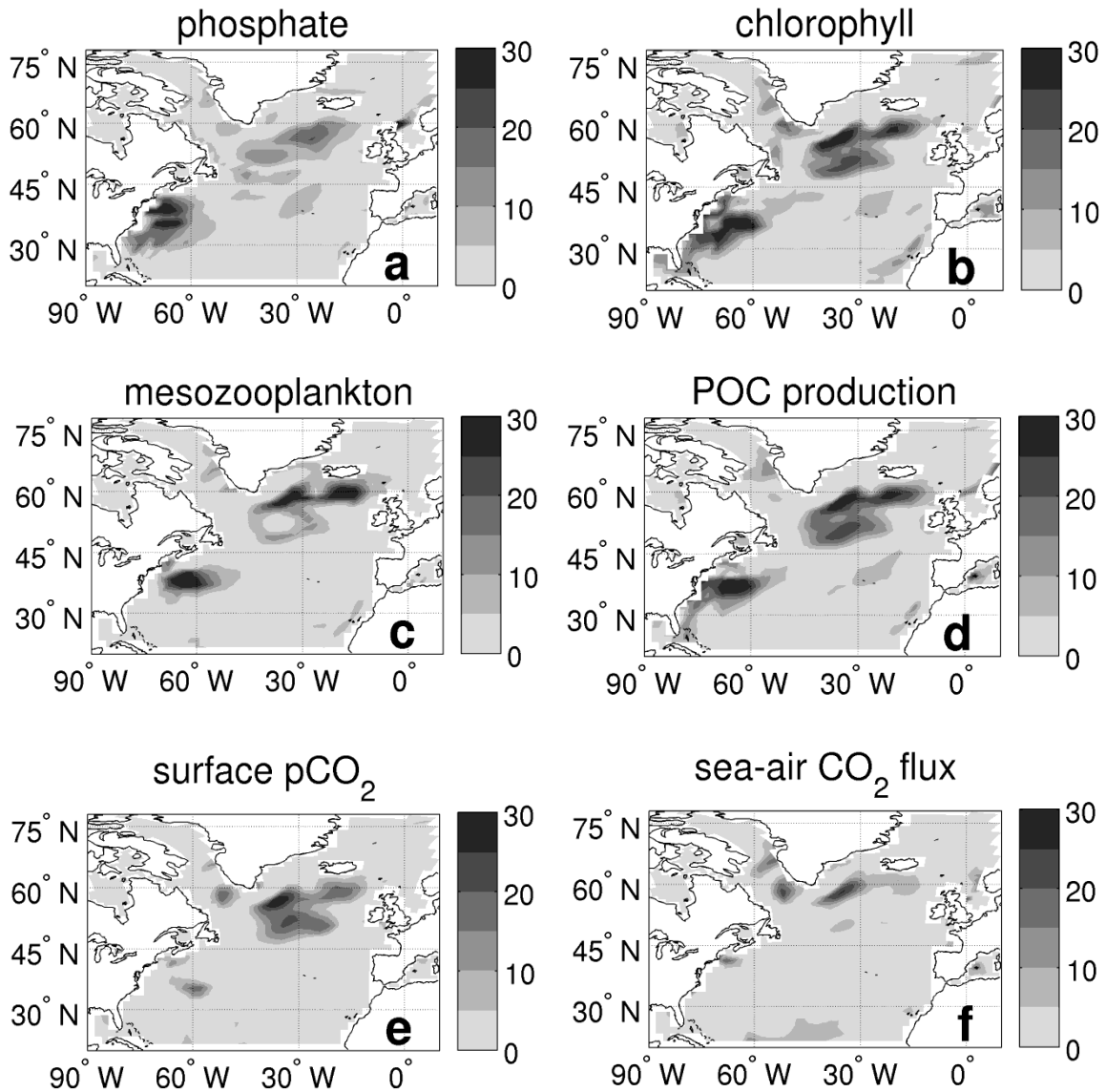
Fig. 4-6 Variance explained by the NAO index (%) of **(a)** euphotic-depth-integrated phosphate concentration, **(b)** euphotic-depth-integrated chlorophyll concentration, **(c)** euphotic-depth-integrated mesozooplankton concentration, **(d)** euphotic-depth-integrated particulate organic carbon (POC) production, **(e)** surface CO_2 partial pressure (pCO_2), **(f)** sea-air CO_2 flux.

The overall positive correlation between annual chlorophyll concentration and winter MLD variations indicates that on an annual scale nutrient limitation is relatively more important in determining phytoplankton variability than it is light limitation. Despite general spatial correspondence between annual phosphate and chlorophyll anomalies,

some dissimilarity is evident. The largest chlorophyll increase at subpolar latitudes occurs not in the area of MLD and nutrient maxima but at its edges. Evidently here the balance between light and nutrient limitations is optimal for phytoplankton growth. It may also be speculated that the chlorophyll increase off the northwestern African coast might be more related to increased upwelling caused by positive wind stress curl anomalies, rather than to changes in mixing, which are only slight in this area. This result is consistent with the study of Oschlies (2001) who finds increased advective nitrate supply of ~1 mol m^{-2} year^{-1} during NAO+ phases along the northwestern African coast.

Chlorophyll variability affects mesozooplankton biomass (Fig. 4-5c) which increases during NAO+ phases of ~30% in the subpolar gyre and decreases at mid-latitudes with spatial structures similar to the chlorophyll changes. Changes in phyto- and zooplankton productivity affect in turn particulate organic carbon (hereafter POC) production which during NAO+ phases increases at subpolar latitudes and decreases at mid-latitudes by ~10% (Fig. 4-5d). The NAO index generally explains up to 30% of the variance of chlorophyll, zooplankton and POC production in the subpolar gyre and in the western mid-latitudes.

The chlorophyll increase found in the subpolar gyre during NAO+ phases does not agree with previous findings, based on a few years of satellite data, that in the Irminger Basin a bloom delay during NAO+ years related to deeper mixing decreases the magnitude of the subsequent spring bloom (Henson et al., 2006). Follows and Dutkiewicz (2002) however observe that over the whole subpolar region a clear interannual signal is not discernible and invoke several mechanisms including small scales and intermittency driving restratification processes, which the coarse resolution model used in this study is not able to capture. However authors also discuss that it is likely that the shortness of the time series and the poorer satellite data coverage at higher latitudes due to cloudiness may also be causing these different results. Longer and spatially-integrated observational records are thus required to assess prevailing mechanisms.

Even though available SeaWiFS chlorophyll time series are too short to provide a robust statistical framework, for reference we show in Fig. 4-7 regressions between the April-July (AMJJ) chlorophyll concentration anomalies over the euphotic depth and the simulated NAO index, and the SeaWiFS chlorophyll time series for the years 1998-

70

2006 (McClain, 2009) regressed onto the Hurrell NAO index (http://www.cgd.ucar.edu/cas/jhurrell/indices.html); AMJJ climatologies are shown in contours for reference. It may be first of all noted that the model correctly captures the amplitude of the anomalies corresponding to an NAO index equal to 1. Moreover it may be seen that tropical and subtropical latitudes exhibit a similar response between model and observations, whereas at subpolar latitudes the results differ as already discussed previously. The chlorophyll concentration decrease found during NAO+ phases by Henson et al. (2006) in the Irminger Basin may be seen. However other areas south of Greenland and Iceland exhibit a strongly positive response which we might hypothesize to be due to increased nutrient availability driven by deeper mixing.
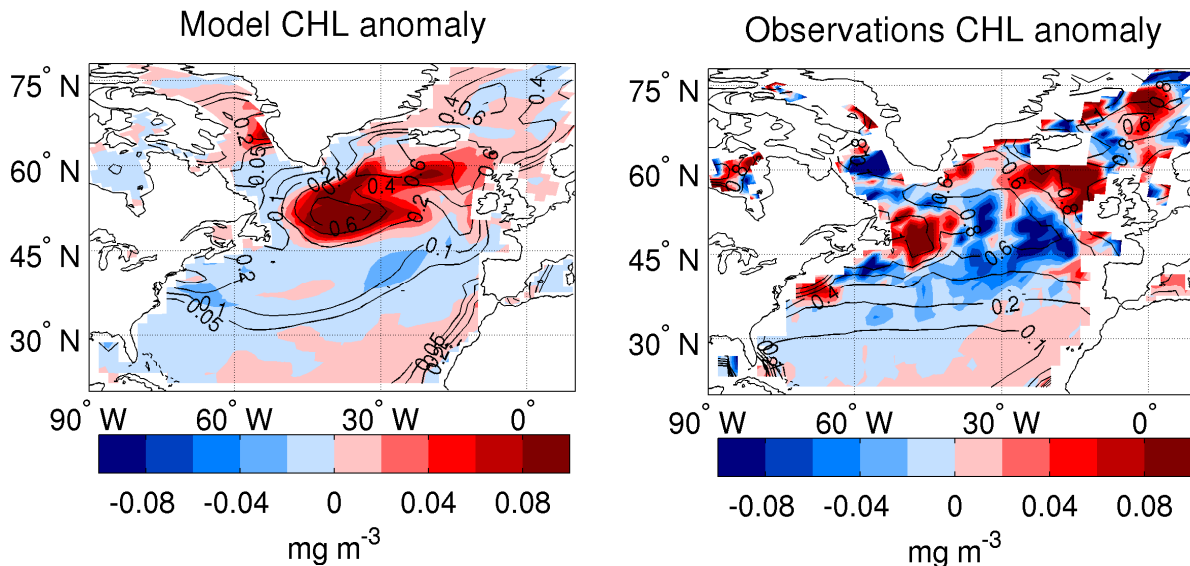
Fig. 4-7: (a) simulated chlorophyll concentration in spring (AMJJ) anomalies averaged over the euphotic layer depth (mg m^{-3}) regressed onto the normalized simulated NAO index and **(b)** spring (AMJJ) SeaWiFS satellite chlorophyll concentration anomalies (mg m^{-3}) during the years 1998-2006 regressed onto the normalized observed Hurrell NAO index.

Climatological CO_2 partial pressure (hereafter pCO_2) at the ocean surface (Fig. 4-5e) depends on both physical and biological factors: increased MLD increases pCO_2 entrainment of carbon-rich waters, increased phytoplankton biomass lowers pCO_2 by biological uptake, and increased temperature increases pCO_2. Ocean-atmosphere pCO_2 differences drive a CO_2 flux between the two compartments whose amplitude depends on wind speed squared (Wanninkhof, 1992). Climatological CO_2 fluxes in our model (Fig. 4-5f) show the subpolar latitudes as being a permanent sink of atmospheric CO_2, with magnitudes of ~4 mol C m^{-2} year^{-1}, similar to those estimated from observations

(Koertzinger et al., 2008; Takahashi et al., 2009). Middle and subtropical latitudes are either neutral or a source of CO_2, in contrast to observational estimates (Takahashi et al., 2009) which show the zero-line of CO_2 fluxes shifted much more to the south. This result might be explained by considering that atmospheric CO_2 concentrations in our simulation are lower than those occurring in the 1990s, included between 350 and 360 ppm (Bates, 2007). It is also possible that, since our model overestimates winter MLD in the western mid-latitudes (Fig. 2-8), enhanced entrainment of carbon-rich waters in winter might produce an overestimation of winter CO_2 outgassing.

In response to NAO wind variability, the model results show that changes in surface ocean pCO_2, in the order of 5 µatm, are inversely correlated to chlorophyll concentration and MLD, thus indicating that on an annual time scale the dominant control on surface pCO_2 interannual variability is exerted by biological processes. NAO interannual variability gives rise to modifications in sea-air CO_2 fluxes through changes in surface pCO_2, wind speed, and SST (which affects CO_2 solubility in seawater). The subpolar gyre shows the largest response, with increased ocean CO_2 uptake occurring during NAO+ phases because of higher biological uptake, lower SST, and stronger winds. This result agrees with observational studies based on fixed-point time series in the northern North Atlantic (Olsen et al., 2003) and in the northeastern Atlantic (Santana-Casiano et al., 2007), and with an ocean-marine biogeochemistry modeling study (Thomas et al., 2008). Changes in sea-air CO_2 flux between 30°-45°N are close to zero (as also found by Bates, 2007) despite rather large modifications in surface pCO_2. This effect is related to the fact that during NAO+ phases wind speed decreases between 30°-45°N (Fig. 4-1c) thus causing CO_2 flux to decrease in amplitude. The variance explained by the NAO in affecting CO_2 fluxes is rather low (<5% on large areas).

4.3.2 Seasonal response

The seasonal response of marine biogeochemistry to NAO winter forcing is analyzed in two different geographical locations: one is in the subpolar gyre (48°-55°N; 45°-30°W), the other one in the Sargasso Sea around the Bermuda Atlantic Time Series (BATS) station (30°-40°N; 70°-60°W). In Figs. 4-8 and 4-10 monthly composites during NAO+ and NAO- years, defined as those in which the NAO index exceeds ±1 standard deviation, are shown and compared with monthly climatologies.

At subpolar latitudes (Fig. 4-8), the winter climatological means indicate that deep mixing (Fig. 4-8a) and typically low incoming solar radiation limit phytoplankton growth despite high nutrient availability (Fig. 4-8b). In spring the upper water column stratifies and the phytoplankton bloom initiates (Fig. 4-8c). The diatom peak, occurring in May in agreement with observations (McClain, 2009), sustains with two months delay a mesozooplankton biomass maximum (Fig. 4-8d). We remark that the model does not simulate the climatological autumn phytoplankton maximum (Mann and Lazier, 1996) because of underestimation of ocean mixing in autumn (Fig. 4-8a). Phytoplankton primary production is partly respired by heterotrophic oxidation reactions, and partly transferred to higher trophic levels or to dissolved and particulate organic matter (Fig. 4-8e) pools.

Winter MLD interannual variability has significant impacts on nutrient availability and on light levels experienced by phytoplankton. Our results show that during NAO+ (NAO-) phases, diatom biomass decreases (increases) between January and April even though nutrient concentrations are higher (lower), as reported by Henson et al. (2006). This result may be explained by considering that deeper winter mixed layer depths reduce the retention time of phytoplankton inside the euphotic layer. Conversely, shallower mixed layers allow for an earlier increase of phytoplankton growth. However, during the subsequent months (May-July) phytoplankton biomass and bloom duration are larger when deeper mixing has occurred in winter, i.e. during NAO+ phases, because of higher nutrient availability.
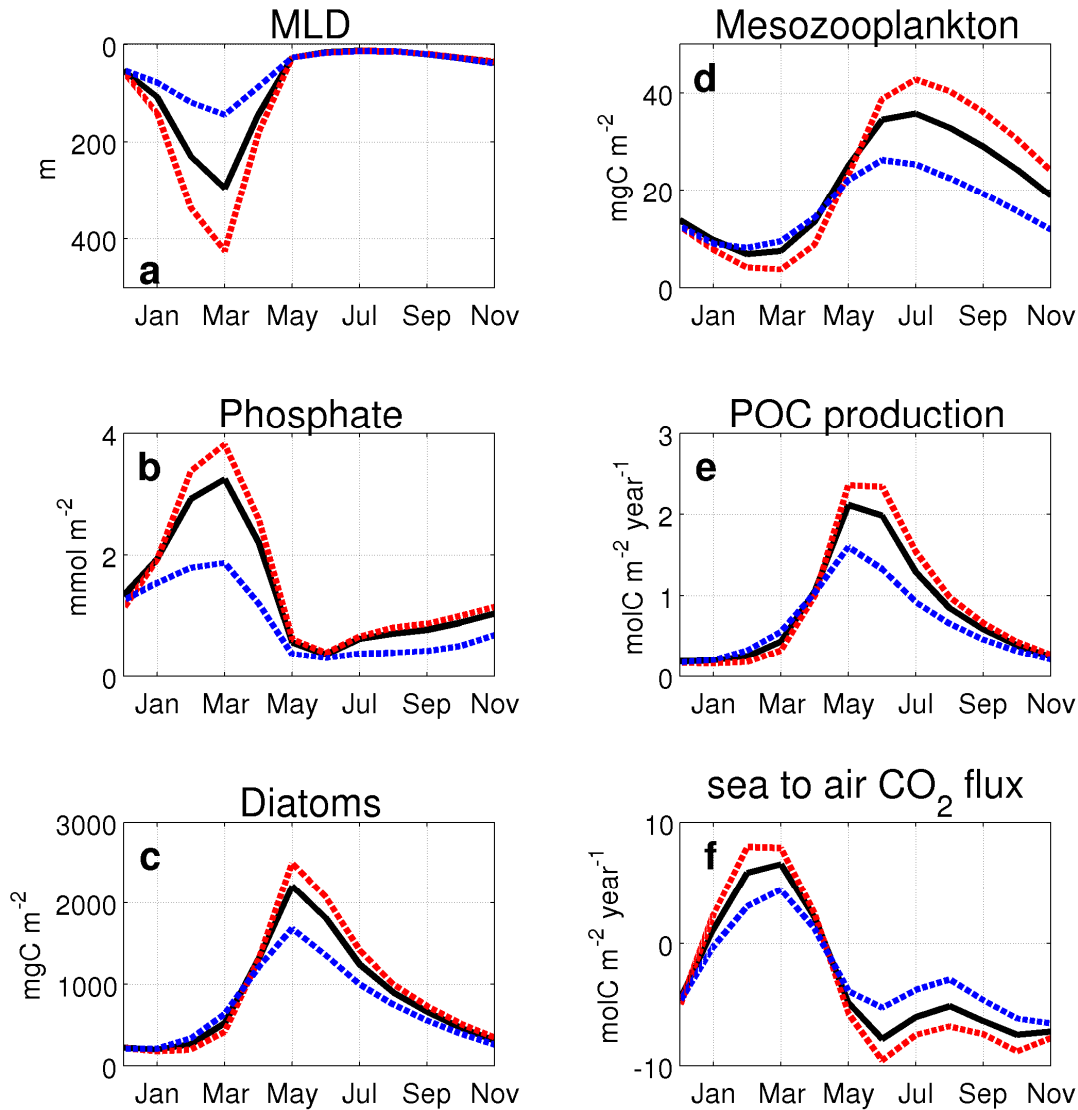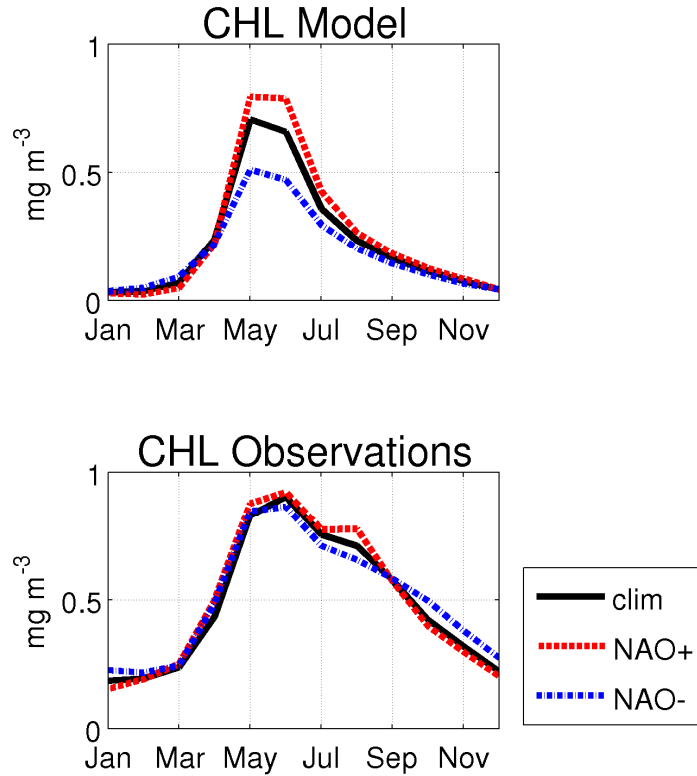
Fig. 4-8 Climatological (black), NAO+ (red), and NAO- (blue) seasonal cycles in the subpolar gyre region of **(a)** mixed layer depth in m (note reversed axis), **(b)** phosphate concentration in mmol m^{-2}, **(c)** diatom concentration in mg C m^{-2}, **(d)** mesozooplankton concentration in mg C m^{-2}, **(e)** particulate organic carbon (POC) production in mol C m^{-2} year^{-1}, **(f)** sea-air CO$_2$ flux (defined positive upwards) in mol C m^{-2} year^{-1}. Variables in panels b-e are integrated over the euphotic depth.

We then conclude that changes in winter mixing affect not only the mean annual phytoplankton biomass, but also the amplitude and length of the seasonal cycle: during NAO+ phases, the seasonal cycle amplifies and the summer maximum lasts longer, during NAO- phases the seasonal cycle amplitude is reduced. Temporal fluctuations of the subpolar gyre phytoplankton bloom initiation in the order of 2-3 weeks are observed in relation to NAO-induced changes in light conditions (Henson et al., 2009). The temporal resolution of the model used in this study does not allow discrimination of temporal shifts below the monthly scale. We do not find changes in timing of the

phytoplankton seasonal peak, but we do find that the seasonal peaks of mesozooplankton and POC production are shifted of one month between NAO+ and NAO- phases and that their seasonal cycle is modified consistently with phytoplankton biomass variability.

For reference we show in Fig. 4-9 composite NAO+ and NAO- seasonal cycles of chlorophyll concentration averaged over subpolar latitudes (45°-60°N) for SeaWiFS satellite values available for 1998-2006 (top) and for model chlorophyll averaged over the euphotic depth (bottom). Composites are calculated by selecting years in which the observed and simulated normalized NAO index exceeds +1 (-1) standard deviation. The model simulates rather well the magnitude and timing of the spring phytoplankton bloom, even though it exhibits an anticipated bloom ending and underestimated chlorophyll values in autumn-winter. In response to NAO+ phases SeaWiFS satellite estimates show a slight decrease of chlorophyll concentrations in winter and an increase in spring-summer, as seen in the model results analyzed in this study. We may therefore hypothesize that the processes found in the model leading to chlorophyll changes may indeed be valid. However it has to be stressed that these are only speculations, as the shortness of the satellite time series does not allow robust statistics.

Climatological sea-air CO_2 fluxes (Fig. 4-8f) exhibit seasonal oscillations with the ocean being a source of CO_2 in winter, when deep mixing entrains subsurface carbon-rich waters, and a sink in the remaining part of the year, when pCO_2 is lowered by the biological and solubility pumps, consistently with observations (Koertzinger et al., 2008). During NAO+ phases, deep winter mixing of carbon-rich waters increases winter CO_2 outgassing, whereas lower SST and increased primary production in the subsequent months increase ocean CO_2 uptake. Despite increased winter CO_2 outgassing, the annual net of these two processes results in an increase in ocean CO_2 uptake during NAO+ phases.

Fig. 4-9 Climatological (black), NAO+ (red), and NAO- (blue) seasonal cycles in the subpolar latitudes of the North Atlantic (50°-60°N,50°-10°W) of **(top)** SeaWiFS satellite estimates of chlorophyll values (mg m^{-3}) during the years 1998-2006 and **(bottom)** model chlorophyll concentration (mg m^{-3}).

The BATS area (Fig. 4-10) is located in the northwestern Atlantic in the transition zone between easterlies and westerlies and in a region of near zero mean geostrophic circulation (Bates, 2007). It represents the equatorward limit of significant winter mixing and is then expected to be largely influenced by interannual changes in atmospheric and oceanic forcing (Longhurst, 2007). Compared to the subpolar regime, mixed layers are shallower and upper-ocean nutrient, phytoplankton and zooplankton concentrations are lower. Nutrient limitation is more effective in controlling phytoplankton growth than light limitation, and the phytoplankton and zooplankton blooms occur coincidentally or with little delay with respect to the MLD seasonal maximum (Fig. 4-10 a-d). POC production (Fig. 4-10e) is lower than at subpolar latitudes, both because primary production is lower, and because the phytoplankton community is characterized by a higher nanophytoplankton fraction (not shown) having lower POC production rates.
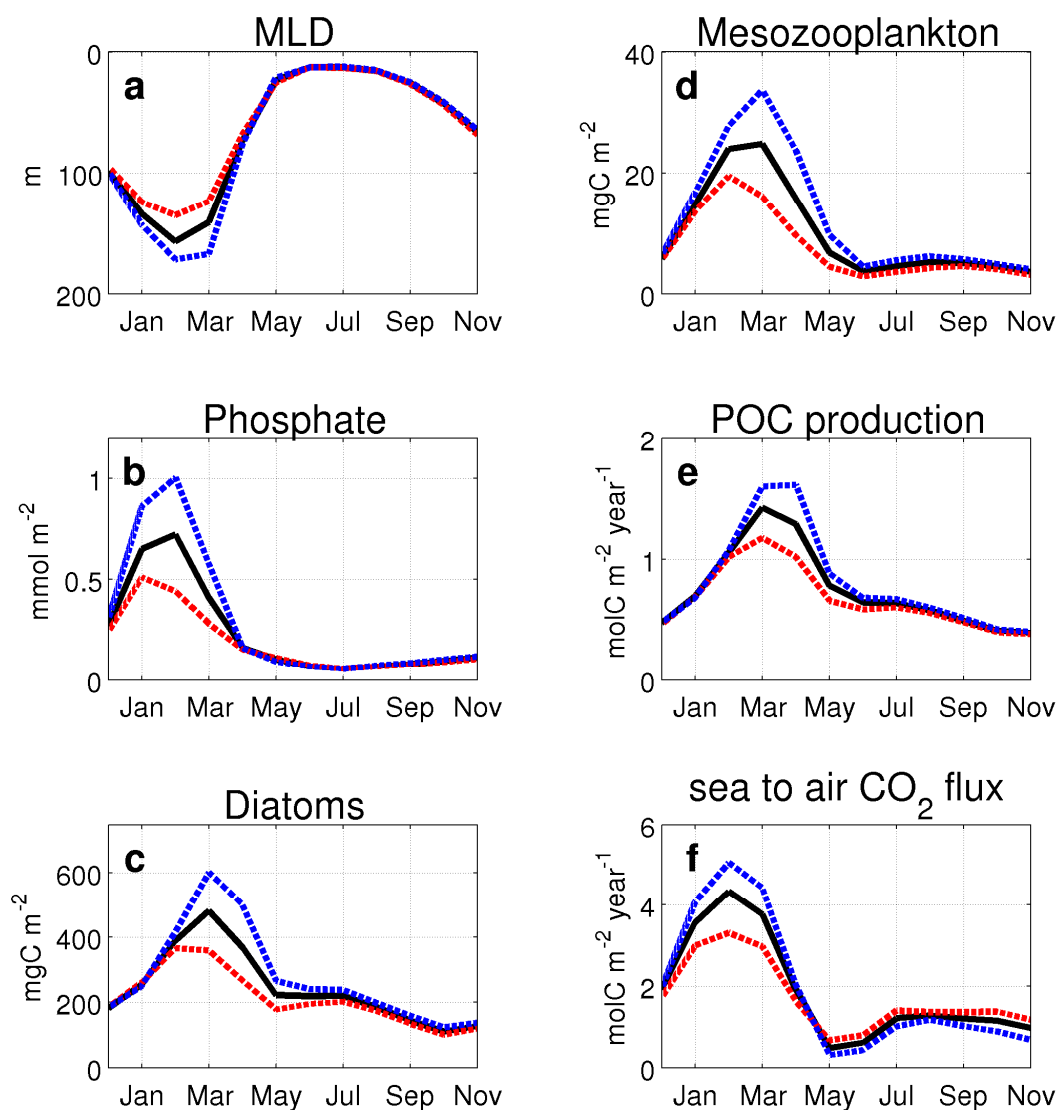
Fig. 4-10 Climatological (black), NAO+ (red) and NAO- (blue) seasonal cycles in the Sargasso Sea near BATS of **(a)** mixed layer depth in m (note reversed axis), **(b)** phosphate concentration in mmol PO_4 m^{-2}, **(c)** diatom concentration in mg C m^{-2}, **(d)** mesozooplankton concentration in mg C m^{-2}, **(e)** particulate organic carbon (POC) production in mol C m^{-2} year^{-1}, **(f)** sea-air CO_2 flux (defined positive upwards) in mol C m^{-2} year^{-1}. Variables in panels b-e are integrated over the euphotic depth.

NAO-related changes in winds drive an opposite response with respect to subpolar latitudes of MLD which shoals during NAO+ phases and deepens during NAO- phases. MLD interannual variability (Fig. 4-10a), though less pronounced than in the subpolar gyre, yet causes a 25% change in phosphate concentrations (Fig. 4-10b), with consistent impacts on the seasonal cycle amplitude and phase of all biological components. During NAO+ phases, shallower winter MLD causes phytoplankton to peak already in February, i.e. one month earlier than average. This might be due to a combination of increased light availability in winter and insufficient nutrients in following months. A

30-40 day earlier bloom start during NAO+ phases was also found at mid-latitudes by Henson et al., (2009) caused by increased retention inside the euphotic layer. In contrast to subpolar latitudes (Fig. 4-8) winter phytoplankton biomass does not increase when MLDs are shallower, because at these latitudes light limitation is less effective than nutrient limitation in controlling phytoplankton growth. In general, we observe that in this model changes in amplitude of the seasonal cycle are more typical of subpolar latitudes, whereas changes in phase are more common at subtropical latitudes.

At BATS, the simulated climatological sea-air flux of CO_2 is positive throughout the year (Fig. 4-10f), with higher values during winter and lower values in the remaining part of the year. As already noted in the previous section, our model tends to overestimate ocean outgassing in this area. CO_2 outgassing increases when winter MLD is deeper and decreases when spring biological uptake is higher and SST lower, with a resulting amplification of the seasonal cycle during NAO- phases and reduction during NAO+ phases. However averaged over the whole year NAO interannual variability does not significantly modify CO_2 fluxes.
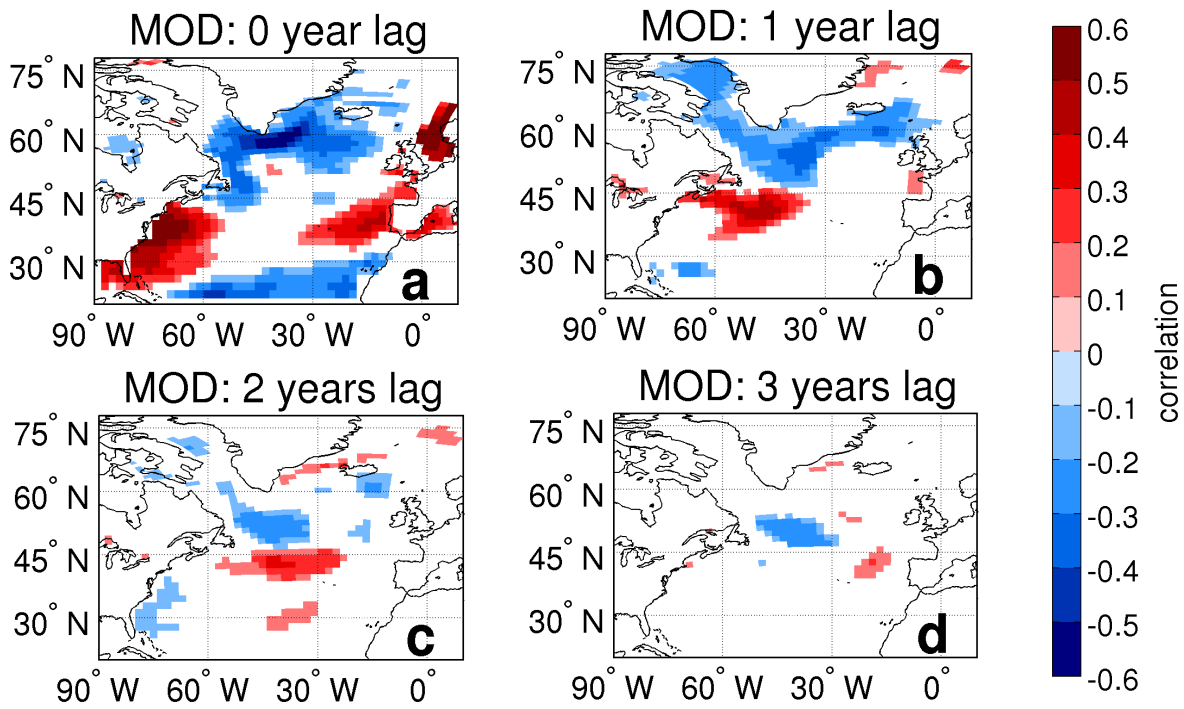
4.4 Lagged response to the NAO

Simulated SST anomalies generated by NAO forcing maintain statistically significant correlations with the NAO index (at 95% confidence level) with lags up to 3 years (Fig. 4-11). Similar ocean memory is found in observational reanalyses such as the 100-year Kaplan winter anomaly SST data set (Kaplan et al., 1998; Visbeck et al., 2003) and the winter Hadley SST reanalysis (Rayner et al., 2003) during the years 1930-2002 (Fig. 4-12). In Fig. 4-12 correlations are computed with respect to the observed station-based Hurrell NAO index (http://www.cgd.ucar.edu/cas/jhurrell/indices.html). The observed persistence is significantly longer than one might expect from local air-sea interaction, yielding decay scale of about 3 months (Frankignoul et al., 1998), and may be explained by the ''reemergence mechanism" (Alexander and Deser, 1995; Deser et al., 2003). This mechanism suggests that a shallow summer thermocline shields subsurface temperature anomalies from atmospheric damping and large current shears, making it possible for the anomalies to become partially re-entrained into the mixed layer during the following winter.
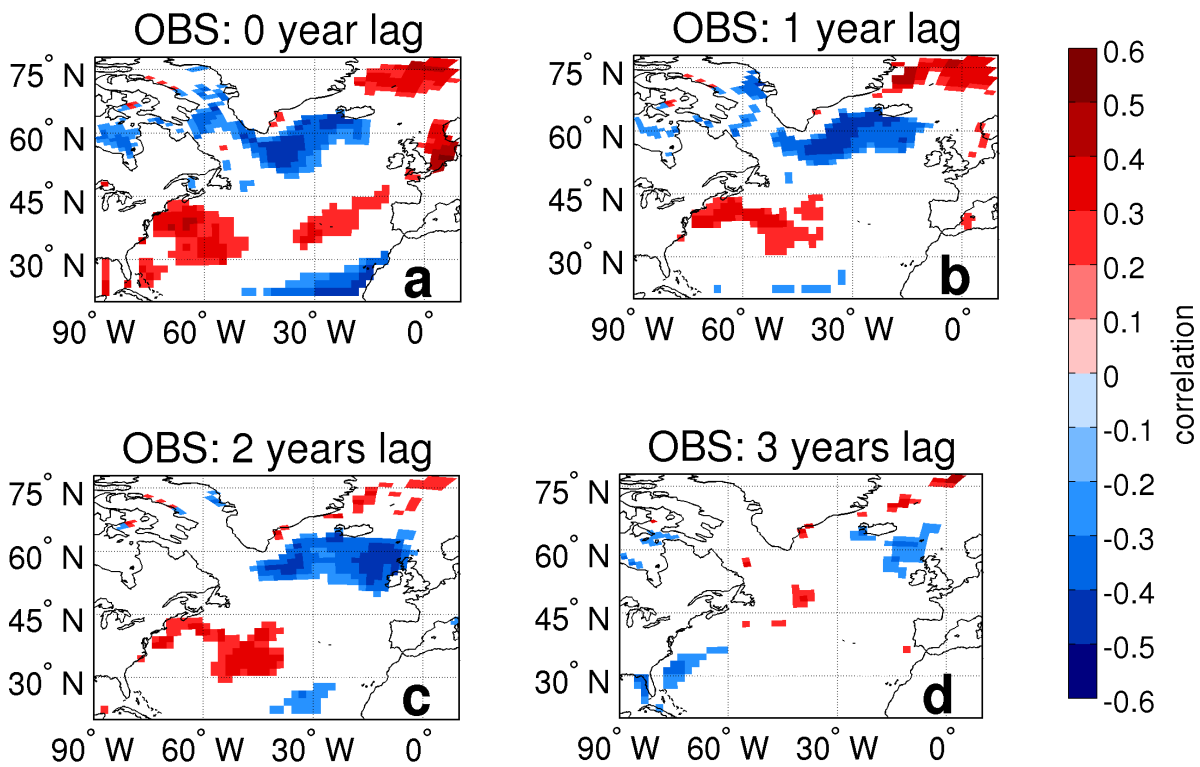
From both model results and observational estimates, SST anomalies show evidence of propagation away from their source region during successive years. In the coupled

simulation analyzed here, SST anomalies generated by NAO+ forcing along the North American coast propagate northeastward in successive years, whereas negative SST anomalies generated in the subpolar gyre persist concentrate in the southern limb of the gyre (Fig. 4-11). In the Hadley SST data set, temperature anomalies are shifted northeastward in successive years even though with slower apparent propagation speeds with respect to the coupled simulation (Fig. 4-12). This behavior might be explained considering that decorrelation time scales in the coupled model are much higher (i.e. 1 year) with respect to the observed values of 3 years (Fig. 4-13): therefore in observations SST anomalies are actively forced in following years by an NAO index of the same sign.
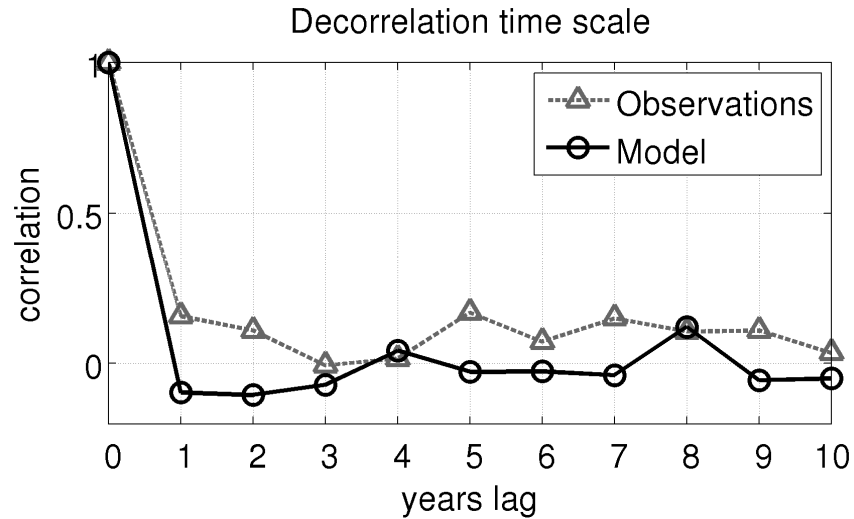
Other observational data sets have also shown evidence of persistent and propagating SST anomalies below the seasonal thermocline close to the Gulf Stream – North Atlantic Current path (Levitus et al., 1994; Sutton and Allen, 1997; Sinha and Topliss, 2006) and in the subpolar gyre (Reverdin et al., 1997). Advection of temperature anomalies by the mean circulation is invoked as a possible mechanism explaining the temporal evolution of SST anomalies (Hansen and Bezdek, 1996; Sutton and Allen, 1997). However Visbeck et al. (1998) and Krahmann et al. (2001) show that the overall cross basin propagation speed depends on the forcing frequency and is not simply set by the advection speed of the upper ocean, suggesting that temperature anomalies are not only passively drifting with ocean currents but also actively forced and destroyed by ocean-atmosphere coupling.
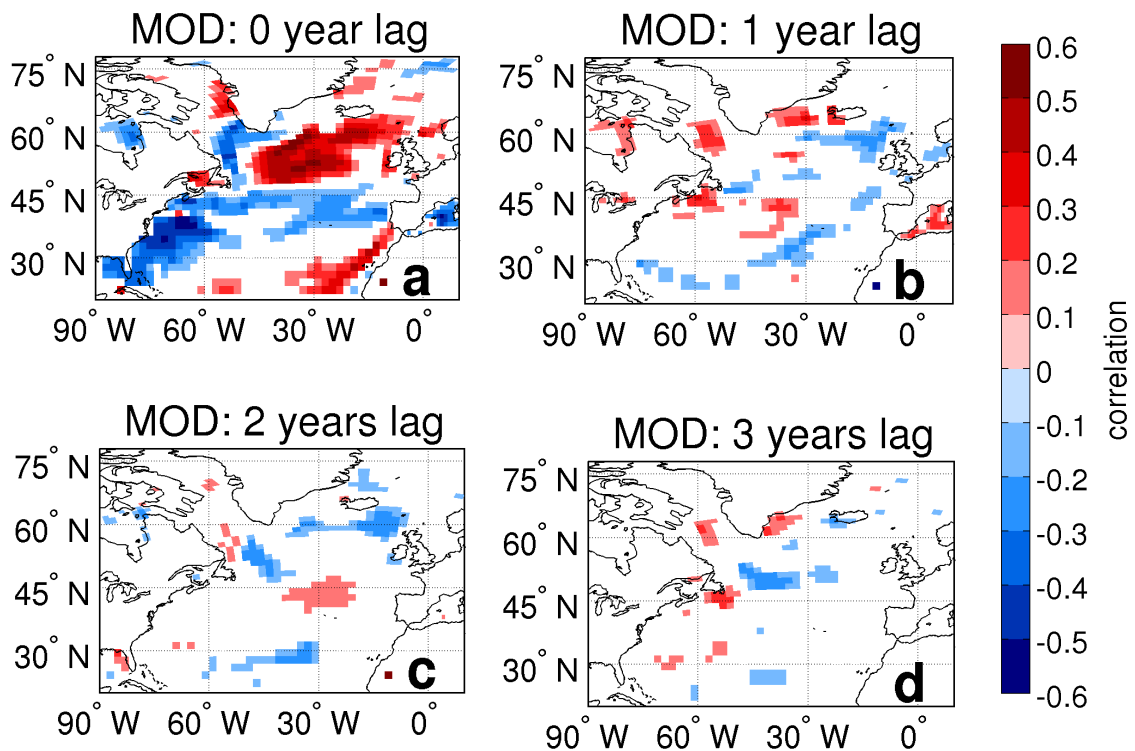
Fig. 4-11 Lagged correlations between NAO index and DJFM SST anomalies with **(a)** no lag, **(b)** 1 year lag, **(c)** 2 years lag, **(d)** 3 years lag. Correlation coefficients lower than 0.14 are not statistically significant at 95% confidence level and are not shown.

Fig. 4-12 Lagged correlations between Hurrell NAO index and Hadley SST DJFM anomalies for the period 1930-2002 with **(a)** no lag, **(b)** 1 year lag, **(c)** 2 years lag, **(d)** 3 years lag. Correlation coefficients lower than 0.24 are not statistically significant at 95% confidence level and are not shown.

Fig. 4-13 Decorrelation time scale for 200 years of the simulated NAO index (black line, circles) and for the 1860-2009 Hurrell NAO index (gray line, triangles).

Fig. 4-14 Lagged correlations between NAO index and spring-summer (AMJJ) chlorophyll anomalies with **(a)** no lag, **(b)** 1 year lag, **(c)** 2 years lag, **(d)** 3 years lag. Correlation coefficients lower than 0.14 are not statistically significant at 95% confidence level and are not shown.

In contrast to SST, correlations between the NAO index and chlorophyll concentration do not show large significance in successive years (Fig. 4-14). This result may be related to possible reasons: (1) simulated marine biogeochemistry is mainly controlled by interannual fluctuations of vertical mixing, characterized by the fast decorrelation

time scales typical of atmospheric signals; (2) nutrients are completely consumed in summer (Figs. 4-8 and 4-10) and thus the biogeochemical system is "re-set" each year.

4.5 Low-frequency response to the NAO

For the analysis of the in-phase ocean response to low-frequency NAO cycles, composite years for positive (NAO+) and negative (NAO-) NAO phases are selected by using the 9-year running average of the NAO index (Fig. 4-2a). For biogeochemical variables, time series detrended with a second order polynomial fit (see Section 2-4) are employed. For the in-quadrature ocean response to low-frequency NAO cycles, transition periods between opposite low-frequency NAO phases symmetrical with respect to the zero-crossing of the NAO index 9-year running average are chosen. The in-phase response will give information on the effect of persistent NAO forcing on ocean properties, whereas the in-quadrature response, characterized by NAO forcing close to zero (not shown), will tell whether the ocean keeps memory of previous phases of low-frequency NAO forcing. In order to test robustness of results, also 9-year running means of the investigated variables are computed and the regression with the 9-year running mean of the NAO index (for the in-phase response) and with its derivative (for the in-quadrature response) calculated. The two methods - regression and composites - yield similar results (not shown). In the following composites will be shown.

The in-phase response of physical ocean properties to low-frequency NAO forcing is shown in Fig. 4-15 (left) for SST, heat content integrated between 0-300 m depth, and sea surface salinity (SSS), and in Fig. 4-16 (top) for sea surface height and horizontal currents averaged between 40-100 m depth.
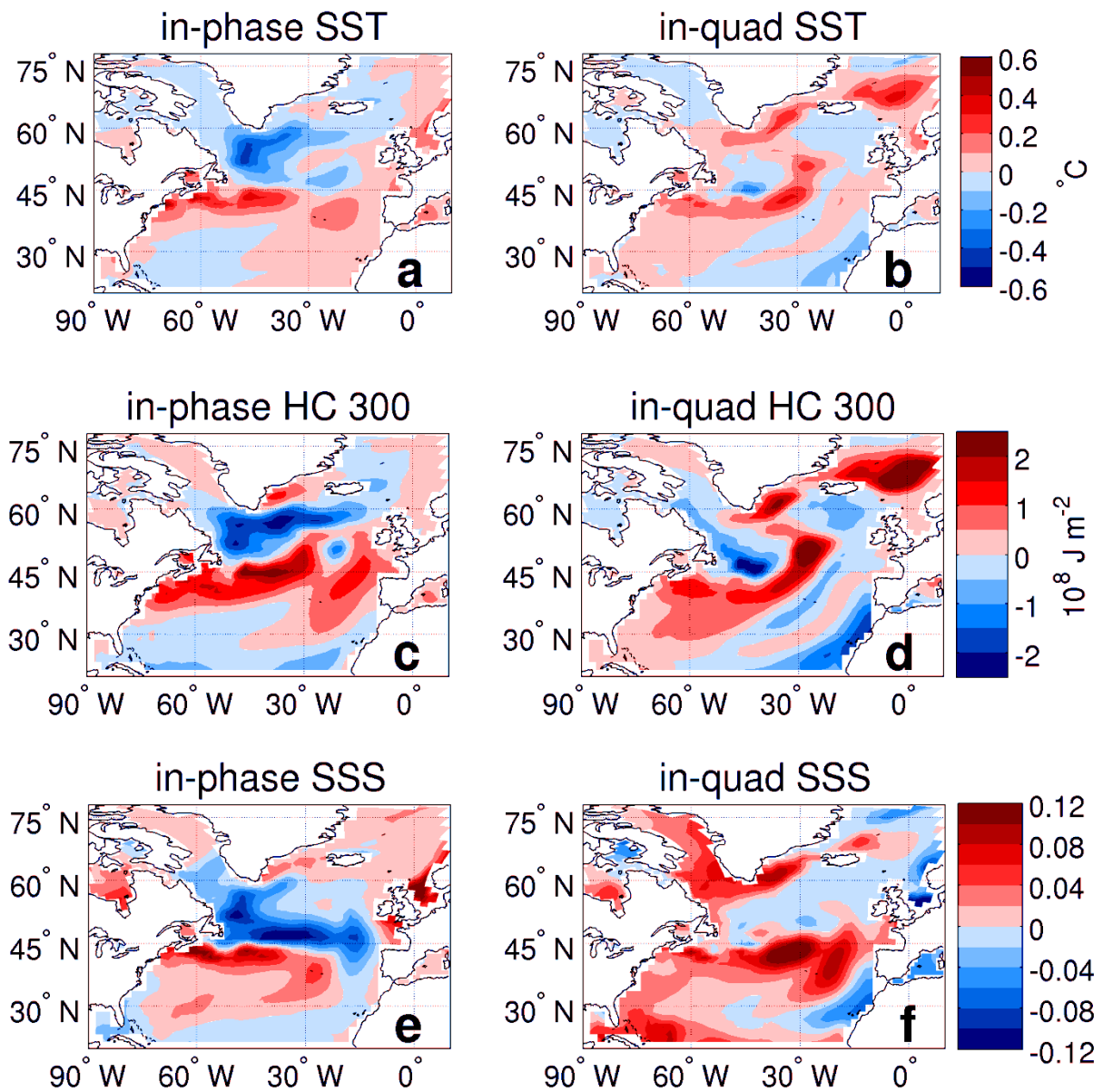
Fig. 4-15 In-phase (left) and in-quadrature (right) response to NAO+ low-frequency phases of (a,b) sea surface temperature (SST) in °C, (c,d) heat content integrated between 0-300 m depth in J m^{-2} and (e,f) sea surface salinity (SSS).
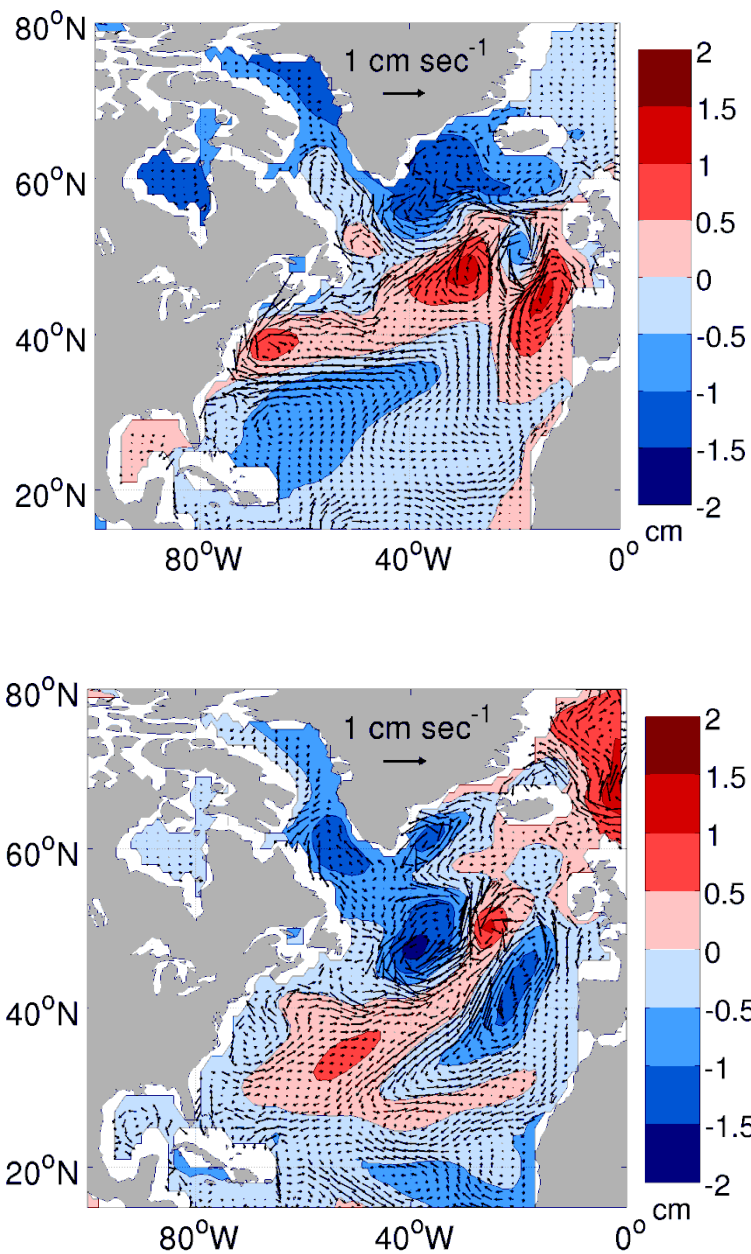
Fig. 4-16 In-phase (top) and in-quadrature (bottom) response to NAO+ low-frequency phases of (a,b) sea surface in cm (colors) and horizontal currents averaged between 40-100 m depth.

At mid-latitudes, positive SST anomalies (Fig. 4-15a) generated by persistent NAO+ phases are concentrated on a narrow zonal band at 40-45°N, instead of covering the whole 30°-45°N area. This structure is possibly related to (1) the time averaging of SST anomalies propagating with yearly lags along the North Atlantic Current, and (2) the increased mass convergence into the area related to persistent wind stress curl anomalies (Fig. 4-2d), which causes positive sea surface height anomalies between 40°-45°N (Fig. 4-16, colors); changes in sea surface height in turn modify horizontal currents through geostrophy giving rise to an anomalous anticyclonic circulation (Fig. 4-16, arrows). The

anomalous anticyclonic circulation causes (1) an intensification of the North Atlantic Current which reinforces and confines positive temperature and salinity (Fig. 4-15e) anomalies around 40°N; (2) an increase of southward transport in the eastern part of the basin (Fig. 4-16) thus reducing heat and salinity advection into the eastern subpolar gyre, as also shown by Herbaut and Houssais (2009) and Frankignoul et al., (2009). Positive 0-300 m heat content anomalies (Fig. 4-15c) show a northeastward extension up to 55°N in equilibrium with the sea surface height and geostrophic currents (Fig. 4-16), possibly indicating that ocean dynamics plays a role in determining the shape of subsurface temperature anomalies. This northeastward extension is not visible at the surface likely because of atmospheric damping (Masina et al., 2004).

At subpolar latitudes, persistent NAO+ phases cause negative SST anomalies throughout the subpolar gyre without being interrupted, as seen in the interannual response, by anomalies of opposite sign in correspondence of maximum MLD deepening. This might be due to the fact that increased buoyancy losses during persistent NAO+ phases cool subsurface layers more effectively than in the interannual case; thus mixed layer deepening typical of NAO+ phases (Fig. 4-3b) would not entrain to the surface relatively warmer subsurface waters. Sea surface height is lower throughout the subpolar gyre and Labrador Sea, in geostrophic balance with cyclonic circulation anomalies which enhance the strength of the subpolar gyre (Haekkinen and Rhines, 2004; Boening et al., 2006).

Pronounced freshening occurs in the subpolar gyre, in the Labrador Sea and in the eastern mid-latitudes. Whereas on interannual time scales surface salinity mainly responds to local changes in evaporative fluxes and wind-driven currents (Fig. 4-3f and 4-4 right, Visbeck et al., 2003), in response to persistent NAO+ phases low frequency changes in geostrophic ocean advection (Fig. 4-16) appear to be more relevant. In particular, NAO+ forcing is associated with reduced northward salt transport in the eastern subpolar gyre regions by the wind-driven intergyre-gyre (Marshall et al., 2001), and increased southward flows of freshwater related to increased subpolar gyre strength (Fig. 4-16). Similar processes were also detected in observational (Reverdin et al., 1997; Belkin, 2004) and modeling studies (Frankignoul et al., 2009; Herbaut and Houssais, 2009), where it was found that anomalous circulation induced by NAO forcing plays a relevant role in the generation and spreading in successive years of surface salinity anomalies.

By analyzing the in-quadrature ocean response (Fig.4-15, right panels, Fig. 4-16 bottom), it can be seen that positive SST and salinity anomalies generated at mid-latitudes by persistent NAO+ forcing continue to spread northeastward despite the absence of NAO-derived forcing. A similar result was found by Eden and Jung (2001) who explain the SST anomaly evolution as due to delayed convergence of heat transport from anomalous ocean circulation. Also the subpolar gyre exhibits memory of previous persistent NAO+ forcing, especially for subsurface heat content (Fig. 4-15d), sea surface height, and near-surface currents (Fig. 4-16) but less for SST and SSS anomalies which are more affected by atmospheric coupling. The ocean is thus providing significant amounts of memory to the system for several years after a persistent NAO forcing phase. These results also point to the importance of ocean preconditioning in the passage from one NAO decadal cycle to its opposite phase, as found by Lohmann et al. (2009b).
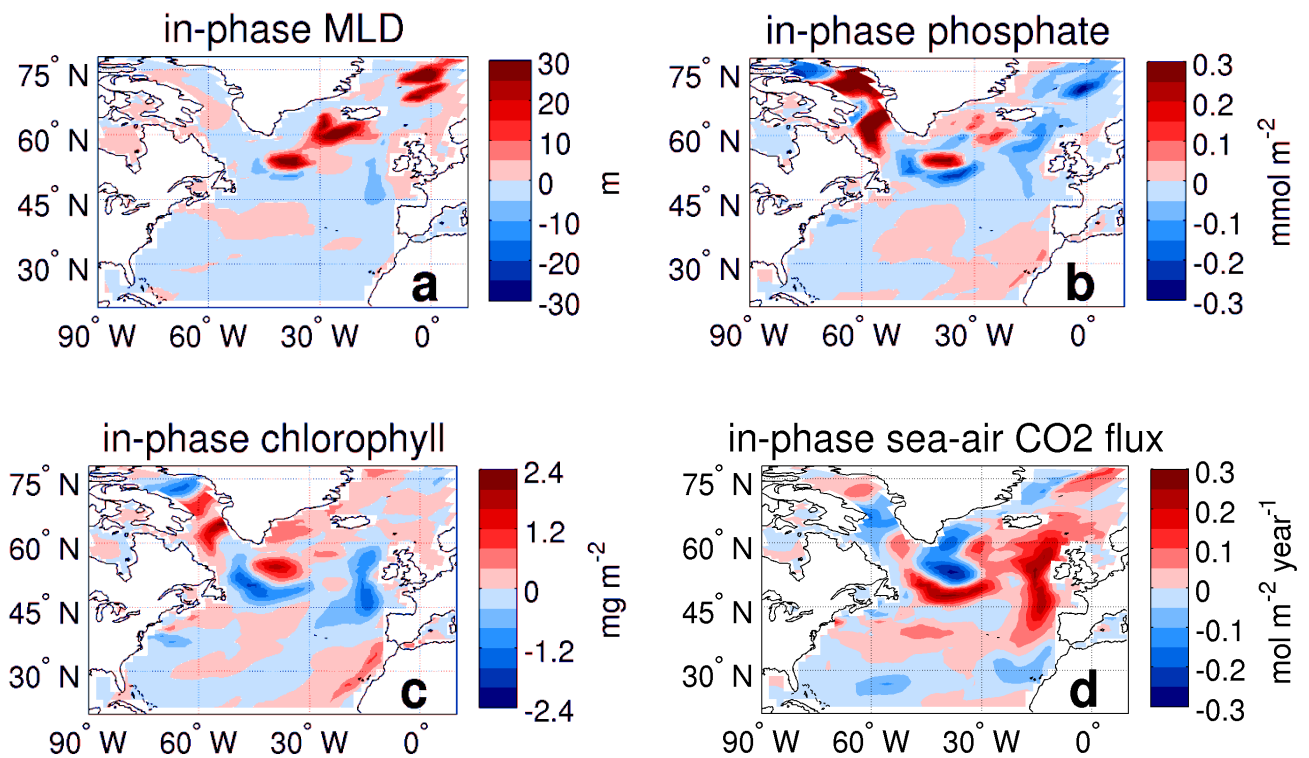
Fig. 4-17 In-phase response to low-frequency NAO+ phases of **(a)** mixed layer depth (m), **(b)** euphotic-depth-integrated phosphate concentration (mmol m^{-2}), **(c)** euphotic-depth-integrated chlorophyll concentration (mg m^{-2}), **(d)** sea-air CO_2 fluxes in mol m^{-2} year^{-1}.

In response to persistent NAO+ forcing, MLD (Fig. 4-17a) deepens in confined areas of the Irminger and GIN Seas, and becomes shallower in the remaining areas of the 45°-60°N belt, contrarily to the interannual response (Fig. 4-3b). We may explain this result

by considering that mixed layer depth variability is determined by upper ocean density modifications which are driven by both temperature and salinity changes. The extensive freshening occurring in the subpolar gyre and in the eastern middle latitudes during persistent NAO+ phases (Fig. 4-15e) enhances stratification in these areas. Thus on decadal time scales persistent changes in salinity acquire more importance, in comparison with surface heat fluxes, in determining MLD variability.

Low-frequency changes in MLD are positively correlated with phosphate (Fig. 4-17b) and chlorophyll concentration anomalies (Fig. 4-17c), indicating that, similarly to the interannual time scale, deeper-than-average MLDs entrain more nutrients to the surface in winter which may be used by phytoplankton in the following spring-summer. Low-frequency changes in MLD are instead negatively correlated with sea-air CO_2 flux anomalies (Fig. 4-17d), indicating that when MLD is deeper the ocean CO_2 uptake increases because of higher primary production and lower sea surface temperatures. It may be seen that in the subpolar gyre, the areas of decreased CO_2 ocean uptake (positive anomalies) are much larger compared to the interannual response. In other words, whereas the interannual response to NAO+ phases causes a large ocean CO_2 absorption at the surface (Fig. 4-5f), on lower frequency the effect that ocean dynamics has on ocean stratification acts to weaken the ocean CO_2 absorbing capacity. This indicates that one cannot extrapolate the biogeochemical response to NAO fluctuations to decadal time scales, as these are affected also by slower time scales set by ocean dynamics.

4.6 Conclusions

The study analyzed the response of the physical and biogeochemical ocean system to North Atlantic Oscillation (NAO) from interannual to decadal time scales. A fully coupled model containing interactive marine biogeochemistry was used to produce a 300-year simulation under constant CO_2. The climate model is found to be capable of internally generating NAO-like variability and of reproducing the main features of the North Atlantic Ocean response to NAO interannual fluctuations through changes in heat, freshwater, and momentum fluxes.

In this modeling study, NAO interannual fluctuations are found to explain a substantial amount of marine biogeochemical variability in the North Atlantic Ocean. Marine biogeochemistry is found to mainly respond to changes in winter mixing, which influences phytoplankton growth through light and limitation mechanisms. Increased winter mixing, occurring during NAO+ in the subpolar gyre and during NAO- at middle latitudes, causes phytoplankton growth to decrease in winter (light limitation) and to increase during the following spring (increased nutrient availability), similarly to what found in the 9-year time series of SeaWiFS satellite estimates. In particular, deeper ocean mixing causes:

1. An amplification of seasonal cycles of phytoplankton, zooplankton, particulate organic matter production, and air-sea CO_2 fluxes.

2. Higher biomasses of phytoplankton and zooplankton on annual scales (10-20% with respect to climatology). In the subpolar gyre this implies increased air-to-sea CO_2 fluxes and particulate organic matter production by phyto- and zooplankton.

The analysis in the coupled model of lagged ocean responses to NAO fluctuations shows that temperature and salinity anomalies persist up to 3 years after their generation, similarly to what found in ocean reanalyses. This behavior suggests an ocean memory of the NAO signal which is further investigated with a low-frequency analysis of the ocean responses. It is found that under persistent positive NAO phases ocean circulation adjusts to the modified wind stress curl field, influencing the ocean temperature and salinity fields as well. This study also shows that ocean anomalies generated on decadal time scales persist also when NAO forcing ceases, re-confirming the capability of the ocean of integrating the atmospheric signal over time. In contrast, in this model simulation ocean marine biogeochemistry has limited memory of NAO

forcing suggesting that its variability is mainly governed by interannual fluctuations of vertical mixing. However, the ocean changes occurring on decadal time scales in response to low-frequency NAO forcing are found in this study to generate some impacts on ocean stratification and marine biogeochemistry as well.

Outlook

This modeling study has found that during positive NAO phases CO_2 air-to-sea fluxes and particulate organic matter (POC) production, a proxy of carbon export from the ocean surface layer, increase by 10-20% in the subpolar gyre (see schematic representation in Fig. 4-18). This behavior is caused by increased wind speeds which enhance mixing, primary productivity, and ocean-atmosphere gas transfer velocity. The combined effect of these two processes (increased CO_2 fluxes and POC production) might lead to an increased uptake of carbon from the North Atlantic Ocean during positive NAO phases. If this is true, an increase of NAO+ phases, suggested as partly caused by anthropogenic CO_2 concentrations (Gillett et al., 2003), may act as a negative feedback to increased anthropogenic CO_2 emissions. How this processes may impact carbon sequestration into deeper ocean layers on longer time scales was not investigated in this study, and constitutes a relevant scientific question to be addressed in future studies.
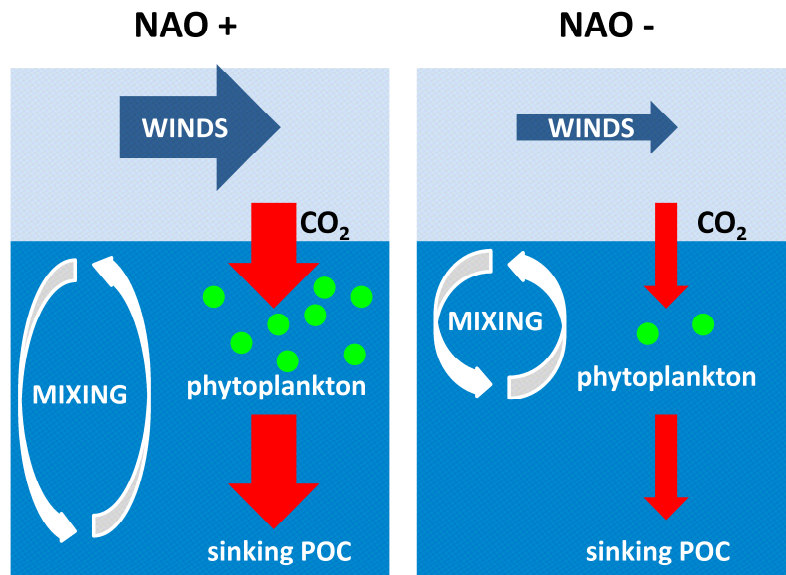
Fig. 4-18 Schematic diagram of the subpolar changes in air-to-sea CO_2 fluxes and production of particulate organic matter (POC) during positive (NAO+) and negative (NAO-) phases. Large arrows indicate large fluxes, small arrows reduced fluxes.

Chapter 5

North Pacific marine biogeochemical variability in XX and XXI century simulations

Summary This study addressed the impacts on North Pacific marine biogeochemistry of natural climatic fluctuations and anthropogenic climate change induced by increased CO_2 emissions. To this end a coupled model containing interactive marine biogeochemistry is used to produce a XX century simulation forced with observed atmospheric greenhouse gas concentrations, and a XXI century simulation forced with the IPCC SRES "business-as-usual" A1B scenario of greenhouse gases increase. It is found that the leading mode of natural atmospheric variability over the North Pacific involves fluctuations of the Aleutian Low strength, whereas the second mode involves a seesaw of atmospheric mass between subtropical and subpolar latitudes. Associated wind changes affect ocean temperature and mixing with impacts on the phytoplankton spring bloom. In particular the first mode of atmospheric variability causes 20-30% chlorophyll changes according to an east-west dipole; the second forces ~10% chlorophyll changes according to a north-south dipole. Comparisons between XX and XXI century simulations show that increased atmospheric CO_2 levels produce sea surface temperatures up to 5°C higher with respect to the XX century, which drastically reduce ocean mixing and its interannual variability in this region. These environmental changes cause a 50% decrease in the subpolar gyre spring phytoplankton bloom and reduced interannual variability on most of the basin; the variance explained by the two dominant modes of atmospheric variability remains nonetheless virtually unchanged in the XX and XXI century. These results show that in a A1B emission scenario, human-induced trends may be considered as the largest source of biogeochemical variation; however natural interannual fluctuations may superimpose to anthropogenic-induced trends and influence the temporal evolution of marine biogeochemical properties.

5.1 Introduction

Observations of biogeochemical and ecological properties in the North Pacific Ocean for the XX century reveal interannual to decadal fluctuations (Miller and Schneider, 2000; Schwing et al., 2010) superimposed to longer term trends (Karl et al., 2001; Watanabe et al., 2005; Ono et al., 2008). Whereas the former have been often found to correlate with climatic indices reflecting large-scale fluctuations in the climate system, the latter have been related to ocean changes due to human carbon emissions in the atmosphere. Separating these two phenomena is made difficult by their intrinsically coupled nature, and by the relatively short observational records of marine biogeochemical properties compared to the temporal scales of decadal and multi-decadal variability.

The leading mode of atmospheric variability in the North Pacific sector is the Pacific–North America (PNA) pattern (Wallace and Gutzler, 1981) which is associated with the modulation of the Aleutian Low, the Asian jet, and the Pacific storm track. Fluctuations in the strength of the winter Aleutian Low pressure system co-vary with the first mode of sea surface temperature variability in the North Pacific, the Pacific Decadal Oscillation (Mantua et al., 1997). The Pacific Decadal Oscillation (hereafter PDO) index exhibits the tendency for multiyear and multidecadal persistence with a few instances of abrupt sign changes, as it occurred in 1976-1977 (Mantua and Hare, 2002; Deser et al., 2006). The temporal evolution of the PDO has been linked to several biological and ecosystem regime shifts in the ocean (Hare and Mantua, 2000; Miller and Schneider, 2000; McFarlane et al., 2000).

Recently a link was also found between low-frequency fluctuations of Northeast Pacific marine biogeochemistry and the second mode of Northeast Pacific sea surface height variability, i.e. the North Pacific Gyre Oscillation (NPGO, Di Lorenzo et al., 2008, 2009), which closely tracks the second mode of North Pacific sea surface temperature variability, i.e. the Victoria mode (Bond et al., 2003). The NPGO is the oceanic expression of the North Pacific Oscillation (NPO) which is identified by fluctuations of the sea level pressure between Hawaii and the Gulf of Alaska (Walker and Bliss, 1932), and co-varies with winter temperature differences between western Alaska-eastern Siberia and western Canada (Rogers, 1981). Since the NPO involves a redistribution of atmospheric mass between subtropical and high latitudes in the North Pacific, it is

suggested to be a basin analog of the North Atlantic Oscillation (Linkin and Nigam, 2008), even though atmospheric teleconnections between the North Pacific and North Atlantic appear to be complex and non-stationary (Zhao and Moore, 2009).

In addition to natural variability cycles, anthropogenic CO_2 emissions are expected to produce significant impacts on North Pacific Ocean properties (Meehl et al., 2007) which in turn may affect marine biogeochemistry mainly through changes in ocean temperatures, mixing and upwelling. Some of these effects have already been detected in the last decades of the XX century. In the subarctic northeast Pacific, Freeland et al., (1997) observed a shoaling of the mixed layer depth in the last 60 years of the XX century in response to upper ocean warming and freshening; however Li et al., (2005) analyzed several stations of the Alaskan Gyre and found a more complex picture of mixed layer depth temporal and spatial responses over the period 1956-2001 owing to various regional forcing factors such as Ekman pumping, heat and freshwater fluxes. Ono et al. (2008) found a decreasing nutrient trend in the period 1975-2005 in the Subarctic North Pacific region between 155°E and 135°W which is significantly correlated with sea surface temperature changes. At the ocean station ALOHA near Hawaii in the subtropical North Pacific subtropical gyre, Karl et al. (2001) have observed changes in nutrient levels, primary productivity, and pigment concentrations in the last three decades of the XX century, suggestive of a shift in the ecosystem structure towards smaller-sized phytoplankton.

Models have also been used to address impacts of both natural fluctuations and of human-induced climate change on North Pacific marine biogeochemistry and ecosystems. A number of modeling studies have shown that climate indices may be correlated with biogeochemical variability in the northeastern Pacific (Chai et al., 2003; Alexander et al., 2008; Di Lorenzo et al., 2008, 2009). By using six different coupled climate model simulations, Sarmiento et al. (2004) suggested that anthropogenic climate warming may cause geographical biomes shifts and decreased nutrient supply in the North Pacific. Hashioka et al. (2009) used an eddy-permitting ecosystem model forced with future climate forcings and found that climate-induced enhancement of ocean stratification may impact the timing and magnitude of the subarctic spring bloom. In addition, Bopp et al. (2005) found in an ocean biogeochemistry model coupled to a climate model, that more nutrient-depleted conditions in the surface ocean may favor

small phytoplankton at the expense of diatoms therefore causing changes in phytoplankton community composition.

In the XX century, North Pacific natural ocean variability and human-induced impacts on sea surface temperatures appear to fall under the same order of magnitude, e.g. 0.5-1°C (Bindoff et al., 2007); however climate projections under increased CO_2 emission scenarios show that future anthropogenic impacts may largely exceed the amplitude of natural fluctuations (Meehl et al., 2007; Wang et al., 2010). A comprehensive investigation of how natural and anthropogenic sources of variability may simultaneously affect the patterns of spatio-temporal variability of North Pacific Ocean is still to be addressed. Earth System Models, in the limits of their biases and coarse resolution, may be used in combination with extended observational efforts, to address this topic in both present and future climate projections.

This study investigates the response of marine biogeochemistry to natural and human-induced climate variability by using an Earth System Model. Two simulations are produced and compared: a historical XX century simulation was performed forced with observed greenhouse gases, aerosol, ozone, and sulfate concentrations and a XXI century climate projection forced with the Intergovernmental Panel on Climate Change (IPCC) A1B emission scenario (Nakicenovic and Swart, 2000). The main scientific questions of this study are:

Scientific questions:

- Which is the response of chlorophyll concentration to climate natural variability in the North Pacific?

- Which are the impacts of increased atmospheric CO_2 levels on chlorophyll structures and on their variability?

This chapter is organized as follows: section 5.2 shows the main features of North Pacific variability simulated by the coupled model; section 5.3 focuses on the bio-physical ocean responses to climate variability in the North Pacific, distinguishing between natural fluctuations and anthropogenic impacts. Finally, section 5.4 gives some concluding remarks.

5.2 North Pacific variability

North Pacific atmospheric variability is investigated by means of Empirical Orthogonal Function (EOF) analysis calculated on January-March (JFM) sea level pressure (hereafter SLP) anomalies in the North Pacific sector (20°-65°N, 120°E-100°W). The spatial patterns of leading modes of sea level pressure variability over the XX century are shown in Fig. 5-1 by regressing JFM anomalies of SLP, winds and wind stress curl, onto the first and second standardized principal component (hereafter PC) time series (Fig. 5-2 a,b). The displayed anomalies in Fig. 5-1 correspond to PC values equal to 1, however it has to be noted that a strong index phase will yield about twice the shown anomalies.

The first mode of sea level pressure variability (52% explained variance in the XX century) is associated with fluctuations in the Aleutian Low strength and position (Fig. 5-1a) and has been shown to be closely related to the North Pacific Index, i.e. the mean SLP anomaly in the Aleutian Low over the Gulf of Alaska (Trenberth and Hurrell, 1994), and to the Pacific North American (PNA) pattern in the troposphere (Wallace et al., 1992), calculated as the normalized 500 hPa height anomalies at 20°N, 160°W and 55°N, 115°W minus those at 45°N, 165°W and 30°N, 85°W (Wallace and Gutzler, 1981). By convention, when the first mode of sea level pressure variability is in its positive polarity, the Aleutian Low is stronger than usual and the wind field exhibits a cyclonic circulation anomaly throughout the North Pacific (Fig. 5-1c). This involves strengthening of westerly winds between 30°-45°N and weakening in the eastern Pacific between 45°-55°N, an increase of high-latitude easterlies, and weakening of subtropical easterlies. Changes in wind patterns in turn affect wind stress curl (Fig. 5-1e), which exhibits overall cyclonic anomalies (around 10% of climatology) north of 40°N (except for coastal domains) and anticyclonic anomalies to the south.
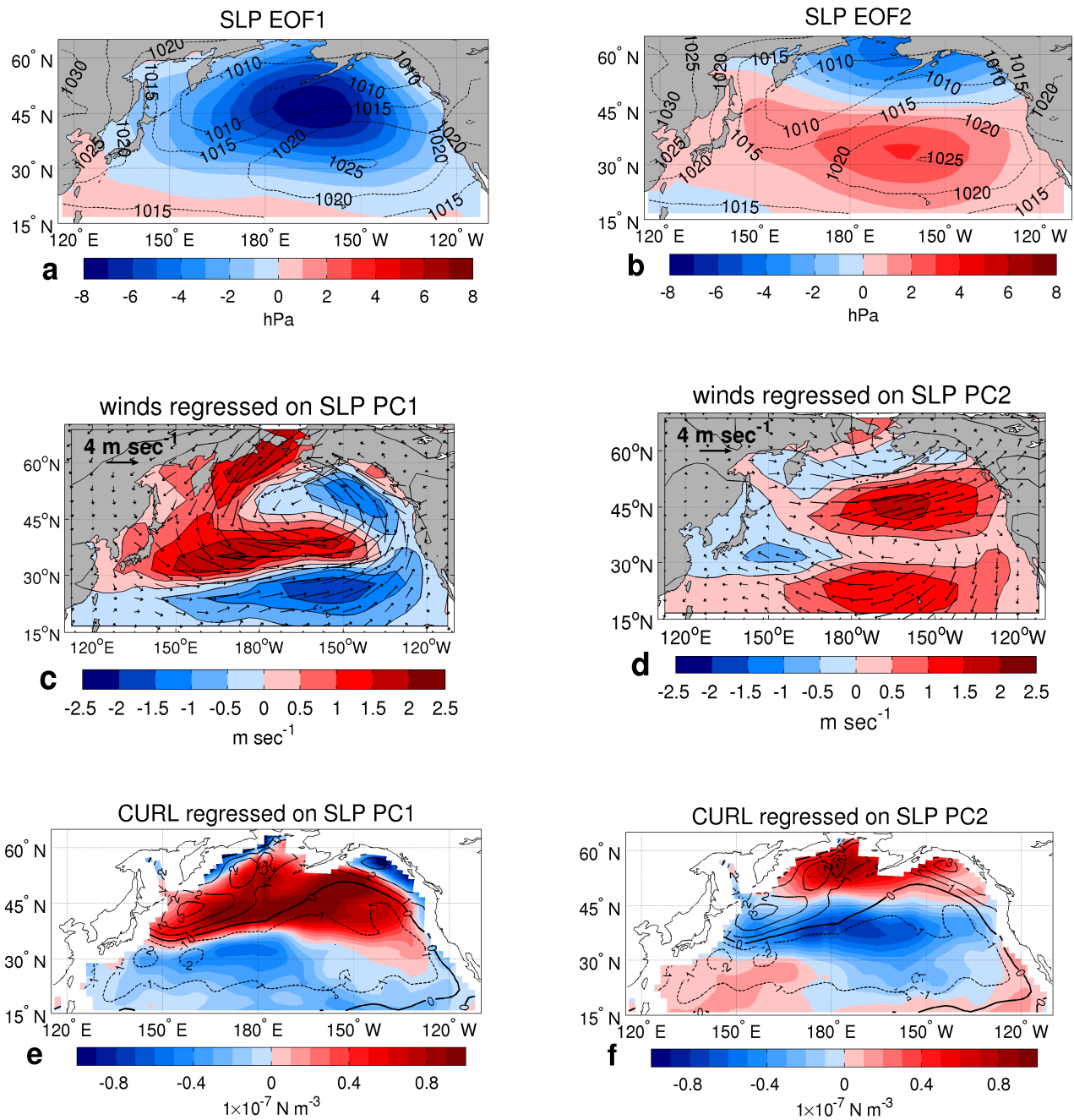
**Fig. 5-1** XX century JFM sea level pressure (hPa) regressed onto the first **(c)** and second **(d)** principle component (PC) time series of JFM SLP anomalies with winter climatology plotted in contours for reference; JFM wind velocity (m sec⁻¹) at 10 m height regressed onto the first **(c)** and second **(d)** PC time series of JFM SLP anomalies; JFM wind stress curl (1×10^{-7} N m⁻³) regressed onto the first **(e)** and second **(f)** PC time series of JFM SLP anomalies. For construction these maps show anomalies relative to index values equal to1.

The second mode of North Pacific JFM SLP variability (22% explained variance in the XX century), corresponding to the North Pacific Oscillation (NPO), involves a north-south dipole characterized by simultaneous out-of-phase fluctuations of atmospheric mass between subtropical and subpolar latitudes (Fig. 5-1b). By convention, positive

polarities of the NPO indicate an enhancement of the north-south SLP difference, which in turn is associated with an intensification and northward shift of mid-latitude westerlies (Fig. 5-1d). The northward shift in westerly winds gives rise to a negative wind stress curl anomaly between 30°-45°N and a positive anomaly north of 50°N (Fig. 5-1f).

EOF analysis is performed also on JFM sea surface temperature (hereafter SST) anomalies over the North Pacific sector (20°-65°N, 120°E-100°W) and the corresponding standardized PC time series of first and second modes of variability computed separately for the XX and XXI centuries are shown in Fig. 5-2 together with winter SLP PC time series. The first mode of SST variability in the North Pacific is the Pacific Decadal Oscillation (PDO, Mantua et al., 1997), whereas the second mode is known as the "Victoria" mode (Bond et al., 2003), which is in turn related to the second mode of Northeast Pacific sea surface height variability, the North Pacific Gyre Oscillation (NPGO, Di Lorenzo et al., 2008). Variability of SLP and SST PC time series show general correspondence, especially in their low frequency temporal evolution (Fig. 5-2, red lines), indicating a relevant atmospheric source for North Pacific SST variability (Schneider and Cornuelle, 2005; Chhak et al., 2009; D'Orgeville and Peltier, 2009). Indeed, Schneider and Cornuelle (2005) show that the PDO pattern and evolution can be reconstructed using an autoregressive model forced by variability of the Aleutian low, El Niño-Southern Oscillation (ENSO) and oceanic circulation anomalies in the Kuroshio-Oyashio Extension region, with changes of the Aleutian low and of ENSO being essential on interannual frequencies. Compared to SLP which exhibits high-frequency fluctuations at interannual time scales, SST variability shows higher energy at decadal frequencies with a spectral peak at ~12 years (not shown), which is slightly lower but still comparatively similar to the observed PDO period (Mantua and Hare, 2002). These longer time scales are possibly related to the integrating effect of the upper ocean mixed layer (Newman et al., 2003), to ocean advective processes, and to the excitation of low frequency off-equatorial Rossby waves (Schneider and Cornuelle, 2005; Power and Colman, 2006; Kwon and Deser, 2007).
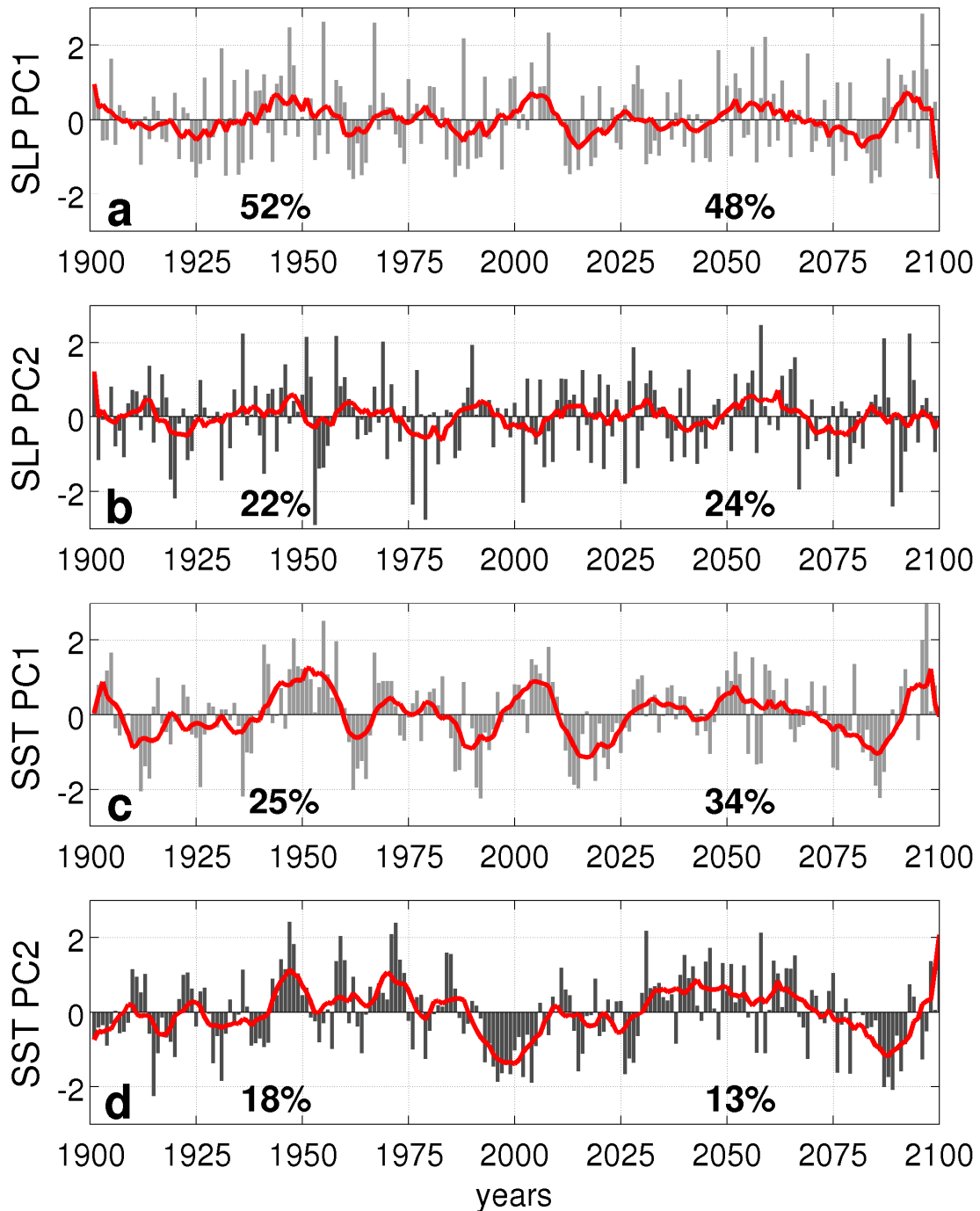
Fig. 5-2 (a) First (PC1, light grey) and **(b)** second (PC2, dark grey) PC time series of JFM SLP anomalies during the XX and XXI centuries (bars). **(c)** First (PC1, light grey) and **(d)** second (PC2, dark grey) PC time series of JFM SST anomalies during the XX and XXI centuries (bars). Red lines indicate 9-year running averages and numbers indicate the variance explained by each mode during the XX and XXI centuries.

By comparing the variance explained by each mode in XX and XXI century simulations (percentages in bottom part of each panel), it may be seen that the variance explained by the first and second SLP modes remains approximately equal (i.e. 2% changes), as similarly found by Keeley et al. (2008). On the other hand, in the XXI century the

variance explained by the PDO exhibits a 10% increase with respect to the XX century, and the variance explained by the second mode of SST variability decreases by 5%. Thus the model indicates that global warming interacts with upper ocean temperature by selecting PDO variability more efficiently than the Victoria mode of SST variability. However the physical link between global climate change and Pacific variability changes is a still topic of scientific debate (Corti et al., 1999; Rauthe et al., 2004).

5.3 Ocean bio-physical response to atmospheric forcing

5.3.1 Natural variability

Ocean physical properties are regressed onto the first and second PC time series of winter SLP anomalies in the XX century. Fig. 5-3 shows the regression coefficients relative to JFM net surface heat fluxes (a,b), SST (c,d) and mixed layer depth (e,f), where for construction the computed anomalies correspond to index values equal to 1. It has to be noted that a high index phase in the model (Fig. 5-2) would produce anomalies that are about twice as large as those shown in Fig. 5-3.

On interannual time scales the ocean adjustment to a deeper-than-average Aleutian Low is characterized by decreased SST (~0.5°C) in the central and western Pacific (Fig. 5-3c). This is related to increased advection of cool and dry air from the north (Fig. 5-1c) and enhanced wind speeds (Fig. 5-1c), which cause an increase of ocean-to-atmosphere net heat fluxes (Fig. 5-3a), and strengthened equatorward temperature advection by Ekman currents (not shown) driven by cyclonic wind stress curl anomalies (Fig. 5-1e). In the eastern part of the basin, weakened winds (Fig. 5-1c) and increased northward ocean circulation (not shown) in relation to cyclonic wind stress curl anomalies (Fig. 5-1e) lead to positive heat flux anomalies and warm anomalies of surface temperature (~0.5°C). Changes in surface heat fluxes and sea surface temperatures drive changes in mixed layer depth (hereafter MLD) which increases by over 60 m in the west and decreases of about the same value in the east (Fig. 5-3e). North of 50°N, increased SST is associated to MLD deepening: this is related to the increase of sea ice melting which leads to an expansion of the ice-free surface able to react to winter heat losses. This result is however partly biased by the model sea ice overestimation in this area during the XX century (Fig 2-7). The pattern of SST regression onto the first mode of SLP variability has very similar structure and magnitude with respect to the simulated PDO

(not shown), confirming the relevant atmospheric source in forcing SST variability on interannual time scales.
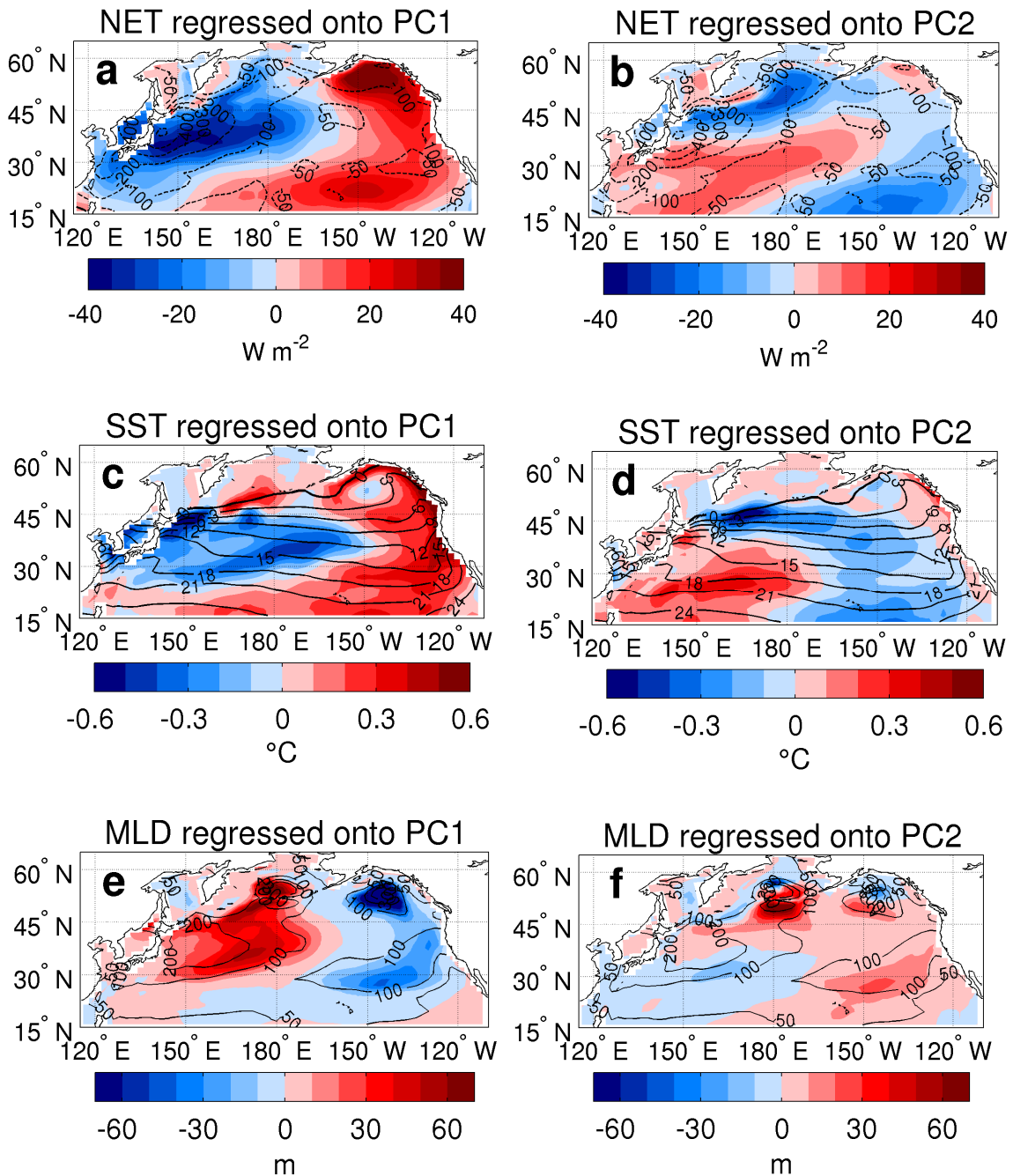
Fig. 5-3 XX century JFM climatologies (contours) and JFM regressions (colors) with the first **(left)** and second **(right)** mode of sea level pressure variability of **(a,b)** net surface heat fluxes (NET) in W m⁻², **(c-d)** sea surface temperature (SST) in °C, **(e-f)** mixed layer depth (MLD) in m.
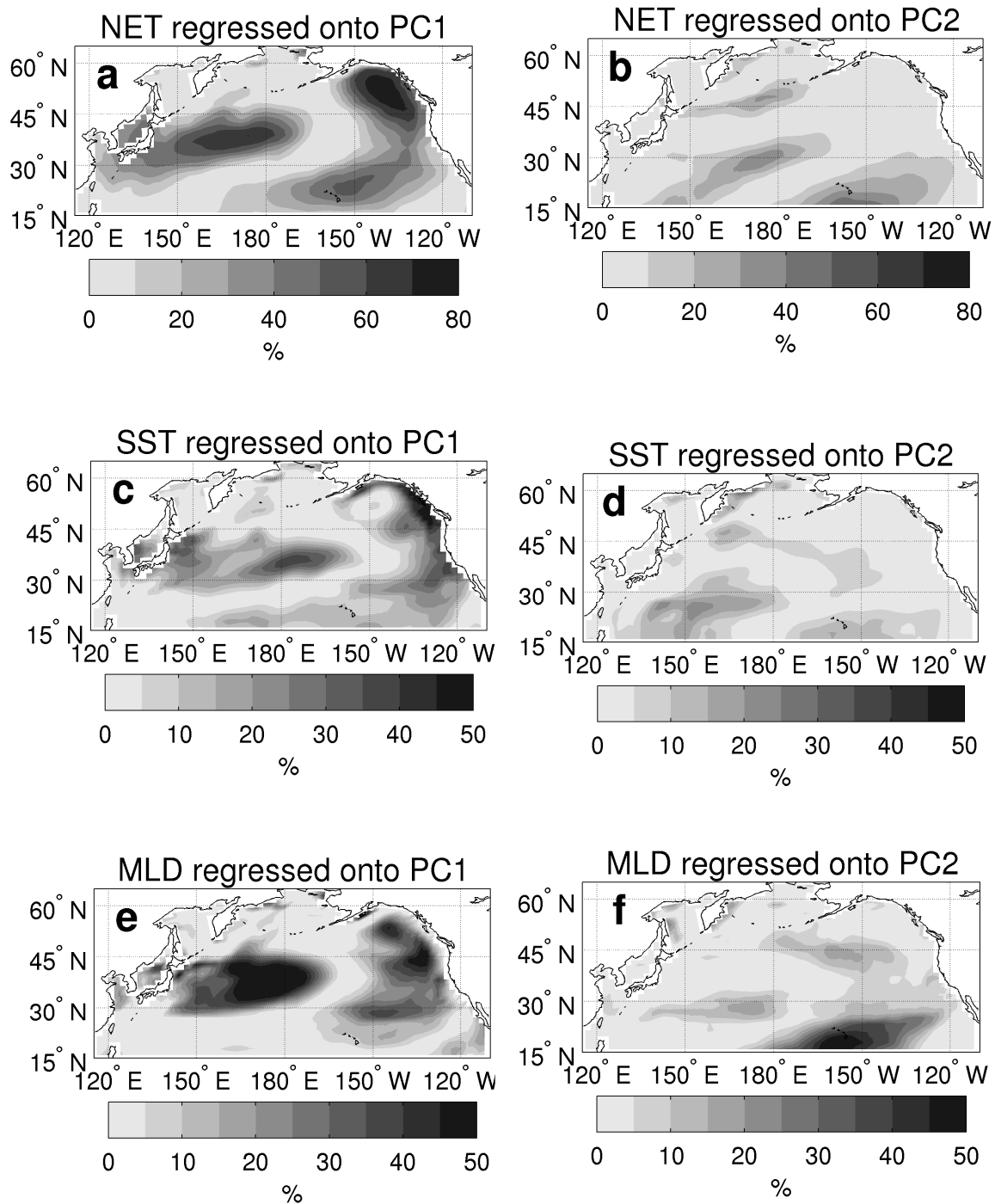
Fig. 5-4 XX century variance explained (%) by the first **(left)** and second **(right)** principle component time series (PC) of sea level pressure variability; **(a,b)** net surface heat fluxes (NET), **(c-d)** sea surface temperature (SST), **(e-f)** mixed layer depth (MLD). Note the different color scale of panels **(a,b)**.

During positive NPO phases changes in wind speed and direction (Fig. 5-1d) are tightly linked to net surface heat flux modifications (Fig. 5-3b). The SST response (Fig. 5-3d) is connected to surface heat flux changes and is characterized by simultaneous decreases at ~45°N (0.6°C) and in the eastern part of the basin (0.2-0.3°C) and increases at ~30°N

in the western part of the basin (~0.3°C). The MLD responds to the modified atmospheric forcing by increasing by more than 30 m at middle and subpolar latitudes except near the coast.

In Fig. 5-4, explained variance of net surface heat fluxes, SST and MLD by the first and second mode of sea level pressure variability is shown in Fig. 5-4. It may be seen that in the central Pacific changes in the Aleutian Low strength are dominant (variance explained >80% for surface heat fluxes, 30-50% for SST and MLD), whereas the NPO explains less ocean variance (10-20%) and in complementary regions with respect to areas of influence of the Aleutian Low.

Similarly to what found in Chapter 4 for the North Atlantic Ocean, chlorophyll interannual variability is tightly linked to winter MLD changes induced by wind fluctuations. Chlorophyll concentration, a proxy of phytoplankton biomass, is integrated throughout the euphotic layer depth and averaged over April-July (AMJJ) when its biomass and variance are largest. Regressions between AMJJ chlorophyll anomalies and the first and second PCs of winter SLP variability are shown in Fig. 5-5 in the XX and XXI centuries together with respective AMJJ chlorophyll climatology, whereas the variance explained by each mode is shown for the XX and XXI century in Fig. 5-6. Regression of chlorophyll AMJJ anomalies onto the SST PC time series yield broadly similar spatial patterns (not shown).

In the XX century, when the winter Aleutian Low is deeper-than-average, the subsequent spring months exhibit an enhanced phytoplankton bloom 20-30% higher than the climatological values simulated in the central part of the basin between 30°-45°N (Fig. 5-5a, colors). This is due to the f deeper mixing (Fig. 5-3e) which entrains more nutrients to the surface in the winter period (not shown). By comparison with AMJJ climatology (Fig. 5-5a, contours) it can be seen that during positive index phases the spring bloom exhibits a southward shift. Along the northwestern edge of the basin, chlorophyll increases by ~10% because of increased ice-free zones. Conversely, the spring bloom is diminished in magnitude by 10-20% in the Alaskan Gyre. The chlorophyll variance explained by changes in the Aleutian Low exceeds 50% over large parts of the central Pacific and Alaskan Gyre (Fig. 5-6a).
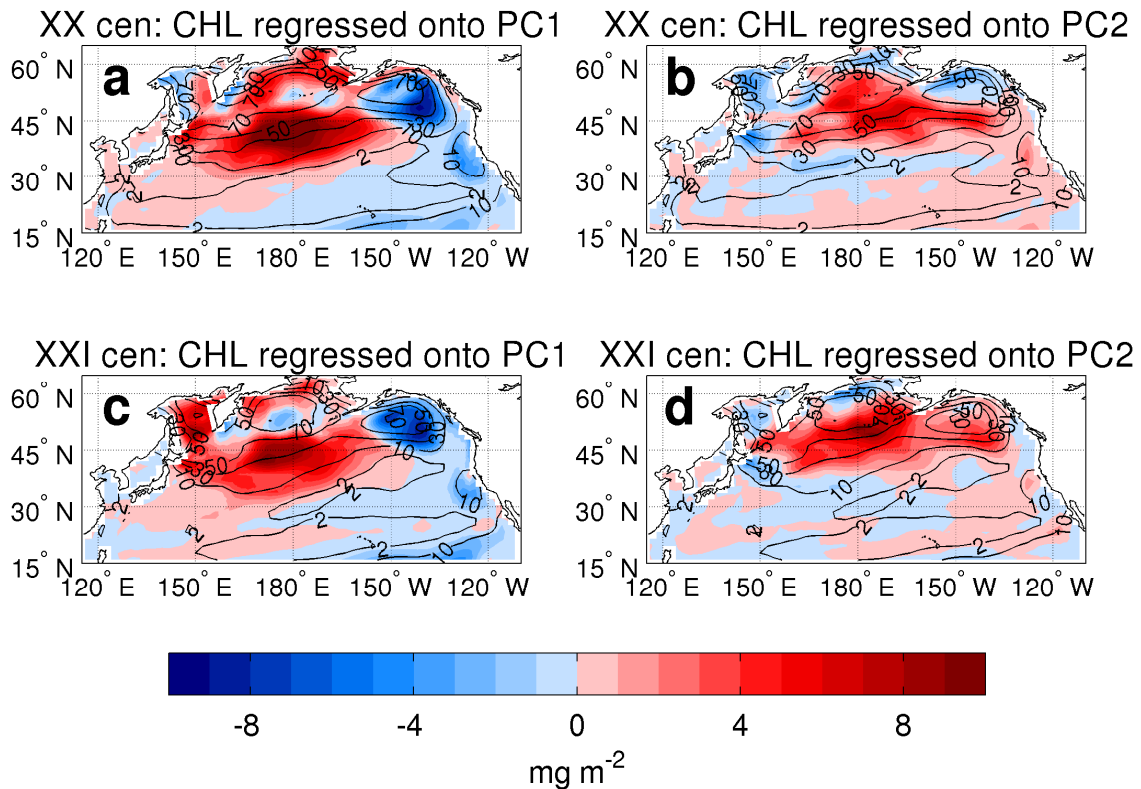
Fig. 5-5 XX century (top) and XXI century (bottom) April-July (AMJJ) euphotic-depth-integrated chlorophyll concentration in mg m^{-2}. Contours: AMJJ climatology; colors: regression onto the **(a)** first and **(b)** second principle component (PC) time series of JFM sea level pressure anomalies.

In the XX century, increased westerlies associated with positive NPO phases lead to deeper winter mixing at subpolar latitudes causing an enhancement of the phytoplankton bloom in the following spring (Fig. 5-5b, colors) because of higher nutrient entrainment into the euphotic layer (not shown). By comparison with climatological values (Fig. 5-5b, contours) it may be seen that chlorophyll concentration is about 10% higher in the open ocean subpolar gyre and that the spatial structure of the spring bloom is not significantly modified. The decrease in chlorophyll along subarctic coastal areas could be biased by the fact that climatological sea ice extent in this model is overestimated (Fig. 2-8). The chlorophyll variance explained by the NPO is ~20% (Fig. 5-6b), i.e. overall lower with respect to Aleutian Low fluctuations; however it is the dominant mode in explaining chlorophyll variance north of 45°N.

In recent modeling studies marine biogeochemical consequences of the North Pacific 1976-1977 regime shift, in which the Pacific Decadal Oscillation entered in a predominantly positive phase (Hare and Mantua, 2000), were investigated by means of physical-biogeochemical ocean models forced with observed atmospheric fields. Chai et al. (2003) find that subsequent to the 1976-1977 climate shift surface nitrate and

chlorophyll concentrations increased by 10-50% in the central North Pacific thanks to a combination of winter mixed layer deepening and upward Ekman pumping enhancement. On the other hand, Alexander et al. (2008) find in the central Alaskan Gyre that enhanced upward Ekman pumping during positive PDO phases causes the halocline and the mixed layer to shoal: this leads to an earlier start of the spring phytoplankton bloom with biomasses ~40% lower because of increased zooplankton grazing pressure. The results found in these forced-ocean studies agree well with the coupled-model results found in the present analysis.

In observational biogeochemical data sets off the Californian coast, Di Lorenzo et al. (2008, 2009) find that nutrient and phytoplankton variability is mainly explained by the NPGO, connected to the second mode climatic variability in the Northeast Pacific, rather than by the PDO. The authors find that relevant physical mechanisms driving biogeochemical variability are wind-driven upwelling and horizontal advection. These processes do not appear to be captured in the present study. However the model appears to successfully capture the large-scale features of chlorophyll variability connected with the second mode of climate variability in the North Pacific when compared with SeaWiFS satellite data (Di Lorenzo et al., in prep. http://eros.eas.gatech.edu/npgo/slides/npgo_ecosys.png).

When computing the same analysis on the XXI century simulation (Fig. 5-5 c,d), it may be seen that global warming does not impact the spatial structures of the chlorophyll anomalies, even though the amplitude and the percentage of variance explained by the first mode of variability is slightly diminished (Fig. 5-6 c,d). It may therefore be concluded that in this coupled simulation the spatial structures and amplitudes associated with atmospheric climatic indexes remain broadly stationary between XX and XXI centuries.
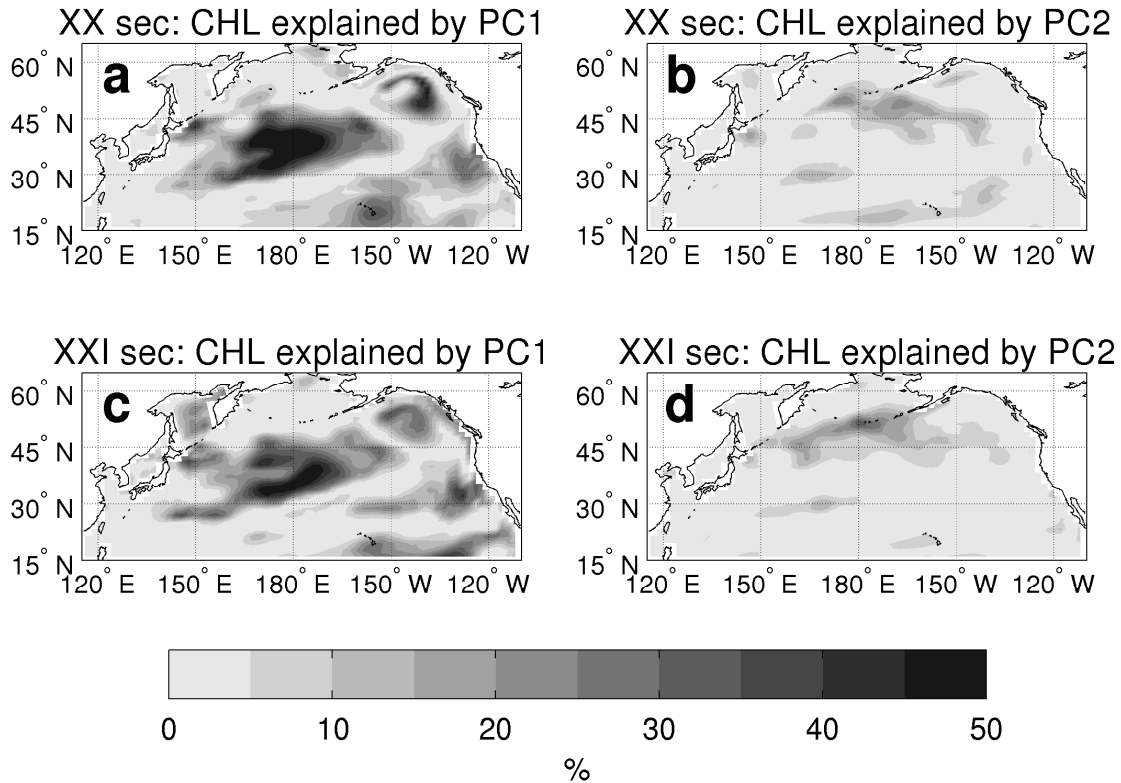
Fig. 5-6 XX century **(top)** and XXI century **(bottom)** April-July (AMJJ) euphotic-depth integrated chlorophyll concentration: variance explained by the **(a,c)** first and **(b,d)** second principle component (PC) time series of JFM sea level pressure anomalies.

5.3.2 Anthropogenic impacts

The physical response to increased atmospheric greenhouse gases is analyzed by taking the differences between the last 30 years of the XXI and XX century (Fig. 5-7). The model simulates an increase in JFM sea surface temperatures (Fig. 5-7a) up to 5°C in the central North Pacific, which is in the range of other coupled model projections for the end of XXI century (Meehl et al., 2007). JFM sea surface salinity (Fig. 5-7b) increases in the central Pacific of 0.2-0.4 because of enhanced evaporation (not shown), whereas it decreases in the eastern portion of the basin in connection with sea ice melting freshwater anomalies being advected by the mean circulation (Fig. 2-5). Associated with surface temperature and salinity changes, the JFM MLD shoals by more than 100 m (~50% with respect to climatology) north of 45°N and slightly deepens (up to 20 m) in the central subtropical gyre; on the northwestern edge of the basin JFM mixed layer increases because of the exposure of formerly sea-ice-covered regions.
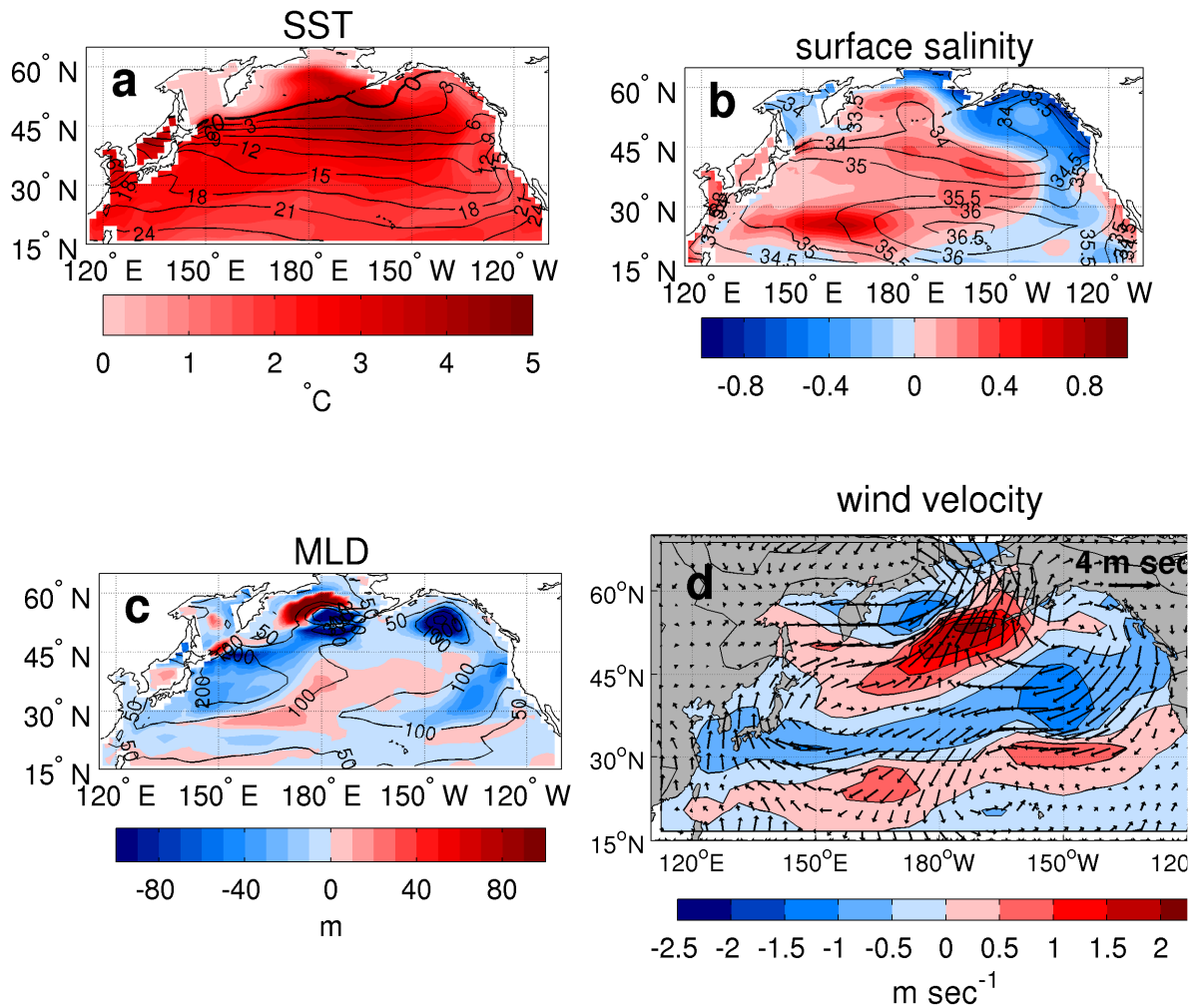
Fig. 5-7 Differences between the last 30 years of the XXI and XX centuries (colors) and climatology of the last 30 years of the XX century (contours) of **(a)** JFM sea surface temperature (SST) in °C, **(b)** JFM sea surface salinity, **(c)** JFM mixed layer depth (MLD) in m, **(d)** JFM winds (arrows) and total wind speed (colors) at 10 m height.

Under increased CO_2 levels, wind patterns show intensification and northward shift of mid-latitude surface westerlies. Other coupled modeling studies have shown an intensification of the mid-latitude westerly jet in XXI century climate models (Ihara and Kushnir, 2009) possibly related to enhanced meridional temperature gradients at the troposphere-stratosphere boundary as proposed by Lorenz and DeWeaver (2007).

When comparing wind variability associated to natural climate oscillations with anthropogenic wind changes (Fig. 5-1c and d), it may be seen that associated wind speed anomalies are of similar magnitude, even though spatial patterns are considerably different. From Fig. 5-7c it may also be seen that MLD modifications in the subpolar gyre are mostly caused by buoyancy changes related to increased temperature and decreased salinity, which would overpower the increased wind speeds at mid-latitudes.

The differences between the last 30 years of the XXI and XX centuries of AMJJ chlorophyll concentration integrated in the euphotic layer are analyzed in terms of median changes (Fig. 5-8a), whose 95% statistical significance is tested through the non-parametric Wilcoxon test (Fig. 5-8b). This test is suitable for non-normally distributed time series, as in the case of chlorophyll concentration time series. The null hypothesis states that two samples come from a distribution with equal medians, and the grey shading shown in Fig. 5-8b indicates the areas where the null hypothesis can be rejected. Spring chlorophyll concentration in the subpolar gyre decreases significantly by ~50% in the XXI century with respect to the XX century, owing to decreased winter nutrient availability caused by increased stratification (Fig. 5-7c). The significant chlorophyll increases along the Siberian coast are related to increased sea ice melting which allows phytoplankton growth in areas formerly covered by sea ice. Slight, although statistical significant, chlorophyll increases occur in the subtropical gyre because of increased mixing, a result which disagrees with the observed trend in the last decade of the XX century (Polovina et al., 2008).

Also the interannual variability of spring euphotic-depth-integrated chlorophyll changes between the last 30 years of the XX and XXI centuries (Fig. 5-8c) with magnitudes of ~10 mg m^{-2}. In order to test the statistical significance of variance changes between the time series, the Ansari-Bradley test is used. The null hypothesis states that the two samples come from the same distribution, against the alternative that they come from distributions that have the same median but different variance. Prior to computing the test, AMJJ chlorophyll values were detrended with their median value in order to obtain two samples with zero-median. Fig. 5-8d shows in grey shading the areas where the null hypothesis can be rejected at 95% confidence level. From figs. 3-8c and 3-8d, it may be seen that the variance of chlorophyll time series significantly decreases in the XXI with respect to the XX century decreases between 30°-45°N, in the Alaskan Gyre, and in the northwestern part of the basin; in an area in the central subpolar gyre chlorophyll variability instead increases, even though not significantly at a 95% confidence level.
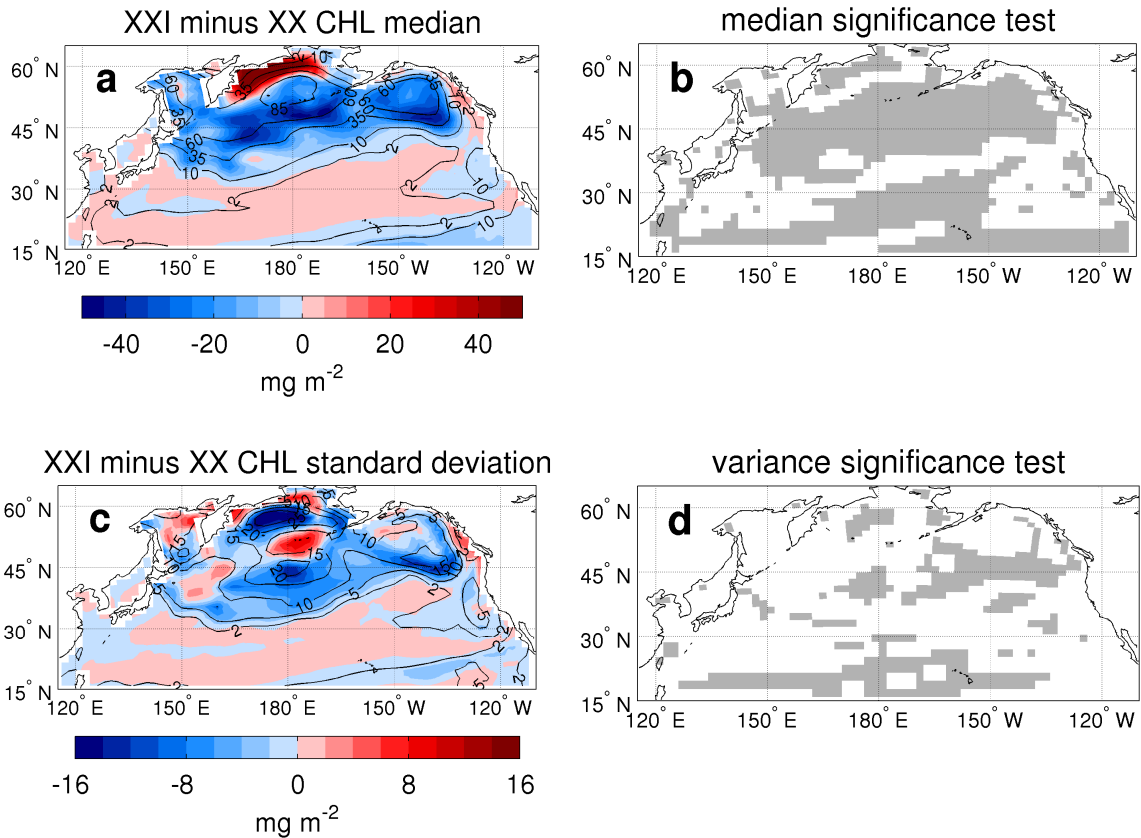
Fig. 5-8 April-July (AMJJ) euphotic-depth-integrated chlorophyll concentration (CHL) in mg m^{-2}. **(a)** Differences between XX and XXI century medians (colors) and XX century median (contours), **(b)** statistical significance at 95% (grey shading) of XX and XXI century median differences; **(c)** differences between XX and XXI century standard deviations (colors) and XX century standard deviation (contours), **(d)** statistical significance at 95% (grey shading) of XX and XXI century standard deviation differences.

Changes in chlorophyll mean state and variability in XX and XXI centuries in connection to changes in the physical climate may clearly be seen on time series averaged over the subpolar North Pacific (45°-60°N, 150°E-130°W) shown in Fig. 5-9, and over the subtropical central North Pacific (20°-45°N, 160°E-130°W) shown in Fig. 5-10. Over the subpolar gyre, JFM SST increases by up to 3°C by the end of the XXI century (Fig. 5-9a), associated with a decrease in JFM MLD (Fig. 5-9b) of several tens of meters. JFM MLD also shows a decrease in interannual variability, possibly caused by increased SST which stabilizes the water column and makes it more difficult for momentum fluxes to erode the ocean mixed layer.

Spring (AMJJ) chlorophyll concentrations are shown both in terms of their integrated values over the euphotic layer depth, to allow comparison with Fig. 5-8, and in terms of their averaged values over the euphotic layer depth, to allow comparison with satellite SeaWiFS chlorophyll estimates shown for the years 1998-2006 with a blue line. As
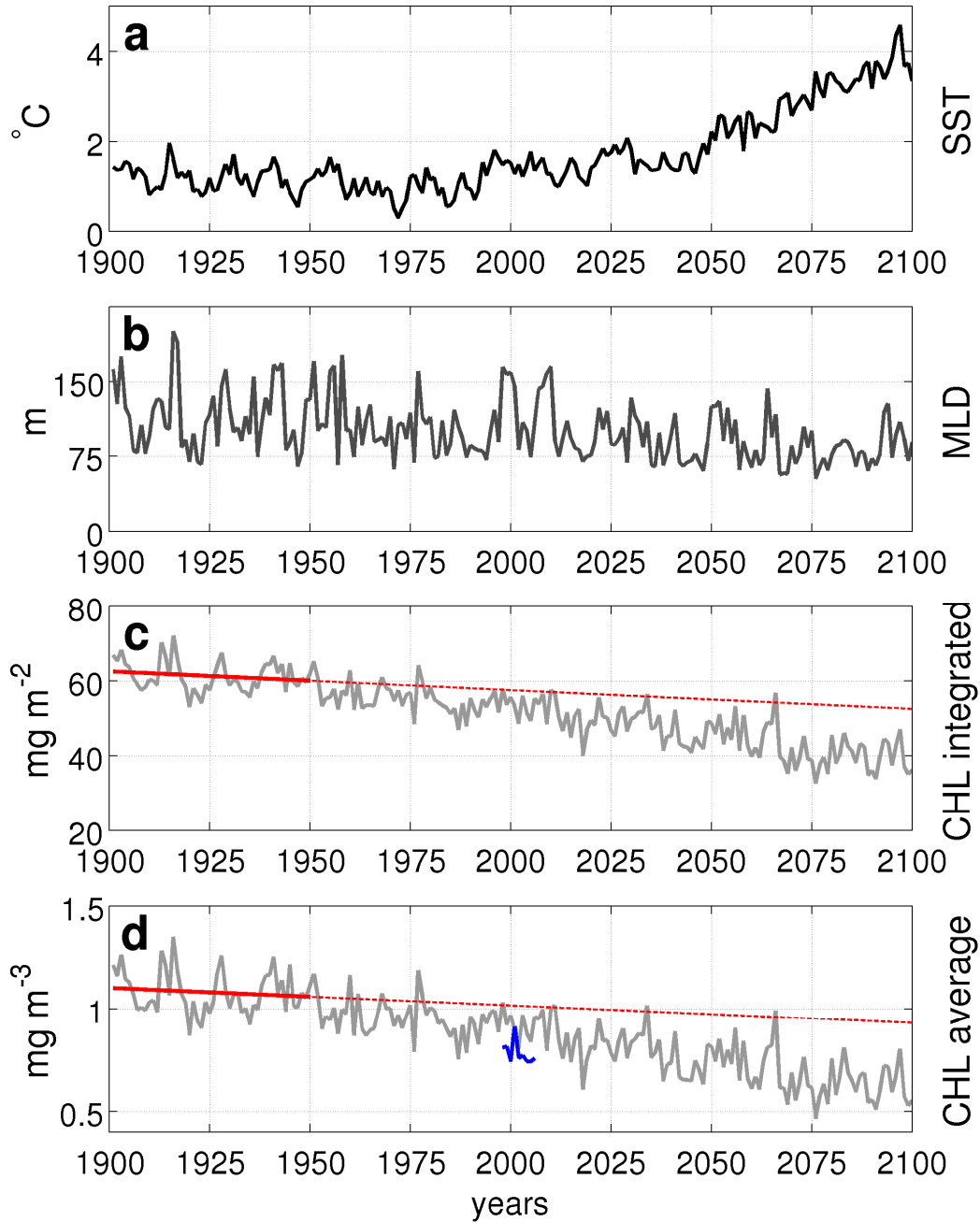
discussed in Section 2.4, the coupled model exhibits a chlorophyll concentration decreasing trend especially in the first 200 years of the simulation which tends to be more stabilized during the following century (Figs 2-12a, Fig. 2-13). Since the first 50 years of the XX century are characterized by relatively small atmospheric CO_2 variations with respect to the subsequent increases of the projected emission scenario (Fig. 2-2), it is here assumed that the chlorophyll decreasing trend shown between years 1900-1949 is mainly due to the model internal drift and not to climate signals. The linear trend over those years is therefore computed (red line) and extrapolated also during the remaining time series. This can give an estimate of the error due to the model drift unrelated with climate forcing. The median difference between the AMJJ chlorophyll during the last 30 years of XX and XXI centuries is ~15 mg m^{-2}. The associated error, estimated by subtracting the means of the linear trends (red line, dashed) of the last 30 years of XX and XXI centuries, is ~5 mg m^{-2}.

From Fig. 5-9d it may be seen that euphotic-depth-averaged chlorophyll concentrations are in the range of SeaWiFS satellite estimates, which are however available only for the years 1998-2006. Even though the time series is extremely short compared to the scales of the Earth system response to the anthropogenic perturbation, a trend is detected towards decreasing chlorophyll values, on which a large interannual fluctuation is superimposed. The similar behavior between model and observations may indicate that the subpolar chlorophyll response to both natural and anthropogenic impacts may be correctly captured by the coupled model simulation.
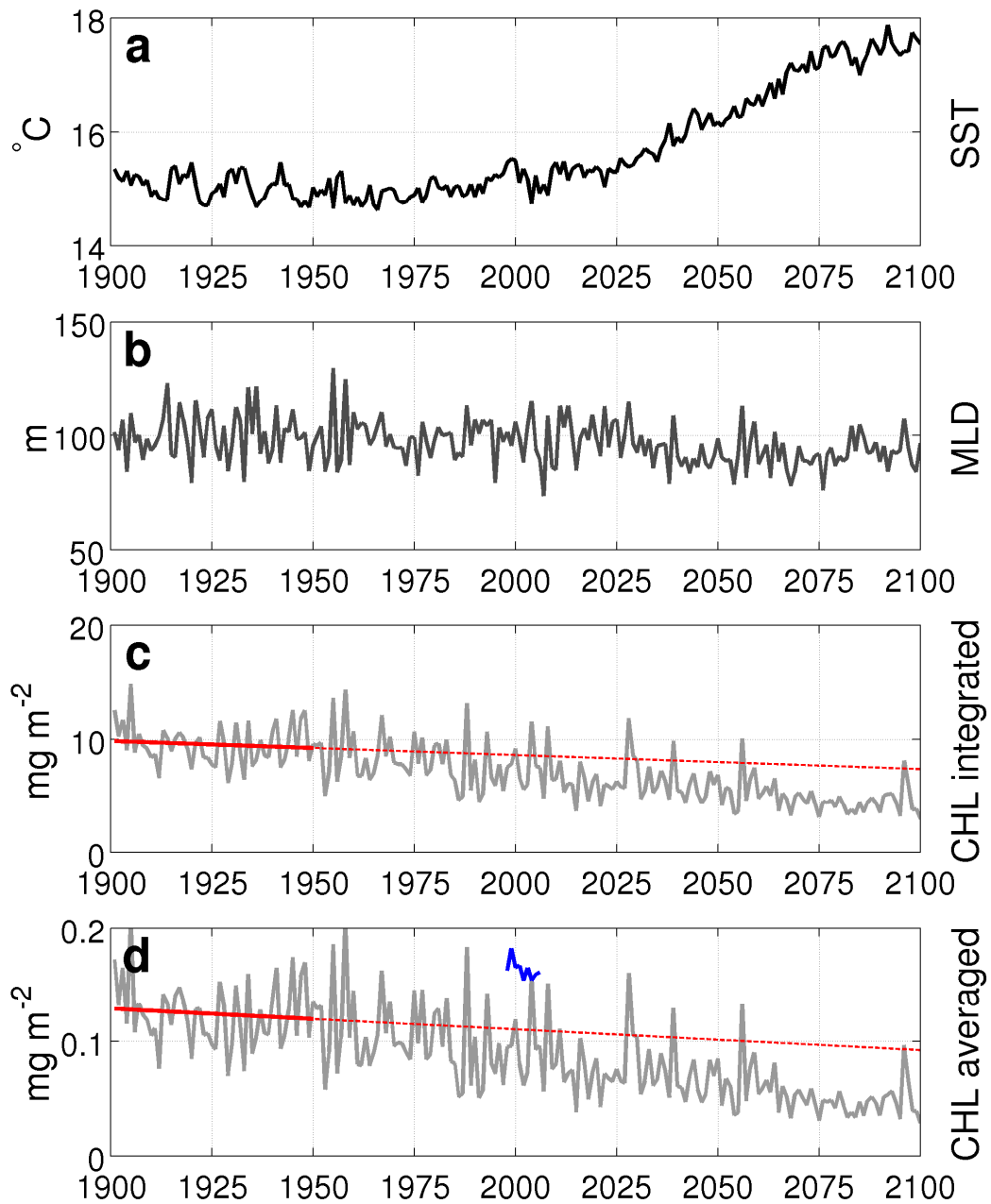
Similar responses occur in the central Pacific (Fig. 5-10): JFM SST increases by ~3°C by the end of the XXI century and JFM MLD decreases slightly in magnitude and largely in variability. As a response to modified physical forcing, chlorophyll decreases by 3.3 mg m^{-2}, with an estimated error related to the systematic trend of 1.2 mg m^{-2}. Hence in the subtropical Pacific the estimated error amounts to a large part of the chlorophyll decrease, and thus could argue that the simulated chlorophyll trend is not climate-related. In addition this area shows a less intense physical forcing in the model, as temperature and salinity are counteracting each other and the MLD changes only slight. Indeed, the main impact of anthropogenic climate change in this area is a drastic reduction of chlorophyll interannual variability, in response decreased mixing variability (Fig. 5-10b). However these considerations have to taken with care as the model in this area underestimates the mean value and overestimates the amplitude of the

interannual oscillations when compared to 1998-2006 satellite SeaWiFS products (Fig. 5-10d).


Fig. 5-9 XX and XXI century time series averaged in the subpolar North Pacific (45°-60°N, 150°E-130°W), of **(a)** sea surface temperature (SST) in °C, **(b)** mixed layer depth (MLD) in m, **(c)** euphotic-depth-integrated chlorophyll concentration (CHL) concentration in mg m^{-2} (grey), **(d)** euphotic-depth-averaged chlorophyll concentration (CHL) in mg m^{-3} (grey) and chlorophyll estimated from SeaWiFS satellite data for the years 1998-2006 (blue). In panels **(c)** and **(d)**, the linear trend relative to the years 1900-1949 is shown (red full line) and extended for reference also in remaining part of the time series (red dashed line).

Fig. 5-10 XX and XXI century time series averaged in the central North Pacific (20°-45°N, 160°E-130°W), of **(a)** sea surface temperature (SST) in °C, **(b)** mixed layer depth (MLD) in m, **(c)** euphotic-depth-integrated chlorophyll concentration (CHL) concentration in mg m^{-2} (grey), **(d)** euphotic-depth-averaged chlorophyll concentration (CHL) in mg m^{-3} (grey) and chlorophyll estimated from SeaWiFS satellite data for the years 1998-2006 (blue). In panels **(c)** and **(d)**, the linear trend relative to the years 1900-1949 is shown (red full line) and extended for reference also in remaining part of the time series (red dashed line).

Changes in climatological seasonal cycles during the last 30 years of the XX and XXI centuries are shown in Fig. 5-11. Both at subpolar and at subtropical latitudes, increased SSTs and stratification in the XXI century lead to a drastic reduction of the spring phytoplankton maximum (>50%) and to an earlier starting of the winter bloom period in the order of one month. These effects arise because of a combination of increased light

availability in winter, and decreased nutrient supply in the following months and possibly increased zooplankton grazing pressure during the following spring months.
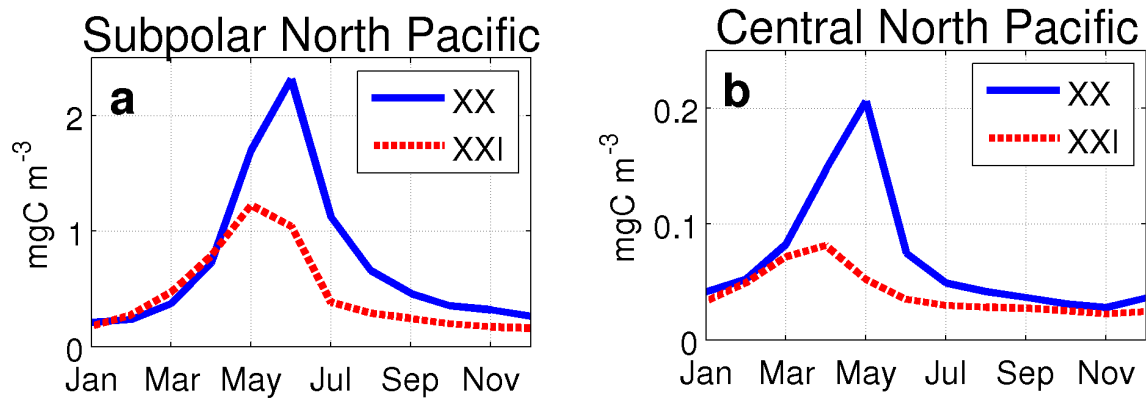
Fig. 5-11 Climatological seasonal cycles of euphotic-depth-averaged chlorophyll concentration computed over the last 30 years of XX century (blue line) and of the XXI century (red dashed line) over **(left)** the subpolar North Pacific (45°-60°N, 150°E-130°W) and **(right)** over the central North Pacific (20°-45°N, 160°E-140°W).

When comparing the magnitude of the chlorophyll anomalies induced by natural variability (Section 5.3.1) and by global warming trends, we can make the following considerations: (1) Interannual chlorophyll fluctuations range between 4-10 mg m^{-2} when the PC index value is equal to 1; (2) a strong event having index values around 2 (Fig. 5-2) will generate chlorophyll anomalies about twice as high (~8-20 mg m^{-2}); (3) chlorophyll changes induced by global warming range between 20-40 mg m^{-2}. Thus interannual fluctuations are lower and on average represent 10% to 50% of projected global warming impacts predicted by this model. However strong interannual wind fluctuations produce chlorophyll anomalies which fall in the range of those projected to occur in an anthropogenic A1B emission scenario. This behavior can also be seen in the time series shown in Figs. 5-8 and 5-9, where decadal variations due to natural oscillations may in cause amplification or weakening of the anthropogenic signal. This study shows that care must thus be taken in attributing chlorophyll trends computed on short periods to anthropogenic impacts.

5.4 Conclusions

This study addressed the impacts on North Pacific marine biogeochemistry of natural climatic fluctuations and anthropogenic climate change induced by increased CO_2 emissions. To this end a coupled model containing interactive marine biogeochemistry is used to produce a XX century simulation forced with observed atmospheric greenhouse gas concentrations, and a XXI century simulation forced with the IPCC SRES A1B scenario of greenhouse gases increase.

The dominant modes of winter climate variability in both the XX and XXI centuries are found to be related with (1) fluctuations of the Aleutian Low strength and (2) with a redistribution of atmospheric mass between subtropical and subpolar latitudes, referred to as the North Pacific Oscillation. Associated variations in wind speed and direction modify ocean temperatures and mixing through changes in surface heat fluxes. These climate fluctuations are found to explain a large part of the variability of phytoplankton spring blooms. In particular, when the Aleutian Low is strong, spring chlorophyll increases by 20-30% in the central Pacific and decreases in the Alaskan Gyre. When subpolar-subtropical pressure gradients are strong, chlorophyll is enhanced by ~10% at subpolar latitudes.

In the coupled model, increased greenhouse gases in the XXI century raise sea surface temperatures by up to 5°C in the subpolar North Pacific, with a consequent enhancement of stratification by up to 50%. This has significant impacts on the North Pacific phytoplankton spring bloom, which at the end of the XXI century is shifted one month earlier and with magnitudes 50% lower than in the XX century. Moreover, increased upper-ocean temperatures significantly reduce the magnitude chlorophyll interannual fluctuations on large portions of the North Pacific. This study however also shows that the variances explained by the first and second modes of atmospheric variability, and their impact on the chlorophyll spring bloom, do not substantially change between XX and XXI centuries.

Concluding, human-induced impacts on the physical environment are the largest source of marine biogeochemical variation, with natural climate fluctuations amounting on average to 10-50% of the human-induced changes. However it has to be remarked that strong interannual wind fluctuations may produce chlorophyll anomalies which fall in the range of those projected to occur in an anthropogenic A1B emission scenario. This

result shows that care must thus be taken when attributing chlorophyll trends computed on short time series to anthropogenic climate change.

This PhD thesis advances the knowledge of bio-physical interactions within the global climate, highlighting the intrinsic coupling between physical climate and biosphere, and providing a framework on which future studies of Earth System change can be built on.

Chapter 6

Conclusions

In this PhD thesis I focused on the study of two-way interactions between climate and marine biogeochemistry in a global climate model. Within the vast range of bio-physical interactions occurring within the Earth System, I analyzed some particular aspects which are believed to be relevant in understanding the Earth's climate functioning and its temporal evolution. These are (1) the climate feedbacks of the solar radiation absorption by phytoplankton, (2) the physical and biogeochemical ocean responses to the North Atlantic Oscillation, and (3) the response of marine biogeochemistry to natural climate fluctuations and to anthropogenic climate forcing in the North Pacific Ocean.

Prior to addressing these studies, I assessed whether the coupled model had sufficient skill at simulating the salient features of the present climate state. Coupled climate models are powerful tools for simulating the interactive evolution of the atmosphere-ocean-sea ice system, yet they are affected by errors that may hinder a correct representation of natural processes. I devoted a part of Chapter 2 to a comparative analysis of the model skills and errors with available observational data sets. The climate model was found to capture the prominent characteristics of the large-scale atmospheric, oceanic, and marine biogeochemical properties, and this has motivated me in continuing my analysis of interactions between climate and marine biogeochemistry. Modeling results obtained throughout the thesis have however been interpreted and discussed in consideration of the errors of the coupled model.

In Chapter 3, I addressed the scientific question of whether phytoplankton organisms, which are ubiquitous in the global ocean, are capable of affecting the physical climate in the process of absorbing solar radiation for their photosynthetic reactions. In fact this process heats the surrounding environment and modifies the radiative and thermal budget of the upper ocean. Such bio-optical feedbacks may be relevant for global climate, as phytoplankton organisms are virtually ubiquitous and dwell in the upper ocean layers in strong contact with the atmosphere.

To address the role of biological radiative heating onto the global climate, I performed and compared two fully coupled simulations: one containing both physical and biological components of the coupled model, the other containing only the physical components. The model results show that phytoplankton warms the ocean surface and raises sea surface temperatures of about 0.5°C. This triggers various dynamically coupled oceanic and atmospheric responses involving changes in stratification, wind patterns, precipitation, incoming solar radiation, and ocean circulation. In addition, increased evaporative heat fluxes from the ocean surface result in an increase of atmospheric water vapor. This process exerts a positive feedback onto global temperatures and suggests that marine biogeochemistry may contribute to a small part of the Earth's greenhouse effect.

This analysis showed that phytoplankton may indeed give rise to a climatic effect by means of its capability of absorbing solar radiation. Bio-optical feedbacks may therefore interact with other sources of climate variability, such as natural climate fluctuations and anthropogenic climate change. It is instructive to compare the magnitude of bio-optical feedbacks with natural and anthropogenic climate variations, which I addressed in Chapters 4 and 5. Impacts of anthropogenic warming, as simulated under the A1B scenario, are the largest source of oceanic variation, whereas impacts of natural fluctuations and of bio-optical feedbacks are about an order of magnitude smaller. This comparative analysis of different climatic perturbations may be useful in deciding whether to add the marine biogeochemistry compartment to climate model simulations in order for bio-optical feedbacks to be explicitly represented.

In Chapters 4 and 5 I focused on the study the climate forcing of on marine biogeochemistry. In particular I analyzed effects of the primary modes of atmospheric variability on the North Atlantic (Chapter 4) and in the North Pacific (Chapter 5), and the impacts of the anthropogenic emission scenario A1B of the IPCC for the 21st century (Chapter 5). I focused on the northern hemisphere – rather than on the southern hemisphere - because there a larger quantity of observational data is available for the assessment of model results. I extrapolated the modes of atmospheric variability of the simulated climate by means of Empirical Orthogonal Function analysis on winter sea level pressure fields, and the response to the climatic fluctuations was investigated mainly through regression analysis on the obtained principal component time series.

The physical and biogeochemical ocean responses to the North Atlantic Oscillation (NAO) were analyzed on the 200-year simulation performed with the fully coupled model under constant greenhouse gases typical of present climate conditions ($CO_2 = 348$ ppm). When compared to observational data sets, the climate model was found to be capable of internally generating NAO-like variability and of reproducing the main features of the North Atlantic Ocean response to NAO interannual fluctuations. The North Atlantic Oscillation involves a north-south redistribution of atmospheric mass and is linked, though changes in the wind field, to coherent out-of-phase sea surface temperature changes between middle and subpolar latitudes. The marine biogeochemistry responses to NAO fluctuations were consequently assessed. Marine biogeochemistry is found to mainly respond to NAO-induced changes in winter mixing, which influence the phytoplankton growth through light and limitation mechanisms. An increase in winter mixing in the subpolar gyre (positive index phase) causes on annual average increased values of phytoplankton, zooplankton, particulate organic matter production, and air-sea CO_2 fluxes of 10-20% with respect to climatology. A possible future direction of this study would be assessing the effective carbon sequestration changes related to the NAO in the North Atlantic, which is one of the largest carbon sinks in the northern hemisphere.

An aspect I wished to investigate was whether in the coupled model the ocean system (physical and biogeochemical) was capable of keeping memory of meteorological forcing in years subsequent to an NAO event. I therefore analyzed the lagged correlations between NAO index and ocean time series and found that temperature anomalies persist up to 3 years after their generation, similarly to what found in ocean reanalyses. Moreover they appear to propagate from their source region in successive years apparently following major current systems. In contrast, marine biogeochemistry had limited memory of interannual NAO forcing which brought me to hypothesize that in this model biogeochemical variability was mainly governed by interannual fluctuations of vertical mixing having very short decorrelation time scales. The behavior of the ocean physics instead suggested a memory of the interannual NAO signal which I therefore further investigated with a low-frequency analysis of the ocean responses. It is found, in agreement with previous modeling and observational studies, that under a low-frequency persistency of NAO phases, ocean circulation adjusts to the modified wind stress curl field, influencing the ocean temperature, salinity, and mixing, and marine

biogeochemistry as well. Finally, this study also shows that ocean anomalies generated on decadal time scales persist also when NAO forcing ceases, re-confirming the capability of the ocean of integrating the atmospheric signal over time.

Having detected in the North Atlantic a multitude of physical and biogeochemical ocean responses to physical climate forcing, I next turned in Chapter 5 to investigating biogeochemical variability in the North Pacific Ocean in present climate and a future scenario of anthropogenic emissions. To this end I used another set of centennial simulations performed within the ENSEMBLES project in which global climate was forced by historical measurements and the A1B future projection of atmospheric radiatively-active gases. My aim was investigating how responses of marine biogeochemistry to natural and anthropogenic forcings were comparatively different in terms of magnitude and spatial structures. To my knowledge this topic has not been addressed in previous coupled modeling studies; yet it is an important one, as in the short available observational time series it is not always clear whether the observed changes are due to anthropogenic forcing or to natural variability cycles.

The two dominant modes of winter atmospheric variability in the 20th and 21st centuries are involve fluctuations of the sea level pressure fields according to a specific spatial structure. The first mode, explaining the largest atmospheric variance in winter, involves fluctuations of the Aleutian Low strength and has its oceanic counterpart in the well-known Pacific Decadal Oscillation. The second mode involves a redistribution of atmospheric mass between subtropical and subpolar latitudes, similarly to the NAO, and has also recently been found to have distinctive oceanic responses. Associated wind changes affect ocean temperature and mixing with impacts on the phytoplankton spring bloom. In particular the first mode of atmospheric variability causes 20-30% chlorophyll changes according to an east-west dipole; the second forces ~10% chlorophyll changes according to a north-south dipole.

The impact on marine biogeochemistry of increased atmospheric greenhouse gases in a projected future climate was subsequently analyzed. The model simulation shows that increased atmospheric CO_2 levels produce in the North Pacific sea surface temperatures up to 5°C higher with respect to the 20th century, which substantially reduce ocean mixing and its interannual variability. These environmental changes cause a statistically-significant 50% decrease in the subpolar gyre spring phytoplankton bloom and reduced chlorophyll interannual variability on most of the basin; the variance

explained by the two dominant modes of atmospheric variability remains nonetheless virtually unchanged in the 20th and 21st century.

These results suggest that in the North Pacific human-induced impacts on the physical environment are the largest source of marine biogeochemical variation, whereas natural climate fluctuations amount on average to 10-50% of the human-induced changes. However it has to be remarked that higher-than-average climatic fluctuations may produce chlorophyll anomalies which fall in the range of those projected to occur in an anthropogenic A1B emission scenario. I therefore concluded that care must thus be taken when attributing to anthropogenic climate change the chlorophyll trends extracted from short-term time series, as they could instead originate from natural climate fluctuations.

Acknowledgements

List of figures

Chapter 1

Chapter 2

Fig. 2-11 Observed (blue, dashed line) and simulated (red, full line) climatological seasonal cycles, computed over the subpolar North Atlantic. **Left**: mixed layer depth (MLD) in m, where the observed values are from de Boyer Montégut et al. (2004). **Right**: chlorophyll concentration (Ch-SAT) in mg m^{-3}, where observed values are SeaWiFS satellite estimates (McClain, 2009), and simulated values are vertically averaged until the 3rd optical depth.

Fig. 2-12: Time series of annual chlorophyll (CHL) concentration integrated in the euphotic layer (mg m^{-2}) and averaged north of 35°N. **(a)** B experiment CHL time series (black) and second order polynomial fit (red) over the last 200 years of simulation, **(b)** last 200 years of the B experiment CHL anomalies after detrending.

Fig. 2-13 Time series of annual chlorophyll concentration integrated over the euphotic layer depth and averaged over the global ocean (mg m^{-2}) for the pre-industrial simulation (blue), historical simulation from 1860 to 1999 (green), and A1B scenario for the XXI century (red).

Fig. 2-14 Maps of 2x2 degrees binned data of surface pCO$_2$ (µatm) from **(a)** LDEO dataset (Takahashi et al., 2009), **(b)** annual climatology of the last 30 years of the XX century simulation. From Vichi et al., 2010 (in preparation).

Chapter 3

Fig. 3-1: **(a)** B minus A annual mean differences of attenuation depth (m) integrated throughout the euphotic layer depth; **(b)** B experiment biological heating at the surface (°C month^{-1})

Fig. 3-2: B minus A annual mean differences of **(a)** sea surface temperature (SST) in °C, **(b)** mixed layer depth (MLD), indicated as the percentual change with respect to the A experiment,**(c)** 0-300 m integrated heat content (HC) in J m^{-2}, **(d)** precipitation (PREC), in mm day^{-1}, **(e)** solar radiation at the ocean surface (W m^{-2}) and **(f)** ocean-atmosphere latent heat fluxes (W m^{-2}), where positive heat fluxes indicate an ocean heat gain.

Fig. 3-3 Statistical significance at a 99% confidence interval of B minus A annual mean differences of (a) sea surface temperature (SST), (b) mixed layer depth (MLD), (c) 0-300 m integrated heat content (HC), (d) sea level pressure (SLP).

Fig. 3-4: B minus A annual differences of wind velocities in m sec^{-1} at 1000 mbar (arrows) and associated wind stress curl in N m^{-3} (colors).

Fig. 3-5: B minus A annual differences of sea level pressure (hPa) and A annual climatology in contours. Shading intervals are 0.05 hPa and contour intervals 5 hPa.

Fig. 3-6 B minus A annual differences of surface currents (cm sec^{-1}). Note different scaling for velocity differences >0.45 cm sec^{-1} (depicted in red), velocities included between 0.15 and 0.45 cm sec^{-1} (depicted in blue), and lower than 0.15 cm sec^{-1} (depicted in black).

Fig. 3-7 Zonal averages of **(a)** B minus A (colors) and A (contours) atmospheric temperature (°C) plotted as a function of atmospheric pressure, **(b)** B minus A (colors, %) and A (contours, kg/kg×10^{-3}) water vapor plotted as function of atmospheric pressure, **(c)** B minus A surface heat fluxes (W m^{-2}) distinguished between solar (red), latent (blue), sensible (green), and longwave (grey), where positive values indicate an ocean heat gain, **(d)** B minus A (colors) and A (contours) ocean temperature (°C) plotted until 300 m depth.

Fig. 3-8: Annual means of B minus A surface heating terms (°C month^{-1}) due to **(a)** radiative processes and **(c)** advective processes (sum of zonal, meridional and vertical components). Note the different color scales.

Fig. 3-9 Zonal section in the Equatorial Pacific of atmospheric zonal velocities (m sec^{-1}) averaged between 5°S-5°N and plotted as a function of atmospheric pressure (hPa). Colors: B minus A, contours: A. Positive values correspond to eastward motion.

Fig. 3-10: Meridional sections in the central Pacific of B minus A **(a)** vertical atmospheric velocity (hPa day^{-1}) and **(b)** meridional atmospheric velocity (m sec^{-1}). Quantities are zonally averaged between 145°E and 100°W. Positive values indicate downward **(a)** and northward **(b)** motion.

Fig. 3-11: Equatorial Pacific map of B minus A **(a)** ocean vertical velocity (cm day^{-1}) averaged over the first 50 m depth, where positive values indicate upward motion, and **(b)** meridional ocean velocity (cm sec^{-1}) at 50 m depth, where positive values indicate northward motion.

Fig. 3-12 Zonal sections in the equatorial Pacific (2°S-2N average) of **(a)** B minus A ocean temperatures in °C (colors) and thermocline depth (full line: A experiment, dashed line: B experiment), **(b)** B minus A radiative heating differences in °C month^{-1} (colors) and chlorophyll concentration in mg m^{-3} (contours), **(c)** B minus A (colors) and A (contours) zonal current velocities in cm sec^{-1}. Note the different depth scale of panel **(b)**.

Fig. 3-13 Atmospheric zonal velocities (m sec^{-1}) zonally averaged over the globe. Colors: B minus A differences; contours: A experiment.

Fig. 3-14 B minus A surface current velocities in cm sec^{-1} (arrows) and sea surface height in cm (colors) in the **(a)** North Atlantic and **(b)** North Pacific. Note the different color and arrow scales between the two panels

Fig. 3-15: Mean seasonal cycles of zonally averaged **(left)** mixed later depth in the B experiment and **(right)** B minus A mixed later depth.

Fig 3.16: Niño3 region (5°S-5°N; 150°W-90°W) SST diagnostics for experiments A (blue lines) and B (red lines): **(a)** SST seasonal cycle, **(b)** histogram of Niño3 index, **(c)** power density spectrum of Niño3 index.

Chapter 4

Fig. 4-1 Schematic illustration of the path and strength of winter storms around high (H) and low (L) pressure zones in the North Atlantic corresponding to positive (left) and negative (right) NAO phases. From http://www.ldeo.columbia.edu/res/pi/NAO/

Fig. 4-2 DJFM North Atlantic atmospheric variability. **(a)** NAO index (NAO+ in yellow bars, NAO-in blue bars) and its 9-point running mean (black line), **(b)** sea level pressure (hPa) climatology (contours) and regression onto NAO index (colors), **(c)** regression onto NAO index of wind stress (arrows, in N m^{-2}) and wind speed (colors, in m sec^{-1}), **(d)** wind stress curl (N m^{-3}×10^{-7}) climatology (contours) and regression onto NAO index (colors).

Fig. 4-3 DJFM climatologies (contours) and regression onto the NAO index (colors) of DJFM anomalies of **(a)** net surface heat flux in W m^{-2} (defined positive downwards), **(b)** mixed layer depth (MLD) in m, **(c)** sea surface temperature (SST) in °C, **(d)** precipitation in mm day^{-1}, **(e)** surface salinity, **(f)** evaporation minus precipitation (E minus P) in mm day^{-1}, **(g)** sea surface height in cm, **(h)** ocean vertical velocity at 50 m depth in cm day^{-1}.

Fig. 4-4 (left) DJFM surface current climatology (cm sec^{-1}), **(right)** DJFM surface currents regressed onto NAO index and salinity flux due to surface horizontal advection (mm day^{-1}).

Fig. 4-5 Climatologies (contours) and regression onto NAO index (colors) of annual anomalies of **(a)** phosphate in mmol m^{-2}, **(b)** total chlorophyll in mg m^{-2}, **(c)** mesozooplankton in mg C m^{-2}, **(d)** particulate organic carbon (POC) production in mol C m^{-2} year^{-1}, **(e)** surface CO_2 partial pressure (pCO_2) in μatm, **(f)** sea-air CO_2 flux (defined positive upwards) in mol C m^{-2} year^{-1}. Variables in panels a-d are integrated over the euphotic depth.

Fig. 4-6 Variance explained by the NAO index (%) of **(a)** euphotic-depth-integrated phosphate concentration, **(b)** euphotic-depth-integrated chlorophyll concentration, **(c)** euphotic-depth-integrated mesozooplankton concentration, **(d)** euphotic-depth-integrated particulate organic carbon (POC) production, **(e)** surface CO_2 partial pressure (pCO_2), **(f)** sea-air CO_2 flux.

Fig. 4-7: (a) simulated chlorophyll concentration in spring (AMJJ) anomalies averaged over the euphotic layer depth (mg m^{-3}) regressed onto the normalized simulated NAO index and **(b)** spring (AMJJ) SeaWiFS satellite chlorophyll concentration anomalies (mg m^{-3}) during the years 1998-2006 regressed onto the normalized observed Hurrell NAO index.

Fig. 4-8 Climatological (black), NAO+ (red), and NAO- (blue) seasonal cycles in the subpolar gyre region of **(a)** mixed layer depth in m (note reversed axis), **(b)** phosphate concentration in mmol m^{-2}, **(c)** diatom concentration in mg C m^{-2}, **(d)** mesozooplankton concentration in mg C m^{-2}, **(e)** particulate organic carbon (POC) production in mol C m^{-2} year^{-1}, **(f)** sea-air CO_2 flux (defined positive upwards) in mol C m^{-2} year^{-1}. Variables in panels b-e are integrated over the euphotic depth.

Fig. 4-9 Climatological (black), NAO+ (red), and NAO- (blue) seasonal cycles in the subpolar latitudes of the North Atlantic (45°-60°N) of **(top)** SeaWiFS satellite estimates of chlorophyll values (mg m^{-3}) during the years 1998-2006 and **(bottom)** model chlorophyll concentration (mg m^{-3}).

Fig. 4-10 Climatological (black), NAO+ (red) and NAO- (blue) seasonal cycles in the Sargasso Sea near BATS of **(a)** mixed layer depth in m (note reversed axis), **(b)** phosphate concentration in mmol PO$_4$ m^{-2}, **(c)** diatom concentration in mg C m^{-2}, **(d)** mesozooplankton concentration in mg C m^{-2}, **(e)** particulate organic carbon (POC) production in mol C m^{-2} year^{-1}, **(f)** sea-air CO_2 flux (defined positive upwards) in mol C m^{-2} year^{-1}. Variables in panels b-e are integrated over the euphotic depth.

Fig. 4-11 Lagged correlations between NAO index and DJFM SST anomalies with **(a)** no lag, **(b)** 1 year lag, **(c)** 2 years lag, **(d)** 3 years lag. Correlation coefficients lower than 0.14 are not statistically significant at 95% confidence level and are not shown.

Fig. 4-12 Lagged correlations between Hurrell NAO index and Hadley SST DJFM anomalies for the period 1930-2002 with **(a)** no lag, **(b)** 1 year lag, **(c)** 2 years lag, **(d)** 3 years lag. Correlation coefficients lower than 0.24 are not statistically significant at 95% confidence level and are not shown.

Fig. 4-13 Decorrelation time scale for 200 years of the simulated NAO index (black line, circles) and for the 1860-2009 Hurrell NAO index (gray line, triangles).

Fig. 4-14 Lagged correlations between NAO index and spring-summer (AMJJ) chlorophyll anomalies with **(a)** no lag, **(b)** 1 year lag, **(c)** 2 years lag, **(d)** 3 years lag. Correlation coefficients lower than 0.14 are not statistically significant at 95% confidence level and are not shown.

Fig. 4-15 In-phase (left) and in-quadrature (right) response to NAO+ low-frequency phases of (a,b) sea surface temperature (SST) in °C, (c,d) heat content integrated between 0-300 m depth in J m^{-2} and (e,f) sea surface salinity (SSS).

Fig. 4-16 In-phase (top) and in-quadrature (bottom) response to NAO+ low-frequency phases of (a,b) sea surface in cm (colors) and horizontal currents averaged between 40-100 m depth.

Fig. 4-17 In-phase response to low-frequency NAO+ phases of **(a)** mixed layer depth (m), **(b)** euphotic-depth-integrated phosphate concentration (mmol m^{-2}), **(c)** euphotic-depth-integrated chlorophyll concentration (mg m^{-2}), **(d)** sea-air CO_2 fluxes in mol m^{-2} year^{-1}.

Fig. 4-18 Schematic diagram of processes affecting subpolar gyre air-to-sea CO_2 fluxes and production of particulate organic matter during positive (NAO+) and negative (NAO-) phases.

Chapter 5

Fig. 5-1 XX century JFM sea level pressure (hPa) regressed onto the first **(c)** and second **(d)** principle component (PC) time series of JFM SLP anomalies with winter climatology plotted in contours for reference; JFM wind velocity (m sec^{-1}) at 10 m height regressed onto the first **(c)** and second **(d)** PC time series of JFM SLP anomalies; JFM wind stress curl (1×10^{-7} N m^{-3}) regressed onto the first **(e)** and second **(f)** PC time series of JFM SLP anomalies. For construction these maps show anomalies relative to index values equal to1.

Fig. 5-2 (a) First (PC1, light grey) and **(b)** second (PC2, dark grey) PC time series of JFM SLP anomalies during the XX and XXI centuries (bars). **(c)** First (PC1, light grey) and **(d)** second (PC2, dark grey) PC time series of JFM SST anomalies during the XX and XXI centuries (bars). Red lines indicate 9-year running averages and numbers indicate the variance explained by each mode during the XX and XXI centuries.

Fig. 5-3 XX century JFM climatologies (contours) and JFM regressions (colors) with the first **(left)** and second **(right)** mode of sea level pressure variability of **(a,b)** net surface heat fluxes (NET) in W m^{-2}, **(c-d)** sea surface temperature (SST) in °C, **(e-f)** mixed layer depth (MLD) in m.

Fig. 5-4 XX century variance explained (%) by the first **(left)** and second **(right)** principle component time series (PC) of sea level pressure variability; **(a,b)** net surface heat fluxes (NET), **(c-d)** sea surface temperature (SST), **(e-f)** mixed layer depth (MLD). Note the different color scale of panels **(a,b)**.

Fig. 5-5 XX century (top) and XXI century (bottom) April-July (AMJJ) euphotic-depth-integrated chlorophyll concentration in mg m^{-2}. Contours: AMJJ climatology; colors: regression onto the **(a)** first and **(b)** second principle component (PC) time series of JFM sea level pressure anomalies.

Fig. 5-6 XX century **(top)** and XXI century **(bottom)** April-July (AMJJ) euphotic-depth integrated chlorophyll concentration: variance explained by the **(a,c)** first and **(b,d)** second principle component (PC) time series of JFM sea level pressure anomalies.

Fig. 5-7 Differences between the last 30 years of the XXI and XX centuries (colors) and climatology of the last 30 years of the XX century (contours) of **(a)** JFM sea surface temperature (SST) in °C, **(b)** JFM sea surface salinity, **(c)** JFM mixed layer depth (MLD) in m, **(d)** JFM winds (arrows) and total wind speed (colors) at 10 m height.

Fig. 5-8 April-July (AMJJ) euphotic-depth-integrated chlorophyll concentration (CHL) in mg m^{-2}. **(a)** Differences between XX and XXI century medians (colors) and XX century median (contours), **(b)** statistical significance at 95% (grey shading) of XX and XXI century median differences; **(c)** differences between XX and XXI century standard deviations (colors) and XX century standard deviation (contours), **(d)** statistical significance at 95% (grey shading) of XX and XXI century standard deviation differences.

Fig. 5-9 XX and XXI century time series averaged in the subpolar North Pacific (45°-60°N, 150°E-130°W), of **(a)** sea surface temperature (SST) in °C, **(b)** mixed layer depth (MLD) in m, **(c)** euphotic-depth-integrated chlorophyll concentration (CHL) concentration in mg m^{-2} (grey), **(d)** euphotic-depth-averaged chlorophyll concentration (CHL) in mg m^{-3} (grey) and chlorophyll estimated from SeaWiFS satellite data for the years 1998-2006 (blue). In panels **(c)** and **(d)**, the linear trend relative to the years 1900-1949 is shown (red full line) and extended for reference also in remaining part of the time series (red dashed line).

Fig. 5-10 XX and XXI century time series averaged in the central North Pacific (20°-45°N, 160°E-130°W), of **(a)** sea surface temperature (SST) in °C, **(b)** mixed layer depth (MLD) in m, **(c)** euphotic-depth-integrated chlorophyll concentration (CHL) concentration in mg m^{-2} (grey), **(d)** euphotic-depth-averaged chlorophyll concentration (CHL) in mg m^{-3} (grey) and chlorophyll estimated from SeaWiFS satellite data for the years 1998-2006 (blue). In panels **(c)** and **(d)**, the linear trend relative to the years 1900-1949 is shown (red full line) and extended for reference also in remaining part of the time series (red dashed line).

Fig. 5-11 Climatological seasonal cycles of euphotic-depth-averaged chlorophyll concentration computed over the last 30 years of XX century (blue line) and of the XXI century (red line) over **(left)** the subpolar North Pacific (45°-60°N, 150°E-130°W) and **(right)** over the central North Pacific (20°-45°N, 160°E-140°W).

References

Alexander, M. A., and C. Deser (1995): A mechanism for the recurrence of wintertime midlatitude SST anomalies. J. Phys. Oceanogr., 25, 122–137.

Alexander, M., A. Capotondi, A. Miller, F. Chai, R. Brodeur, and C. Deser (2008): Decadal variability in the northeast Pacific in a physical-ecosystem model: Role of mixed layer depth and trophic interactions, J. Geophys. Res., 113, C02017, doi:10.1029/2007JC004359.

Alvain, S., Moulin, C., Dandonneau, Y., Loisel, H. (2008): Seasonal distribution and succession of dominant phytoplankton groups in the global ocean: A satellite view, Global Biogeochem. Cy., 22, GB3001, doi:10.1029/2007GB003154.

Anderson, W.G., Gnanadesikan, A., Hallberg, R., Dunne, J., Samuels, B. L. (2007): Impact of ocean color on the maintenance of the Pacific Cold Tongue, Geophys. Res. Lett., 34 (11), Art. No. L11609.

Anderson, W., Gnanadesikan, A., Wittenberg, A. (2009): Regional impacts of ocean color on tropical Pacific variability, Ocean Science, 5 (3), 313-327.

Antonov, J. I., Levitus, S., Boyer, T. P., Conkright, M. E., O'Brien, T., and Stephens C. (1998): World Ocean Atlas 1998 Vol. 2: Temperature of the Pacific Ocean, NOAA Atlas NESDIS 28. U.S. Government Printing Office, Washington, D.C.

Barber, R.T. & Chavez, F.P. (1983) Biological consequences of El Niño. Science (Washington, DC), 222, 1203–1210.

Baretta, J.W., Ebenhoh, W., Ruardij, P. (1995): The European-Regional-Seas-Ecosystem-Model, a complex marine ecosystem model, Netherlands Journal of Sea Research, 33 (3-4), 233-246.

Barton AD, Green CH, Monger BC, Pershing AJ (2003): The continuous plankton recorder survey and the North Atlantic Oscillation: interannual- to multidecadal-scale patterns of phytoplankton variability in the North Atlantic Ocean, Prog. Oceanogr., 58:337–358.

Bates, N.R. (2001): Interannual variability of oceanic CO_2 and biogeochemical properties in the Western North Atlantic subtropical gyre. Deep-Sea Res. II 48 (8–9), 1507–1528.

Bates, N.R. (2007): Interannual variability of the oceanic CO_2 sink on the subtropical gyre of the North Atlantic Ocean over the last 2decades. J. Geophys. Res. 112.

Behrenfeld, M., R. O'Malley, D. A. Siegel, C. McClain, J. Sarmiento, G. Feldman, P. Falkowski, E. Boss, and A. Milligan (2006): Climate-driven trends in contemporary ocean productivity, Nature, 444, 752– 755.

Belkin, I. M. (2004)**:** Propagation of the "Great Salinity Anomaly" of the 1990s around the northern North Atlantic, Geophys. Res. Lett., 31 (8): Art. No. L08306.

Bellucci, A., Gualdi, S., Scoccimarro, E., Navarra, A. (2008): NAO-ocean circulation interactions in a coupled general circulation model. Climate Dyn ., 31 ,759-777.

Bjerknes, J. (1964): Atlantic air-sea interactions, Advances in Geophysics, 10, 1-82.

Bjerknes, J. (1969): Atmospheric teleconnections from the equatorial Pacific, Monthly Weather Review, 97, 163–172.

Blanke, B.; Delecluse, P. (1993): Variability of the Tropical Atlantic Ocean simulated by a general circulation model with 2 different mixed-layer physics, J. Phys. Oceanogr., 23 (7),1363-1388 JUL 1993

Boening, C., M. Scheinert, J. Dengg, A. Biastoch, and A. Funk (2006): Decadal variability of subpolar gyre transport and its reverberation in the North Atlantic overturning, Geophys. Res. Lett., 33, L21S01, doi:10.1029/2006GL026906.

Bond, N. A., J. E. Overland, M. Spillane, and P. Stabeno (2003): Recent shifts in the state of the North Pacific, Geophys. Res. Lett., 30(23), 2183, doi:10.1029/2003GL018597.

Bopp, L., Monfray, P., Aumont, O., Dufresne, J.L., Le Treut, H., Madec, G., Terray, L., Orr, J.C. (2001): Potential impact of climate change on marine export production, Global Biogeochem. Cy., 15 (1), 81-99.

Bopp, L., Aumont, O., Cadule, P., Alvain, S., and Gehlen M. (2005): Response of diatoms distribution to global warming and potential implications: A global model study, Geophys. Res. Lett., 32, L19606, doi:10.1029/2005GL023653.

Boyd, P., Doney, S.C. (2003): The impact of climate change and feedback process on the ocean carbon cycle. In: Ocean Biogeochemistry: The Role of the Ocean Carbon Cycle in Global Change (ed. Fasham MJR), pp. 157–187. Springer, Berlin.

Boyer, T. P., Levitus, S., Antonov, J. I., Conkright, M. E., O'Brien, T., Stephens, C. (1998): World Ocean Atlas 1998 Vol. 5: Salinity of the Pacific Ocean, NOAA Atlas NESDIS 31. U.S. Government Printing Office, Washington, D.C..

Cayan, D.R. (1992): Latent and sensible heat flux anomalies over the Northern Oceans driving the sea surface temperature, J. Phys. Oceanogr., 22 (8): 859-881.

Chai, F., M. Jiang, R. T. Barber, R. C. Dugdale, and Y. Chao (2003), Interdecadal variation of the transition zone chlorophyll front: A physical-biological model simulation between 1960 and 1990, J. Oceanogr., 59, 461–475.

Conkright, M., Garcia, H., O'Brien, T., Locarnini, R., Boyer, T., Stephens, C., Antonov, J. (2002): World Ocean Atlas 2001, Volume 4: Nutrients. In: NOAA Atlas NESDIS 52. U.S. Government Printing Office, Washington D.C..

Corti, S., Molteni, F., Palmer, T.M. (1999): Signature of recent climate change in frequencies of natural atmospheric circulation regimes, Nature, 398, 799– 802.

Curry, R. G., McCartney, M. S. (2001): Ocean gyre circulation changes associated with the North Atlantic Oscillation, J. Phys. Oceanog., 31, 3374–3400.

de Boyer Montégut, C., Madec, G., Fischer, A. S., Lazar, A., Iudicone, D. (2004): Mixed layer depth over the global ocean: An examination of profile data and a profile-based climatology, J. Geophys. Res., 109, C12003, doi:10.1029/2004JC002378.

de Coëtlogon, G., Frankignoul, C. (2003): On the persistence of winter sea surface temperature in the North Atlantic. J. Climate, 16, 1364-1377.

Denman, K., Hofmann, E., Marchant, H. (1996), Marine biotic responses to environmental change and feedbacks to climate, in Climate Change 1995, edited by J. T. Houghton et al., pp. 483– 516, Cambridge Univ. Press, New York.

Deser, C., Alexander, M. A., Timlin, M. S. (2003): Understanding the persistence of sea surface temperature anomalies in midlatitudes, J. Climate, 16, 57– 72.

Deser, C., Phillips, A. S. (2006): Simulation of the 1976/77 climate transition over the North Pacific: Sensitivity to tropical forcing, J. Climate, 19, 6170–6180.

Deshayes, J., Frankignoul, C. (2008): Simulated variability of the circulation in the North Atlantic from 1953 to 2003. J. Climate, 21, 4919–4933.

Dickson, A. G., Riley, J. P (1979): The estimation of acid dissociation constants in seawater media from potentiometric titrations with strong base. I. The ionic product of water (KW). Marine Chemistry, 7, 89–99.

Dickson, A. G. (1990) Standard potential of the reaction: $AgCl(s) + 1/2H_2(g) = Ag(s) + HCl(aq)$, and the standard acidity constant of the ion HSO_4 in synthetic sea water from 273.15 to 318.15 K. Journal of Chemical Thermodynamics 22, 113–127.

Dickson, A.G., Goyet, C. (1994): Handbook of methods for the analysis of the various parameters of the carbon dioxide system in seawater (Version 2). DOE (US Department of Energy) ORNL/CDIAC-74, Carbon Dioxide Information and Analysis Center, Oak Ridge, TN

Di Lorenzo, E., Schneider, N., Cobb, K.M., Franks, P.J.S., Chhak, K., Miller, A.J., McWilliams, J.C., Bograd, S.J., Arango, H., Curchister, E., Powell, T.M., Riviere, P., 2008. North Pacific gyre oscillation links ocean climate and ecosystem change. Geophysical Research Letters 35, L08607, doi:10.1029/2007GL032838.

Di Lorenzo, E., Fiechter, J., Schneider, N., Bracco, A., Miller, A. J., Franks, P. J. S. , Bograd, S. J., Moore, A. M., Thomas, A. C., Crawford, W., Peña, A., Hermann, A. J. (2009), Nutrient and salinity decadal variations in the central and eastern North Pacific, Geophys. Res. Lett., 36, L14601, doi:10.1029/2009GL038261

D'Orgeville, M., Peltier, W. R. (2009): Implications of Both Statistical Equilibrium and Global Warming Simulations with CCSM3. Part I: On the Decadal Variability in the North Pacific Basin, J. Climate, 22, 20, 5277–5297.

Drinkwater, K.F., Belgrano, A., Borja, A., Conversi, A., Edwards, M., Greene, C.H., Ottersen, G., Pershing, A.J., Walker, H., (2003). The response of marine ecosystems to climatic variability associated with the North Atlantic Oscillation, Geophys. Monogr. Ser., vol. 134, edited by J. W. Hurrell et al., pp. 211–234, AGU, Washington D. C.

Drinkwater, K.F., Beaugrand, G., Kaeriyama, M., Kim, S., Ottersen, G., Perry, R.I., Poertner, H.-O., Polovina, J.,J., Takasuka, A. (2010): On the processes linking climate to ecosystem changes, J. Mar. Syst., 79, 374-388.

Dutkiewicz, S., Follows, M., Marshall, J. Gregg, W.W. (2001): Interannual variability of phytoplankton abundances in the North Atlantic, Deep-Sea Research II 48, 2323–2344.

Eden, C., Jung, T. (2001): North Atlantic Interdecadal Variability: Oceanic response to the North Atlantic Oscillation (1865-1997), J. Climate, 14, 676-691.

Eden C, Willebrand, J. (2001): Mechanisms of interannual to decadal variability in the North Atlantic circulation, J. Climate, 14, 2266–2280.

Esselborn, S., Eden, C. (2001): Sea surface height changes in the North Atlantic Ocean related to the North Atlantic Oscillation, Geophys. Res. Lett., 28, 3473–3476.

Flatau, M. K., Talley, L., Niiler, P. P. (2003): The North Atlantic Oscillation, surface current velocities, and SST changes in the subpolar North Atlantic, J. Climate, 16 (14), 2355-2369

Fogli, P.G., Manzini, E., Vichi, M., Alessandri, A., Patara, L., Gualdi, S., Scoccimarro, E., Masina, S., Navarra, A. (2009): INGV-CMCC Carbon (ICC): A Carbon Cycle Earth System Model, CMCC Research Paper No. 61.

Follows, M., Dutkiewicz, S. (2002): Meterological modulation of the North Atlantic spring bloom, Deep-Sea Research II 49, 321–344.

Follows, M.J., Ito, T., Dutkiewicz, S. (2006): On the solution of the carbonate chemistry system in ocean biogeochemistry models, Ocean Modelling, 12 (3-4), 290-301.

Forster, P., V. Ramaswamy, P. Artaxo, T. Berntsen, R. Betts, D.W. Fahey, J. Haywood, J. Lean, D.C. Lowe, G. Myhre, J. Nganga, R. Prinn, G. Raga, M. Schulz and R. Van Dorland (2007): Changes in Atmospheric Constituents and in Radiative Forcing. In: Climate Change 2007: The Physical Science Basis. Contribution of Working Group I to the Fourth Assessment Report of the Intergovernmental Panel on Climate Change [Solomon, S., D. Qin, M. Manning, Z. Chen, M. Marquis, K.B. Averyt, M.Tignor and H.L. Miller (eds.)]. Cambridge University Press, Cambridge, United Kingdom and New York, NY, USA.

Frankignoul, C., P. Muller, and E. Zorita (1997): A simple model of the decadal response of the ocean to stochastic wind forcing, J. Phys. Oceanogr., 27, 1533–1546.

Frankignoul, C., Czaja, A., L'Hevender, B. (1998): Air-sea feedback in the North Atlantic and surface boundary conditions for ocean models, J. Climate, 11, 2310–2324.

Frankignoul, C., De Coëtlogon, G., Joyce, T.M., Dong, S. (2001): Gulf Stream variability and ocean-atmosphere interactions, J. Phys. Oceanogr. 31, 3516–3528.

Frankignoul, C., Deshayes, J., Curry, R. (2009): The role of salinity in the decadal variability of the North Atlantic meridional overturning circulation, Climate Dyn, 33 (6), 777-793.

Freeland, H., Denman, K., Wong, C.S., Whitney, F., Jacques, R. (1997): Evidence of change in the winter mixed layer in the Northeast Pacific Ocean, Deep-Sea Research I, 44, 2117-2129.

Friedlingstein, P., Bopp, L., Ciais, P., Dufresne, J.L., Fairhead, L., LeTreut, H., Monfray, P., Orr, J.C (2001): Positive feedback between future climate change and the carbon cycle, Geophys. Res. Lett., 28 (8), 1543-1546.

Geider, R.J., MacIntyre, H.L., Kana, T.M. (1997): Dynamic model of phytoplankton growth and acclimation: Responses of the balanced growth rate and the chlorophyll a : carbon ratio to light, nutrient-limitation and temperature, Marine Ecology-Progress Series, 148 (1-3), 187-200.

Gent, P.R., McWilliams, J.C. (1990): Isopycnal mixing in ocean circulation models, J. Phys. Oceanogr., 20 (1), 150-155.

Gildor, H., Naik, N.H. (2005): Evaluating the effect of interannual variations of surface chlorophyll on upper ocean temperature, J. Geophys. Res.- Oceans, 110 (C7), Art. No. C07012.

Gillett, N.P., 2005: Northern Hemisphere circulation, Nature, 437, 496.

Gillett, N. P., F. W. Zwiers, A. J. Weaver, and P. A. Stott (2003): Detection of human influence on sea-level pressure, Nature, 422, 292– 294.

Gnanadesikan, A., Anderson, W.G. (2009): Ocean Water Clarity and the Ocean General Circulation in a Coupled Climate Model, J. Phys. Oceanogr., 39 (2), 314-332.

Gregg, W.W., Ginoux, P., Schopf, P.S., Casey, N.W. (2003): Phytoplankton and iron: validation of a global three-dimensional ocean biogeochemical model, Deep-Sea Res. – Part II, 50 (22-26), 3143-3169.

Greatbatch, R. J., (2000): The North Atlantic Oscillation, Stochastic Environ. Res. Risk Assess., 14, 213–241.

Gruber, N., Keeling, C.D., Bates, N.R. (2002): Interannual variability in the North Atlantic Ocean carbon sink, Science, 298, 2374– 2378.

Gu, D.F., Philander, S.G.H. (1997): Interdecadal climate fluctuations that depend on exchanges between the tropics and Extratropics, Science, 275 (5301): 805-807.

Guilyardi, E., Wittenberg, A., Fedorov, A., Collins, M., Wang, C.Z., Capotondi, A., van Oldenborgh, G.J., Stockdale, T. (2009): Understanding El Niño in Ocean-Atmosphere General Circulation Models, Progress and Challenges, Bull. Amer. Meteor. Soc., 90 (3), 325.

Haekkinen, S., Rhines, P. (2004): Decline of subpolar North Atlantic circulation during the 1990s, Science, 304, 555 – 559, doi:10.1126/ science.1094917.

Hansen, D.V., Bezdek, H.F. (1996): On the nature of decadal anomalies in North Atlantic sea surface temperature, J. Geophys. Res., 101, 8749–8758.

Hare, S.R., Mantua, N.J. (2000): Empirical evidence for North Pacific regime shifts in 1977 and 1989, Progr. Oceanogr., 47,103– 145.

Hashioka, T., Sakamoto, T.T., Yamanaka, Y. (2009): Potential impact of global warming on North Pacific spring blooms projected by an eddy-permitting 3-D ocean ecosystem model, Geophys. Res. Lett., 36, L20604, doi:10.1029/2009GL038912.

Hays, J.D. (1976): Variation in the Earth's orbit: Pacemaker of the Ice Ages, Science, 194, 4270,1121-1132.

Held, I.M., Soden, B.J. (2000): Water vapor feedback and global warming, Annual Review of Energy and the Environment, 25, 441-475.

Henson, S. A., Robinson, I., Allen, J. T., Waniek, J. J. (2006): Effect of meteorological conditions on interannual variability in timing and magnitude of the spring bloom in the Irminger Basin, North Atlantic, Deep Sea Res., Part I, 53, 1601– 1615, doi:10.1016/j.dsr.2006.07.009.

Henson, S. A., Dunne, J. P., and Sarmiento, J. L. (2009): Decadal variability in North Atlantic phytoplankton blooms, J. Geophys. Res., 114, C04013, doi:10.1029/2008JC005139.

Herbaut, C., Houssais, M.-N. (2009): Response of the eastern North Atlantic subpolar gyre to the North Atlantic Oscillation. GRL, 36, 17, L17607, doi:10.1029/2009GL03909.

Hibbard, K., Meehl, G., Cox, P., Friedlingstein, P. (2007): A strategy for climate change stabilization experiments, EOS, 88(20), 217, 10.1029/2007EO200002.

Holton, J.R. (1992): An Introduction to Dynamic Meteorology, Ed. 4, 535 pag Holton, J. R., 1992, Academic Press, San Diego, 507 pp.

Hou, A.Y., Lindzen, R.S. (1992): The influence of concentrated heating on the Hadley Circulation, Journal of the Atmospheric Sciences, 49 (14), 1233-1241.

Houghton, B., Visbeck, M. (2002): Quasi-decadal salinity fluctuations in the Labrador Sea, J. Phys. Oceanogr., 32, 687–701.

Hurrell, J., Kushnir, Y., Ottersen, G., Visbeck, M. (2003): An overview of the North Atlantic Oscillation. In: Hurrell, J., Kushnir, J., Ottersen, G., Visbeck, M. (eds) The North Atlantic Oscillation: climatic significance and environmental impact, American Geophysical Union, Washington DC.

Ihara, C., Kushnir, Y. (2009): Change of midlatitude westerlies in XXI century climate simulations, Geophys. Res. Lett., 36, L13701, doi:10.1029/2009GL037674.

Jerlov, N.G. (1968): Optical oceanography, American Elsevier Publ. Co., Inc., New York.

Jungclaus, J.H., Keenlyside, N., Botzet, M., Haak, H., Luo, J.J., Latif, M., Marotzke, J., Mikolajewicz, U., Roeckner, E. (2006): Ocean circulation and tropical variability in the coupled model ECHAM5/MPI-OM, J. Climate, 19 (16), 3952-3972.

Kalnay et al. (1996): The NCEP/NCAR 40-year reanalysis project, Bull. Amer. Meteor. Soc., 77, 437-470.

Kaplan, A., Cane, M., Kushnir, Y., Clement, A., Blumenthal, M., Rajagopalan, B. (1998): Analyses of global sea surface temperature 1856-1991, J. Geophys. Res., 103, 18, 567-18, 589.

Karl, D.M., Bidigare R.R., Letelier, R.M. (2001): Longterm changes in plankton community structure and productivity in the North Pacific Subtropical Gyre: The domain shift hypothesis. Deep-Sea Res., 48, 1449–1470.

Karl, D.M., Bates, N., Emerson, S., Harrison, P.J., Jeandel, C., Llinas, O., Liu, K.K., Marty, J. C., Michaels, A.F., Miguel, J.C., Neuer, S., Nojiri, Y., Wong, C.C. (2003): Temporal studies of biogeochemical processes determined from ocean time-series observations during the JGOFS era, in Ocean Biogeochemistry: The Role of the Ocean Carbon Cyclein Global Change, edited by M. J. R. Fasham, pp. 239– 267, Springer-Verlag, New York.

Keeley, S. P. E., M. Collins, and A. J. Thorpe 2008: Northern Hemisphere Winter Atmospheric Climate: Modes of Natural Variability and Climate Change, Clim. Dyn, 31, 195-211, doi:10.1007/s00382-007-0346-6.

Keenlyside, N., Latif, M., Jungclaus, J., Kornblueh, L., Roeckner, E. (2008): Advancing decadal-scale climate prediction in the North Atlantic sector, Nature 453, 84–88, DOI:10.1038/nature06921.

Key, R.M., Kozyr, A., Sabine, C.L., Lee, K., Wanninkhof, R., Bullister, J.L., Feely, R.A., Millero, F.J., Mordy, C., Peng, T.H. (2004): A global ocean carbon climatology: Results from global data analysis project (GLODAP), Glob. Biogeochem. Cy., 18(4), GB4031

Koertzinger, A., Send, U., Lampitt, R.S., Hartman, S., Wallace, D.W.R., Karstensen, J., Villagarcia, M.G., Llinas, O., DeGrandpre, M.D. (2008): The seasonal pCO2 cycle at 491N/16.51W in the northeast Atlantic Ocean and what it tells us about biological productivity, J. Geophys. Res. 113, C04020.

Krahmann, G., Visbeck, M., Reverdin, G. (2001): Formation and propagation of temperature anomalies along the North Atlantic Current, J. Phys. Oceanogr., 31, 1287–1303.

Kwon, Y.-O., Deser, C. (2007): North Pacific decadal variability in the Community Climate System Model version 2. J. Climate, 20, 2416–2433.

Latif, M., Barnett, T.P. (1996): Decadal variability over the North Pacific and North America: Dynamics and predictability, J. Climate, 9, 2407–2423.

Latif, M. (1998): Dynamics of interdecadal variability in coupled ocean-atmosphere models, J. Climate, 11 (4), 602-624.

Lengaigne, M., Menkes, C., Aumont, O., Gorgues, T., Bopp, L., Andre, J.M., Madec, G. (2007): Influence of the oceanic biology on the tropical Pacific climate in a coupled general circulation model, Climate Dynamics, 28 (5), 503-516.

Lengaigne, M., Madec, G., Bopp, L., Menkes, C., Aumont, O., Cadule, P.: Bio-physical feedbacks in the Arctic Ocean using an Earth System Model (2009): Geophys. Res. Lett., 36 L21602, doi:10.1029/2009GL040145.

Leterme S.C., Edwards M., Seuront L., Attrill M. J., Reid P.C., John A.W.G.: Decadal basin-scale changes in diatoms, dinoflagellates, and phytoplankton color across the North Atlantic, Limnol. Oceanogr., 50 (4), 1244–1253, 2005.

Le Treut, H., R. Somerville, U. Cubasch, Y. Ding, C. Mauritzen, A. Mokssit, T. Peterson and M. Prather, 2007: Historical Overview of Climate Change. In: *Climate Change 2007: The Physical Science Basis. Contribution of Working Group I to the Fourth Assessment Report of the Intergovernmental Panel on Climate Change* [Solomon, S., D. Qin, M. Manning, Z. Chen, M. Marquis, K.B. Averyt, M. Tignor and H.L. Miller (eds.)]. Cambridge University Press, Cambridge, United Kingdom and New York, NY, USA.

Levitus, S., Antonov, J. I. & Boyer, T. P. Interannual variability of temperature at a depth of 125 metres in the North Atlantic ocean. *Science* **266,** 96–99 (1994).

Levitus, S., T. Boyer, M. Conkright, T. O'Brien, J. Antonov, C. Stephens, L. Stathoplos, D. Johnson, and R. Gelfeld (1998), WORLD OCEAN DATABASE 1998: Vol. 1: Introduction, vol. NOAA Atlas NESDIS 18, 346 pp., U.S. Gov. Printing Office, Washington D.C.

Lévy, M., Klein, P., and Treguier, A. M. (2001): Impact of sub-mesoscale physics on production and subduction of phytoplankton in an oligotrophic regime, J. Mar. Res., 59(4), 535–565.

Lévy, M., Lehahn, Y., Andre, J. M., Memery, L., Loisel, H., Heifetz, E. (2005): Production regimes in the northeast Atlantic: A study based on Sea-viewing Wide Field-of-view Sensor (SeaWiFS) chlorophyll and ocean general circulation model mixed layer depth, J. Geophys. Res., 110, C07S10, doi:10.1029/2004JC002771.

Li, M., Myers, P.G., Freeland, H. (2005): An examination of historical mixed layer depths along Line-P in the Gulf of Alaska, Geophys. Res. Lett., 32, L05613, doi:10.1029/2004GL021911.

Lin, J.L. (2007): The Double-ITCZ Problem in IPCC AR4 Coupled GCMs: Ocean–Atmosphere Feedback Analysis, Journal of Climate, 20, DOI: 10.1175/JCLI4272.1.

Linkin, M. E., Nigam, S. (2008): The North Pacific Oscillation–West Pacific Teleconnection Pattern: Mature-Phase Structure and Winter Impacts, Journal of Climate, 21, DOI: 10.1175/2007JCLI2048.1.

Liu, Z.Y., Alexander, M. (2007): Atmospheric bridge, oceanic tunnel, and global climatic teleconnections, Rev. Geophysics, 45 (2): Art. No. RG2005.

Lohmann, K., Drange, H., Bentsen M. (2009a): Response of the North Atlantic subpolar gyre to persistent North Atlantic Oscillation like forcing, Clim. Dyn., 32, 273–285, doi:10.1007/s00382-008-0467-6.

Lohmann, K., Drange, H., Bentsen M. (2009b): A possible mechanism for the strong weakening of the North Atlantic subpolar gyre in the mid-1990s, Geophys. Res. Lett., 36, L15602, doi:10.1029/2009GL039166.

Longhurst, A. R. (2007): Ecological Geography of the Sea, 2nd ed., Amsterdam, Boston, MA, Academic Press.

Loeptien, U., Eden, C., Timmermann, A., Dietze, H. (2009): Effects of biologically induced differential heating in an eddy-permitting coupled ocean-ecosystem model, J. Geophys. Res. Oceans, 114: Art. No. C06011.

Lorenz, D. J., DeWeaver, E.T. (2007): Tropopause height and zonal wind response to global warming in the IPCC scenario integrations, J. Geophys. Res., 112, D10119, doi:10.1029/2006JD008087.

Madec, G., Imbard, M. (1996): A global ocean mesh to overcome the North Pole singularity, CLIMATE DYNAMICS, 12 (6), 381-388.

Madec, G., Delecluse, P., Imbard, M., Levy, C. (1998): OPA 8.1 Ocean General Circulation Model Reference Manual, Note du Pole de Modélisation, 11, Institut Pierre Simon Laplace, 91pp.

Manizza, M., Le Quere, C., Watson, A.J., Buitenhuis, E.T. (2005): Bio-optical feedbacks among phytoplankton, upper ocean physics and sea-ice in a global model, Geophys, Res. Lett., 32 (5), Art. No. L05603.

Manizza, M., Le Quere, C., Watson, A.J., Buitenhuis, E.T. (2008): Ocean biogeochemical response to phytoplankton-light feedback in a global model, J. Geophys. Res. Oceans, 113 (C10), Art. No. C10010.

Mann K.H., Lazier J.R.N. (1996): Dynamics of marine ecosystems. Blackwell Scientific Publications, Oxford.

Mantua, N. J., Hare, S. R., Zhang, Y., Wallace, J. M., Francis, R. C. (1997): A Pacific interdecadal climate oscillation with impacts on salmon production, Bull. Amer. Meteor. Soc., 78, 1069–1079.

Mantua, N., Hare, S.: The Pacific decadal oscillation, J. Oceanogr., 58, 35– 44, 2002.

Marshall, J., Johnson, H., Goodman, J. (2001): A study of the interaction of the North Atlantic Oscillation with the ocean circulation, J. Climate, 14, 1399–1421.

Marshall, J., Plumb, R.A. (2008): Atmosphere, Ocean, and Climate Dynamics: An Introductory Text. Elsevier, Amsterdam, 319 pp.

Marzeion, B., Timmermann, A., Murtugudde, R., Jin, F.F. (2005): Biophysical feedbacks in the tropical Pacific, J. Climate, 18 (1), 58-70.

Masina, S., Di Pietro, P., Navarra, A. (2004): Interannual to decadal variability of the North Atlantic from an ocean data assimilation system, Climate Dyn., 23, doi:10.1007/s00382-004-0453-6.

McClain, C.R. (2009): A Decade of Satellite Ocean Color Observations, Annual Review of Marine Science, 1, 19-42.

McGillicuddy, D.J., Anderson, L.A., Doney, S.C., Maltrud M.E. (2003): Eddy-driven sources and sinks of nutrients in the upper ocean: Results from a 0.1° resolution model of the North Atlantic, Glob. Biogeochem. Cycles, 17(2), 1035, doi:10.1029/2002GB001987.

Meehl, G.A., T.F. Stocker, W.D. Collins, P. Friedlingstein, A.T. Gaye, J.M. Gregory, A. Kitoh, R. Knutti, J.M. Murphy, A. Noda, S.C.B. Raper,I.G. Watterson, A.J. Weaver and Z.-C. Zhao, 2007: Global Climate Projections. In: Climate Change 2007: The Physical Science Basis. Contribution of Working Group I to the Fourth Assessment Report of the Intergovernmental Panel on Climate Change [Solomon, S.,D. Qin, M. Manning, Z. Chen, M. Marquis, K.B. Averyt, M. Tignor and H.L. Miller (eds.)]. Cambridge University Press, Cambridge, United Kingdom and New York, NY, USA.

Miller, A. J., Schneider, N. (2000): Interdecadal climate regime dynamics in the North Pacific Ocean: Theories, observations and ecosystem impacts, Prog. Oceanogr., 47, 355–379.

Miller, R.L., Schmidt, G.A., Shindell, D.T. (2006): Forced variations of annular modes in the XX century IPCC AR4 simulations. J. Geophys. Res., 111, D18101, doi:10.1029/2005JD006323.

Millero F. J. (1995): Thermodynamics of the carbon dioxide system in the oceans. Geochimica et Cosmochimica Acta 59, 661–677.

Morel, A., Antoine, D. (1994): Heating rate within the upper ocean in relation to its bio-optical state**,** J. Phys. Oceanogr., 24 (7), 1652-1665.

Morris A. W., Riley, J. P. (1966): The bromide/chlorinity and sulphate/chlorinity ratio in sea water. Deep-Sea Research 13, 699–705.

Murtugudde, R., Beauchamp, J., McClain, C.R., Lewis, M., Busalacchi, A.J. (2002): Effects of penetrative radiation on the upper tropical ocean circulation, J. Climate, 15 (5): 470-486.

Nakamoto, S., Kumar, S.P., Oberhuber, J.M., Ishizaka, J., Muneyama, K., Frouin, R. (2001): Response of the equatorial Pacific to chlorophyll pigment in a mixed layer isopycnal ocean general circulation model, Geophys. Res. Lett., 28 (10), 2021-2024.

Nakicenovic, N., Swart, R. (Eds.) (2000): Special Report on Emissions Scenarios. A Special Report of Working Group III of the Intergovernmental Panel on Climate Change, 612 pp., Cambridge University Press, Cambridge, UK, ISBN 0521804930.

Navarra, A., Gualdi, S., Masina, S., Behera, S., Luo, J.J., Masson, S., Guilyardi, E., Delecluse, P., Yamagata, T.: Atmospheric horizontal resolution affects tropical climate variability in coupled models, JOURNAL OF CLIMATE, 21 (4): 730-750 FEB 2008

Newman, M., Compo, G.P., Alexander, M.A. 2003: ENSO-forced variability of the PDO. *J. Clim.*, **16**, 3853–3857.

Olsen, A., R. G. J. Bellerby, T. Johannessen, A. M. Omar, and I. Skjelvan (2003), Interannual variability in the wintertime air-sea flux of carbon dioxide in the northern North Atlantic, 1981– 2001, Deep Sea Res., Part I, 50, 1323– 1338.

Ono, T., A. Shiomoto, and T. Saino (2008), Recent decrease of summer nutrients concentrations and future possible shrinkage of the subarctic North Pacific high-nutrient low-chlorophyll region, *Global Biogeochem. Cycles*, 22, GB3027, doi:10.1029/2007GB003092.

Oschlies, A. (2001), NAO-induced long-term changes in nutrient supply to the surface waters of the North Atlantic, Geophys. Res. Lett., 28(9), 1751–1754.

Oschlies, A.: Feedbacks of biotically induced radiative heating on upper-ocean heat budget, circulation, and biological production in a coupled ecosystem-circulation model, JOURNAL OF GEOPHYSICAL RESEARCH-OCEANS, 109 (C12): Art. No. C12031 DEC 28 2004

Park, S., Deser, C., Alexander, M.A.: Estimation of the surface heat flux response to sea surface temperature anomalies over the global oceans, JOURNAL OF CLIMATE, 18, 4582, 2005.

Paulson, C.A., Simpson, J.J.: Irradiance measurements in upper ocean, JOURNAL OF PHYSICAL OCEANOGRAPHY, 7 (6): 952-956 1977

Peixoto, J. P., and A. H. Oort, 1992: *Physics of Climate.* American Institute of Physics, 520 pp

Philander, G.: El Niño, la Niña, and the Southern Oscillation, Academic Press, San Diego, California, USA, 1990.

Polovina, J. J., E. A. Howell, and M. Abecassis (2008). Ocean's least productive waters are expanding, Geophys. Res.Lett., 35, L03618, doi:10.1029/2007GL031745.

Power S, Colman R. 2006. Multi-year predictability in a coupled general circulation model. Climate Dynamics 26: 247–272.

Quadrelli, R., and J. M. Wallace, 2004: A simplified linear framework for interpreting patterns of Northern Hemisphere wintertime climate variability. *J. Climat*e, 17, 3728–3744.

Randall, D.A., R.A. Wood, S. Bony, R. Colman, T. Fichefet, J. Fyfe, V. Kattsov, A. Pitman, J. Shukla, J. Srinivasan, R.J. Stouffer, A. Sumi and K.E. Taylor, 2007: Cilmate Models and Their Evaluation. In: Climate Change 2007: The Physical Science Basis. Contribution of Working Group I to the Fourth Assessment Report of the Intergovernmental Panel on Climate Change [Solomon, S., D. Qin, M. Manning, Z. Chen, M. Marquis, K.B. Averyt, M.Tignor and H.L. Miller (eds.)]. Cambridge University Press, Cambridge, United Kingdom and New York, NY, USA.

Rauthe, M., A. Hense, and H. Paeth, 2004: A model intercomparison study of climate change-signals in extratropical circulation. Int. J. Climatol., 24, 643–662.

Rayner, N. A., D. E. Parker, E. B. Horton, C. K. Folland, L. V. Alexander, D. P. Rowell, E. C. Kent, and A. Kaplan: Global analyses of sea surface temperature, sea ice, and night marine air temperature since the late nineteenth century, JOURNAL OF GEOPHYSICAL RESEARCH, 108, 4407, doi:10.1029/2002JD002670, 2003.

Reverdin, G; Cayan, D; Kushnir, Y**:** Decadal variability of hydrography in the upper northern North Atlantic in 1948-1990, JOURNAL OF GEOPHYSICAL RESEARCH-OCEANS, 102 (C4): 8505-8531 APR 15 1997

Reverdin, G., P. P. Niiler, and H. Valdimarsson (2003), North Atlantic Ocean surface currents, J. Geophys. Res., 108(C1), 3002, doi:10.1029/ 2001JC001020.

Riley J. P. (1965) The occurrence of anomalously high fluoride concentrations in the North Atlantic. *Deep-Sea Research* **12**, 219–220.

Röckner, E., Bäuml, G., Bonaventura, L., Brokopf, R., Esch, M., Giorgetta, M., Hagemann, S., Kirchner, I., Kornblueh, L., Manzini, E., Rhodin, A., Schlese, U., Schulzweida, U., Tompkins, A.: The atmospheric general circulation model ECHAM5,

Part I: Model description, Max-Planck-Institute for Meteorology, Report No. 349, Hamburg, Germany, 2003.

Rogers, J. C., 1981: The North Pacific Oscillation. *J. Climatol.,* **1, 39–57.**

Roy R. N., L. N. Roy, K. M. Vogel, C. Porter-Moore, T. Pearson, C. E. Good, F. J. Millero & D. J. Cambell (1993): Determination of the ionization constants of carbonic acid inseawater in salinities 5 to 45 and temperatures 0 to 45 °C. *Marine Chemistry* 44, 249–267.

Santana-Casiano, J.M., Gonzalez-Davila, M., Rueda, M.J., Llinas, O., Gonzalez-Davila, E.F.: The interannual variability of oceanic CO2 parameters in the northeast Atlantic subtropical gyre at the ESTOC site, GLOBAL BIOGEOCHEMICAL CYCLES, 21 (1): Art. No. GB1015 MAR 8 2007

Sarmiento, J. L., Slater, R., Barber, R., Bopp, L., Doney, S.C., Hirst, A.C., Kleypas, J., Matear, R., Mikolajewicz, U., Monfray, P., Soldatov, V., Spall, S.A., Stouffer, R.: Response of ocean ecosystems to climate warming, GLOBAL BIOGEOCHEMICAL CYCLES, 18, GB3003, doi:1029/2003GB002134, 2004.

Sarmiento, J., and N. Gruber (2006), Ocean Biogeochemical Dynamics, Princeton Univ. Press, Princeton, N. J.

Scaife A.A., et al., 2005: A stratospheric influence on the winter NAO and North Atlantic surface climate, Geophys. Res. Lett., 32, L18715, doi:10.1029/2005GL023226.

Schneider, N., and B.D. Cornuelle, 2005:The forcing of the Pacific decadal oscillation.*J.Climate,***18,** 4355 –4373.

Schwing, F.B., Mendelssohn, R., Bograd, S.J., Overland, J.E., Wang, M., Ito, S.: Climate change, teleconnection patterns, and regional processes forcing marine populations in the Pacific, J. Mar. Syst.,79, 245–257.

Shell, K.M., Frouin, R., Nakamoto, S., Somerville, R.C.J.: Atmospheric response to solar radiation absorbed by phytoplankton, JOURNAL OF GEOPHYSICAL RESEARCH-ATMOSPHERES, 108 (D15): Art. No. 4445 AUG 2 2003

Siegel, DA, Doney, S.C., Yoder, J.A., 2002: The North Atlantic spring phytoplankton bloom and Sverdrup's critical depth hypothesis, SCIENCE, 296 (5568): 730-733.

Simmons, A.J., Gibson, J.K.: The ERA-40 project plan. Tech. Rep., ERA-40 Project Report Series 1, ECMWF, Reading, United Kingdom, 63 pp, 2000

Sinha, B. and Topliss, B. (2006) A description of interdecadal time-scale propagating North Atlantic sea surface temperature anomalies and their effect on winter European climate, 1948-2002. *Journal of Climate*, 19, (7), 1067-1079.

Stenseth, N. C., A. Mysterud, G. Ottersen, J. W. Hurrell, K.-S. Chan, and M. Lima, Ecological effects of climate fluctuations, *Science*, *297*, 1292–1296, 2002.

Strutton, P.G., Chavez, F.P.: Biological heating in the equatorial Pacific: Observed variability and potential for real-time calculation, JOURNAL OF CLIMATE, 17 (5): 1097-1109 MAR 2004

Sutton, R., and M. Allen, 1997: Decadal predictability of North Atlantic sea surface temperature and climate. Nature, 388, 563–567.

Sverdrup, H. U. (1953), On conditions for the vernal blooming of phytoplankton, J. Cons. Cons. Int. Explor. Mer, 18, 287– 295.

Sweeney, C., Gnanadesikan, A., Griffies, S.M., Harrison, M.J., Rosati, A.J., Samuels, B.L.: Impacts of shortwave penetration depth on large-scale ocean circulation and heat transport, JOURNAL OF PHYSICAL OCEANOGRAPHY, 35 (6): 1103-1119 JUN, 2005.

Takahashi, T., et al. (2002), Global sea-air CO_2 flux based on climatological surface ocean pCO_2 and seasonal biological and temperature effects, Deep Sea Res., Part II, 49, 1601– 1622.

Takahashi, T., S.C. Sutherland, and A. Kozyr. 2009a. Global Ocean Surface Water Partial Pressure of CO_2 Database: Measurements Performed During 1968–2008 (Version 2008). ORNL/CDIAC-152, NDP-088r. Carbon Dioxide Information Analysis Center, Oak Ridge National Laboratory, U.S. Department of Energy, Oak Ridge, Tennessee, doi: 10.3334/CDIAC/otg.ndp088r.

Takahashi, T., S. C. Sutherland, R. Wanninkhof, C. Sweeney, R. A. Feely, D. W. Chipman, B. Hales, G. Friederich, F. Chavez, A. Watson, D. C. E. Bakker, U. Schuster, N. Metzl, H. Yoshikawa-Inoue, M. Ishii, T. Midorikawa, Y. Nojiri, C. Sabine, J. Olafsson, Th. S. Arnarson, B. Tilbrook, T. Johannessen, A. Olsen, Richard Bellerby, A. Körtzinger, T. Steinhoff, M. Hoppema, H. J. W. de Baar, C. S. Wong, Bruno Delille and N. R. Bates, 2009b: Climatological mean and decadal changes in surface ocean pCO_2, and net sea-air CO_2 flux over the global oceans. Deep-Sea Res. II, 56, 554-577.

Tegen, I., Fung, I.: Modeling of mineral dust in the atmosphere – sources, transport, and optical-thickness. J. Geophys. Res.-Atmos 99, 22897–22914, 1994.

Timmermann, A., Jin, F.F.: Phytoplankton influences on tropical climate, GEOPHYSICAL RESEARCH LETTERS, 29 (23): Art. No. 2104 DEC 6, 2002.

Timmermann, R., Goosse, H., Madec, G., Fichefet, T., Ethe, C., Dulière, V.: On the representation of high latitude processes in the ORCA-LIM global coupled sea ice-ocean model, OCEAN MODELLING, *8*, 175-201, 2005.

Thomas, G.E. and Stamnes, K.: Radiative Transfer in the Atmosphere and Ocean, Cambridge University Press, Cambridge, UK, 1999.

Thomas, H., Prowe, A. E. F., Lima, I. D., Doney, S. C., Wanninkhof, R., Greatbatch, R. J., Schuster, U., and Corbière, A. (2008): Changes in the North Atlantic Oscillation

influence CO2 up- 5 take in the North Atlantic over the past 2 decades, Global Biogeochem. Cycles, 22, GB4027, doi:10.1020/2007GB003167.

Thompson, D.W.J.and J.M.Wallace, 2000: Annular modes in the extratropical circulation.Part I:Month- to-month variability.*J.Climate* ,**13** ,1000-1016.

Trenberth, K. E.,, and J. W. Hurrell, 1994: Decadal atmosphere-ocean variations in the Pacific. Climate Dyn., 9, 303–319.

Uppala, S. M., et al. (2005), The ERA-40 re-analysis, Q. J. R. Meteorol. Soc., 131, 2961–3012, doi:10.1256/qj.04.176.

Uppstroem, L. (1974), The boron-chlorinity ratio of deep seawater from the Pacific Ocean, Deep Sea Res. Oceanogr. Abstr., 21, 161– 163.

Valcke, S., Caubel, A., Vogelsang, R., Declat, D.: Oasis3 ocean atmosphere sea ice soil user's guide, Technical Report TR/CMGC/04/68, CERFACS, Toulouse, France, 2004.

Vichi, M., Masina, S., Pinardi, N.: A generalized model of pelagic biogeochemistry for the global ocean ecosystem. Part I: Theory, JOURNAL OF MARINE SYSTEMS, 64, 1-4, 89-109, 2007.

Vichi, M., Masina, S., Navarra, A.: A generalized model of pelagic biogeochemistry for the global ocean ecosystem. Part II: Numerical simulations, JOURNAL OF MARINE SYSTEMS, 64 (1-4): 110-134 JAN 2007

Vichi, M. and S. Masina: Skill assessment of the PELAGOS global ocean biogeochemistry model over the period 1980–2000, Biogeosciences, 6, 2333-2353, 2009

Visbeck, M; Cullen, H; Krahmann, G; Naik, N**:** An ocean model's response to North Atlantic Oscillation-like wind forcing, GEOPHYSICAL RESEARCH LETTERS, 25 (24): 4521-4524 DEC 15 1998

Visbeck, M. 2002: The Ocean's Role in Atlantic Climate Variability, Science, 297, 2223-2224

Visbeck, M., E. P. Chassignet, R. G. Curry, T. L. Delworth, R. R. Dickson, and G. Krahmann (2003), The ocean's response to North Atlantic oscillation variability, in The North Atlantic Oscillation: Climatic Significance and Environmental Impact, Geophys. Monogr. Ser., vol. 134, edited by J. W. Hurrell et al., pp. 113– 145, AGU, Washington D. C.

Walker, G. T., and Bliss, E.W. 1932: World weather V. *Mem. Roy. Meteor. Soc.,* **4,** 53–84.

Wallace, J.M., and D.S.Grutzler, 1981: Teleconnections in the Geopotential Height Field during the Northern Hemisphere Winter, *Mon.Wea.Rev.,***109** ,784-812.

Wallace, J.M., Smith, C., Bretherton, C.S.: Singular value decomposition of wintertime sea surface temperature and 500-mb height anomalies, JOURNAL OF CLIMATE, 5 (6): 561-576 JUN 1992

Wallace, J.M.: North Atlantic Oscillation/annular mode: Two paradigms - one phenomenon, QUARTERLY JOURNAL OF THE ROYAL METEOROLOGICAL SOCIETY, 126 (564): 791-805 Part A, 2000

Wallace, J. M., and D. W. J. Thompson (2002), The Pacific center of action of the Northern Hemisphere annular mode: Real or artifact?, J. Clim., 15, 1987– 1991.

Wang, M., Overland, J.E., Bond, N.A. (2010): Climate projections for selected large marine ecosystems, J. Mar. Syst. 79, 258-266.

Watanabe, Y.W., H. Ishida, T. Nakano, and N. Nagai, 2005: Spatiotemporal decreases of nutrients and chlorophyll-a in the surface mixed layer of the western North Pacific from 1971 to 2000. *J. Oceanogr.*, **61**, 1011– 1016.

Wanninkhof, R. 1992. Relationship between wind speed and gas exchange over the ocean. J. Geophys. Res. 97: 7373–7382.

Weiss R. F. (1974) Carbon dioxide in water and seawater: the solubility of a non–ideal gas. *Marine Chemistry* **2**, 203–215.

Wetzel, P., Maier-Reimer, E., Botzet, M., Jungclaus, J., Keenlyside, N., Latif, M.: Effects of ocean biology on the penetrative radiation in a coupled climate model, JOURNAL OF CLIMATE, 19 (16): 3973-3987 AUG 2006

Xie, P., and Arkin, P. A.: Analyses of global monthly precipitation using gauge observations, satellite estimates, and numerical model predictions, JOURNAL OF CLIMATE, 9, 840–858, 1996.

Zeebe, R. E., Wolf-Gladrow. D.A (2001): CO2 in Seawater: Equilibrium, Kinetics, Isotopes, Elsevier Oceanography Series, 65, pp. 346, Amsterdam.

Zhao, H., Moore, G.W.K. (2009): Temporal variability in the expression of the Arctic Oscillation in the North Pacific, J. Climate, 22, 3310-3126, DOI: 10.1175/2008JCLI2611.1